HIGH-THROUGHPUT 3D X-RAY IMAGING OF SMALL VERTEBRATE MODEL ORGANISMS ON THE EXAMPLE OF MEDAKA

Zur Erlangung des akademischen Grades eines
DOKTORS DER NATURWISSENSCHAFTEN (Dr. rer. nat.)

von der KIT-Fakultät für Physik des
Karlsruher Instituts für Technologie (KIT)
angenommene

DISSERTATION

von

M. Sc. Sabine Ulrike Bremer
geb. Engelhardt

Tag der mündlichen Prüfung:	09.07.2021
Referent:	Prof. Dr. Tilo Baumbach
Korreferent:	Prof. Dr. Michael Fiederle

Abstract

Many studies in the fields of genetic research, developmental biology, and disease etiology are based on morphological analysis of model organisms. Thereby, a large number of samples is required for statistical analysis. 3D full-body imaging of adult organism would be desirable to study the complete anatomy. Limitations of available measurement setups are a time-consuming data acquisition or insufficient contrast. The aim of this thesis is the development of a pipeline for 3D full-body imaging of adult vertebrate model organisms that overcomes these limitations. The requirements are the visualization of relevant organs and structures with sufficient contrast to allow morphometric analysis and a low time effort. The development of such an imaging pipeline, consisting of sample preparation, data acquisition, and 3D reconstruction, is shown on the model organism medaka (*Oryzias latipes*), also known as Japanese rice fish.

The development of the imaging pipeline is structured as follows: First, potential physical measurement techniques are evaluated. The pipeline then is designed based on the selected technique and optimized to match the requirements. Finally, the complete pipeline is tested.

The full-body imaging pipeline is based on x-ray micro-computed tomography (µCT) to generate the 3D representation of medaka. µCT is easily adaptable to varying sample sizes. At x-ray sources providing a high flux density, fast data acquisition is possible. A challenge in x-ray imaging is the display of biological soft tissues due to their low natural absorption. One solution is the increase of the absorption by staining with a contrast agent. This carries the risk of altering the sample, for example by shrinkage. Phase contrast displays low absorbing structures, but contrary to absorption contrast, it is not directly measurable. In this thesis, absorption imaging, single distance phase retrieval as a phase imaging method and grating interferometry (GI) are tested for their application in 3D imaging of medaka. GI has the advantage of providing absorption, phase, and the so-called visibility contrast based on scattering in a single measurement.

From the three imaging methods, absorption imaging at a synchrotron is chosen for the imaging pipeline. The absorption contrast enhanced with a phosphotungstic acid (PTA) staining and the achieved resolution allowed easy differentiation and segmentation of all relevant organs and tissues. A new staining procedure was developed to achieve sufficient staining of adult medaka. The use of a suitable embedding material enabled fast data acquisition in filtered white beam. Optimizations on the imaging setup resulted in a higher image quality and significantly reduced the time effort for the 3D reconstruction.

The developed imaging pipeline from sample preparation to image reconstruction was successfully applied to several hundred medaka. The average time of 11 min needed for image data acquisition was more than 10 times faster than previous imaging experiments on comparable samples. Comparative analysis showed no significant influence from sample preparation or physical measurement setup on the resulting 3D representations of medaka. Thus, the imaging pipeline is suited for large-scale comparative studies. The developed staining protocol ensured a complete staining of all adult medaka. All relevant organs and structures down to individual brain regions could be distinguished and segmented in 3D.

Due to fast data acquisition times and reliable results, the established imaging pipeline enables for the first time to run large-scale morphometric studies with a reasonable expenditure of time. The knowledge gained in the development of the high-throughput imaging pipeline for medaka can be adapted for other vertebrate model organisms.

Zusammenfassung

Die morphologische Darstellung von Modellorganismen ist Grundlage für viele Studien in den Bereichen der Genforschung, der Entwicklungsbiologie, sowie der Erforschung von Krankheiten und ihren Auslösern. Für statistische Analysen ist dabei eine große Probenzahl notwendig. 3D Ganzkörper-Bildgebung adulter Tiere wäre wünschenswert, um die gesamte Anatomie zu analysieren. Einschränkungen momentaner Messaufbauten sind lange Messzeiten oder unzureichender Kontrast. Das Ziel dieser Dissertation ist die Entwicklung eines Arbeitsablaufes für 3D-Ganzkörperbildgebung adulter Modellorganismen, die diese Einschränkungen überwindet. Anforderungen sind die Visualisierung relevanter Organe und Strukturen mit ausreichendem Kontrast zur Durchführung morphometrischer Analysen, sowie ein geringer Zeitaufwand. Die Entwicklung eines solchen Arbeitsablaufs bestehend aus Probenvorbereitung, Datenaufnahme und 3D Rekonstruktion, wird am Modellorganismus Medaka (*Oryzias latipes*), auch bekannt als japanischer Reisfisch, gezeigt.

Für die Entwicklung des Arbeitsablaufs werden zunächst mögliche physikalische Messtechniken evaluiert. Anschließend wird der Arbeitsablauf auf Basis der ausgewählten Technik entworfen und entsprechend den Anforderungen optimiert. Zum Abschluss wird der Gesamtablauf getestet.

Zur Darstellung der 3D Anatomie von Medaka basiert der Arbeitsablauf auf Röntgen-Mikro-Computertomographie (µCT). µCT kann mit wenig Aufwand auf unterschiedliche Probengrößen angepasst werden. In Kombination mit einer hohen Flussdichte des Röntgenstrahls ist eine schnelle Datenaufnahme möglich. Eine Herausforderung in der Röntgenbildgebung ist die Darstellung von Weichteilen aufgrund ihrer niedrigen Absorption. Eine Lösung ist die Erhöhung der Absorption durch Färbung mit einem Kontrastmittel. Dies birgt das Risiko die Probe zum Beispiel durch Schrumpfung zu verändern. Phasenkontrast bildet niedrig absorbierende Strukturen ab, kann aber im Gegensatz zu Absorptionskontrast nicht direkt gemessen werden. In dieser Arbeit werden daher Absorptionsbildgebung, single distance phase retrieval als Phasenbildgebungsmethode und Gitterinterferometrie, die Absorptions- und Phasenkontrast darstellt, für die 3D-Darstellung von Medaka getestet.

Die Wahl fiel auf Absorptionsbildgebung am Synchrotron. Der Absorptionskontrast resultierend aus einer Färbung mit Phosphorwolframsäure (PTA) und die erreichte Auflösung erlaubten eine einfache Unterscheidung und Segmentierung aller relevanten Organe und Gewebe. Ein neuer Färbeprozess wurde entwickelt, um ausreichende Färbung in adulten Medaka zu gewährleisten. Die Verwendung eines geeigneten Einbettungsmaterials ermöglichte eine schnelle Datenaufnahme im gefilterten Weißstrahl. Optimierungen am Messaufbau verbesserten die Bildqualitäten und führten zu einem kürzeren Zeitaufwand in der Rekonstruktion.

Der entwickelte Arbeitsablauf von Probenvorbereitung bis zur Bildrekonstruktion wurde erfolgreich an einigen hundert Medaka angewendet. Die durchschnittliche Datenaufnahme war mit 11 min mehr als 10mal so schnell wie vorherige Messungen an vergleichbaren Proben. Eine Vergleichsstudie zeigte keinen sichtbaren Einfluss der Probenvorbereitung oder des physikalischen Messaufbaus auf die 3D Darstellung der Medaka. Damit ermöglicht der Arbeitsablauf große Vergleichsstudien. Das neu entwickelte Färbeprotokoll gewährleistete eine vollständige Färbung jedes erwachsenen Medaka. Alle relevanten Organe und Strukturen bis hin zu einzelnen Gehirnregionen konnten unterschieden und in 3D segmentiert werden.

Das entwickelte Verfahren erlaubt durch die kurzen Messzeiten und die zuverlässigen Ergebnisse erstmals die Durchführung großangelegter morphometrischer Analysen mit vernünftigem Zeitaufwand. Die gewonnenen Erkenntnisse aus der Entwicklung des Hochdurchsatz-Arbeitsablaufs für Medaka können auf andere Modelorganismen übertragen werden.

Acknowledgments

This work would not have been possible without the help of many people. First of all, I would like to thank my supervisor Prof. Tilo Baumbach. His support and enthusiasm have carried me through-out this work.

I am grateful to my co-supervisor Prof. Michael Fiederle for his interest in my work and his willingness to invest time in the correction and evaluation.

A special thanks goes to all my colleagues at IPS and IBPT. The great working atmosphere and the readiness to help were a great support throughout the complete thesis. Marcus Zuber's support and suggestions to improve measurements were invaluable. His willingness to help and solve any technical issue even late in the evening saved many measurement campaigns. I am grateful to Tomas Farago for the implementation of the spiral reconstruction in the UFO platform and constant improvements. His advice regarding reconstructions and simulations greatly improved the results. The guidance and assistance given by Thomas van de Kamp have been a great help throughout this work. I greatly appreciate the help by Janes Odar in many night shifts at the beamline and in many productive discussions on biology related questions. I would like to thank Alexey Ershov and especially Yaroslav Zharov for their development of automated segmentation for medaka and for the data provided.

I am grateful to Felix Loosli and his group from IBCS for the fruitful discussions and the samples provided. Special thanks to Narendar Aadepu for the joint optimization of the sample preparation and especially for the preparation of many hundreds of samples.

I would also like to thank Prof. Jochen Wittbrodt and his group from COS Heidelberg for the fruitful collaboration and their assistance in medaka segmentation. Especially Thomas Thumberger and Tina Tavhelidse answered many questions on medaka anatomy and helped preparing the segmentations.

The advice on segmentation with biomedisa given by Philip Lösel was a great help to optimize the results of the segmentations.

Last but not least, I owe my deepest gratitude to my family, especially my husband, for their endless support.

Contents

Chapter 1

Introduction

Vertebrate model organisms play an important role to study development and disease. Research fields include developmental biology, toxicology, and genetic studies as well as drug development and preclinical studies [1–5]. For many studies, imaging is an important tool. Correlation of morphometric data to the genome of different inbred lines will show the influence of individual genes for the development of specific phenotypes, the observable traits of an organism. Comparisons of morphometric features of genetically identical individuals will allow conclusions to be drawn about the influence of external factors as environment or medication on phenotype development. Non-destructive full-body imaging has the advantage of preserving the complete 3D anatomy of the organism. Size and limited transparency in the visible light regime limits the choice of non-destructive imaging methods for display of the full body to microscopic ultrasound imaging (MUI), magnetic resonance microscopy (MRM) and x-ray micro computed tomography (µCT) [6]. MUI and MRM apply no damage to living specimens, making these techniques ideally suited for developmental studies. The achievable resolution is about 25 µm for MRM and 50 µm for MUI in full-body imaging of vertebrate embryos with a few centimetres size [6]. µCT allows resolutions down to some micrometres even for samples larger than embryos. Its application to living animals is restricted due to the applied radiation dose and related damage. MRM and µCT provide tomographic volumes of the sample, which allow arbitrary slicing and morphometric analysis in 3D. Current limitations for large scale studies on adult model organisms are long data acquisition times per full-body scan or low contrast. The aim of this thesis is the development of a high-throughput imaging pipeline optimized for 3D imaging of adult medaka as exemplary vertebrate model organism.

The medaka fish (*Oryzias latipes*) is a teleost model organism widely used for studies on vertebrate development as eggs and embryos are transparent for optic microscopy [7]. The generation time is relative short with eight to twelve weeks. In addition, medaka are highly resistant to inbreeding. This allows the establishment of inbred lines with individuals of identic genome [7]. Currently, about 60 such inbred lines are maintained at the Institute of Biological and Chemical Systems (IBCS) of Karlsruhe Institute of Technology (KIT). Studies on medaka thus allow comparison of morphometric features as well as on phenotype-genotype correlation. High-throughput imaging will enable large scale studies with significant statistics in a reasonable amount of time. Of special interest for such studies are adult medaka, which are opaque in the visible light regime. The desired resolution for imaging of adult medaka is 10 µm to resolve the gill filaments [8], which represent one of the smallest structures in a medaka. Regarding the desired resolution, x-ray µCT is the best suited non-destructive imaging techniques for full-body imaging of medaka. A challenge is the display of biological soft tissue by x-rays due to its low absorption.

Usually, x-ray imaging displays the attenuation of x-rays by a sample in 2D, 3D or even 4D. Exploiting the properties of x-ray waves allow to additionally analyse the induced phase changes. Attenuation as well as phase changes depend on the penetrated material as well as the energy of the x-rays. Attenuation results in a lower amplitude of the x-ray waves by absorption. It is displayed as absorption contrast. Absorption contrast is directly derived from intensity images as acquired by an x-ray detector (section 2.2). Regarding the imaging of medaka, the low absorption of biological soft tissues, consisting of light elements as carbon, is a challenge. A solution is a staining with a high absorbing material [9], that binds to the soft tissue and increases the absorption. Phase changes are significantly higher than the attenuation especially in low absorbing materials (section 2.1). Therefore, phase contrast imaging makes x-ray imaging well suited for the display of biological samples, even for imaging of samples *in vivo* [10, 11]. However, the phase cannot be directly measured by an x-ray detector. The refracted x-ray beam is detectable as intensity changes as Fresnel diffraction after propagation or with the use of optical elements (details see section 2.3). From these intensity images, the phase contrast can be retrieved. Grating interferometry (GI) is an x-ray imaging technique that yields absorption contrast, differential phase contrast, and so-called visibility of a sample in a single experiment. The visibility includes scattering and unresolved differential phase contrast [12]. GI can be used with high-brilliant synchrotron sources as well as conventional x-ray tubes [13, 14]. Applications in medical and biomedical imaging [15–17] have been demonstrated whereby each contrast provides a different information of the sample.

The detailed imaging pipeline depends on the choice of the x-ray imaging technique and the related contrast (figure 1.1). The general work flow of the imaging setup is divided into sample preparation, data acquisition, and image reconstruction. The sample preparation starts with the fixation of the sample to preserve the sample. Staining increases the soft tissue contrast for absorption imaging. The embedding prevents sample movement during the CT scan and thus ensures a good image quality. The data acquisition includes the sample exchange and alignment as well as a CT scan of the sample. A CT scan measures projections of the sample from different angles. In the image reconstruction, the contrast of the sample is retrieved from these projections. A tomographic reconstruction yields a tomogram representing the 3D structure of the sample. Further details regarding contrast retrieval and imaging setups will be discussed in chapter 2.

For morphometric analysis, preservation of the 3D anatomy of the sample is key. In addition, image quality, comprising of contrast and noise, and resolution of the measured anatomy should be high enough to allow differentiation of relevant organs and tissues. These parameters are influenced by the sample preparation and the data acquisition (figure 1.1). Additional requirements for the use in comparative studies are reliable results and the comparability of the 3D representations. The reliability should be given across several measurement campaigns, in the best case carried out at the same imaging setup. A high sample throughput with short acquisition times is desirable for large measurement campaigns. To conclude, the requirements for a high-throughput imaging pipeline of biological samples are:

- availability of the imaging setup for measurement campaigns with large sample series,
- a minimum human effort from sample preparation to final tomogram,
- a minimum time effort, especially regarding data acquisition,
- preservation of the sample anatomy also during storage,
- provision of the 3D representation of the full-body of the organism in sufficient resolution,
- sufficient contrast to allow differentiation of all relevant organs and tissues for morphometric analysis,
- reproducible image quality of the 3D representations for comparative studies.

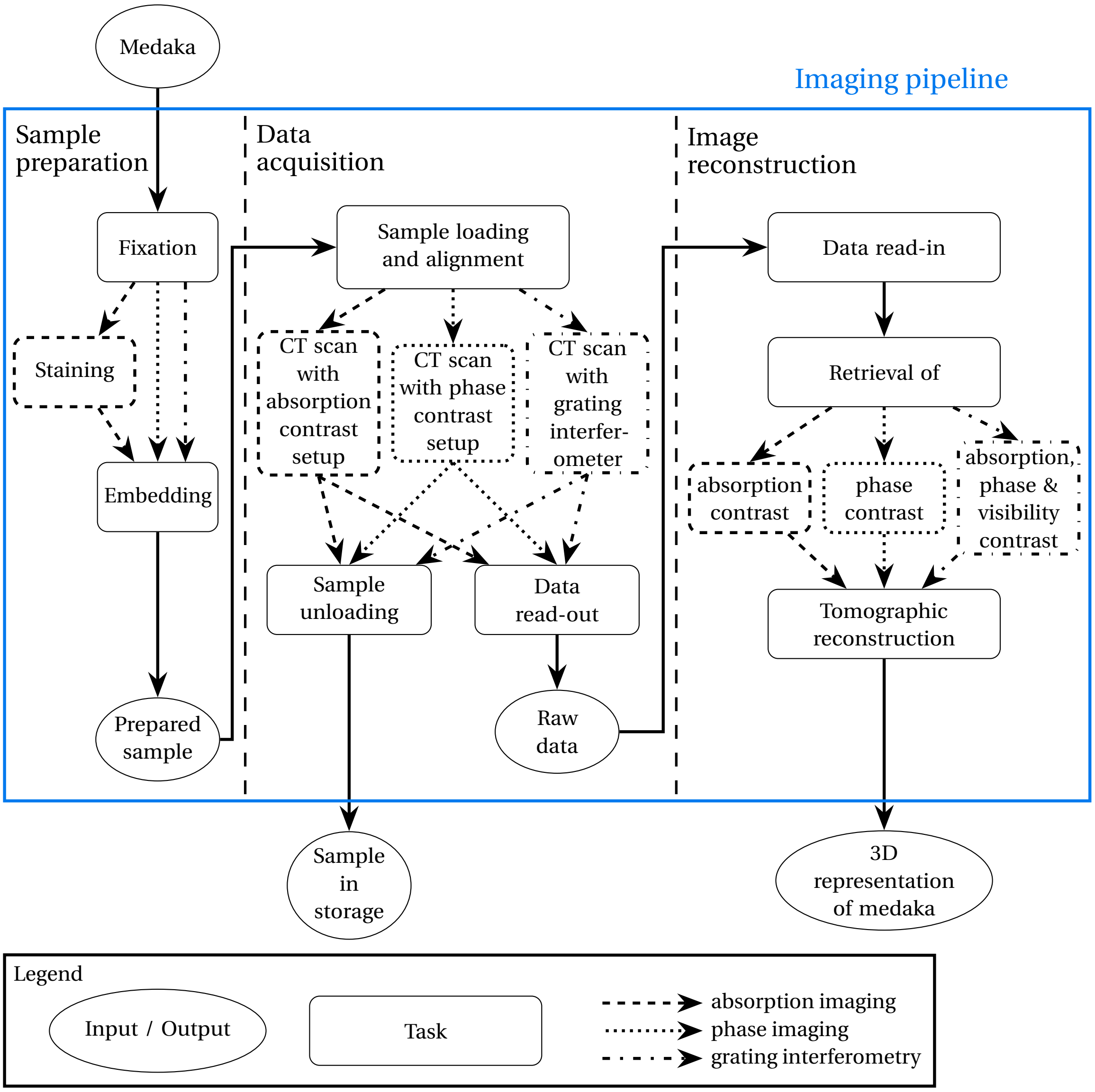

Figure 1.1.: Workflow of an imaging pipeline for a single medaka displayed for absorption imaging, phase imaging, and grating interferometry.

The resulting image quality should be high enough to allow for automated segmentation of organs and tissues from the complete 3D anatomy. The fulfilment of all requirements demands a fine tuning of sample preparation, data acquisition, and image reconstruction under the aspects of the used x-ray imaging technique, time effort and image quality. External constraints, as sample size and computational power, further limit the detailed implementation.

The thesis presents the development of the high-throughput imaging pipeline under these aspects. The outline is as follows: The second chapter presents the fundamentals of the different x-ray imaging techniques. Additionally, it presents the imaging setups as well as the image analysis used in this thesis. The third chapter shows the application of absorption contrast imaging, phase contrast imaging, and grating interferometry on medaka and discusses their potential for high-throughput full-body measurements of medaka. The fourth chapter deals with optimizations of absorption imaging regarding sample preparation, image quality and time effort. The fifth chapter presents the developed high-throughput imaging pipeline for full-body absorption imaging of adult medaka. It summarizes all tasks from sample preparation to the final 3D representation adapted for optimum performance of the imaging pipeline. The sixth chapter summarizes the results and gives an outlook for further use of the imaging pipeline and the resulting data.

Chapter 2

X-ray imaging

X-ray imaging comprises different techniques that use the properties of x-rays to exploit the 2D, 3D or even 4D structure of a sample. As x-rays penetrate matter, x-ray imaging is non-destructive. A general x-ray imaging setup consists of an x-ray source, a sample stage and an x-ray detector placed in line. As discussed in the introduction, absorption imaging, single distance phase contrast imaging, and grating interferometry are considered as imaging methods for high-throughput imaging of medaka.

This chapter explains the basics of these x-ray imaging techniques. It develops the formation of absorption, phase, and visibility contrast from the wave properties of x-rays and presents the image reconstruction for the three imaging techniques, as well as the filtered backprojection for 3D reconstruction. The last part of this chapter presents the imaging setups, the image post-processing, and the image analysis used in this thesis.

2.1. Basic principles of x-ray imaging

X-rays are electromagnetic waves. Characteristics are a short wavelength λ and a weak interaction with matter. The base for the understanding of contrast formation in x-ray imaging are the propagation of the wave and its interaction with matter. If not stated otherwise, the following considerations are adapted from a book by Paganin [18].

The Maxwell equations describe in general the interaction of electromagnetic fields with a medium. From them, the inhomogeneous Helmholtz equation

$$\left[\nabla^2 + k^2 n_\omega^2(x,y,z)\right] \psi_\omega(x,y,z) = 0 \tag{2.1}$$

can be derived. It describes the propagation of a monochromatic plane electromagnetic wave ψ_ω through a non-magnetic, linear isotropic material with refractive index n along z. $k = \frac{2\pi}{\lambda}$ is the wave number. With $n = 1$, the equation becomes the homogeneous Helmholtz equation for propagation in free space. An elementary plane wave

$$\psi_{\omega,e}(x,y,z=0) = \exp\left(i\mathbf{k}\cdot\mathbf{r}\right) \tag{2.2}$$

is a solution to the inhomogeneous Helmholtz equation. The general definition of the refractive index n_ω is

$$n_\omega = c\sqrt{\varepsilon_\omega(x,y,z)\mu_0} \tag{2.3}$$

with ε_ω the frequency dependent electrical permittivity and μ_0 the magnetic permeability. For x-rays, the complex refractive index n is slightly smaller than 1 and can be written as

$$n_\omega = 1 - \delta_\omega + i\beta_\omega. \tag{2.4}$$

Considering the resonant scattering of x-ray waves, the refractive index relates to the atomic scattering length $f(\mathbf{Q}) = f^0(Q) + f'(\omega) + i f''(\omega)$ by [19]

$$n = 1 - \frac{2\pi\rho r_0}{k^2} f^0(Q) + f'(\omega) + i f''(\omega)\,()\,. \tag{2.5}$$

r_0 denotes the Thomson scattering length for inelastic scattering. ρ is the electron density of the material. $\mathbf{Q} = \mathbf{k} - \mathbf{k}'$ is the scattering vector relating the incoming wave $\mathbf{k}$ to the elastically scattered wave $\mathbf{k}'$. The dispersion correction terms f' and f'' are dominated by absorption edges of the related material.

From equation 2.5, the real part δ derives as

$$\delta_\omega = \frac{2\pi r_0 \rho}{k^2} f^0(Q) + f'(\omega). \tag{2.6}$$

δ_ω is called the refractive index decrement. It relates to the inelastic scattering of the x-ray by the material and thus to phase changes.

The imaginary part β is then

$$\beta = -\frac{2\pi r_0 \rho}{k^2} f''(\omega). \tag{2.7}$$

It relates to the absorption coefficient μ of the x-ray waves by direct absorption or elastic scattering displayed in the second term for dispersion correction [19]

$$f'' = -\left(\frac{k^2}{2\pi\rho r_0}\right)\frac{\mu}{2k} = -\left(\frac{k}{4\pi r_0}\right)\sigma_a. \tag{2.8}$$

The linear attenuation coefficient $\mu = 2k\beta_\omega$ and the absorption cross-section σ_a are energy dependent. Different absorption effects dominate the total attenuation coefficient in dependence of the x-ray energy (figure 2.1).

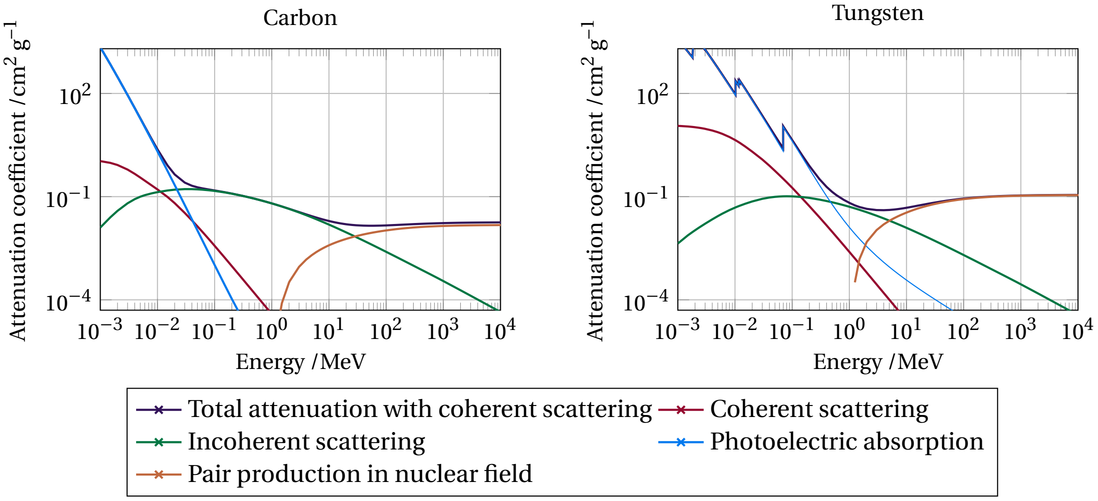

Figure 2.1.: Energy dependence of the attenuation coefficients and the contributing effects for carbon and tungsten. The data is obtained from [20].

The x-ray energies considered in this thesis are below 100 keV. In this region, the photoelectric effect dominates. Its cross-section scales with $Z^4 E_{\text{photon}}^{-1}$ [21]. The photoelectric effect describes the absorption of a photon by an atom with the liberation of a so-called photoelectron. The kinetic energy of the photoelectron is equal to the difference between photon energy and binding energy of the liberated electrons. When the vacancy in the atom is filled with an electron from an upper level, the energy difference is either emitted as a photon or liberates another Auger-electron from the atom. These two effects can be used to study the electron binding energies of a material. The coherent and incoherent scattering of the x-ray waves results in background noise. Their participation to the total attenuation decreases with a higher x-ray energy. Therefore, measuring at high energies is advantageous for noise reduction. Pair production of an electron and a positron requires a photon energy of at least 1.022 MeV, corresponding to twice the rest mass energy of an electron.

Especially in weak absorbing materials, the refractive index decrement δ is much larger than β (figure 2.2). As δ relates to phase changes and β to the linear attenuation coefficient, phase contrast is higher than absorption contrast especially in the low energy x-ray regime. However, phase changes cannot be directly measured as opposed to absorption contrast.

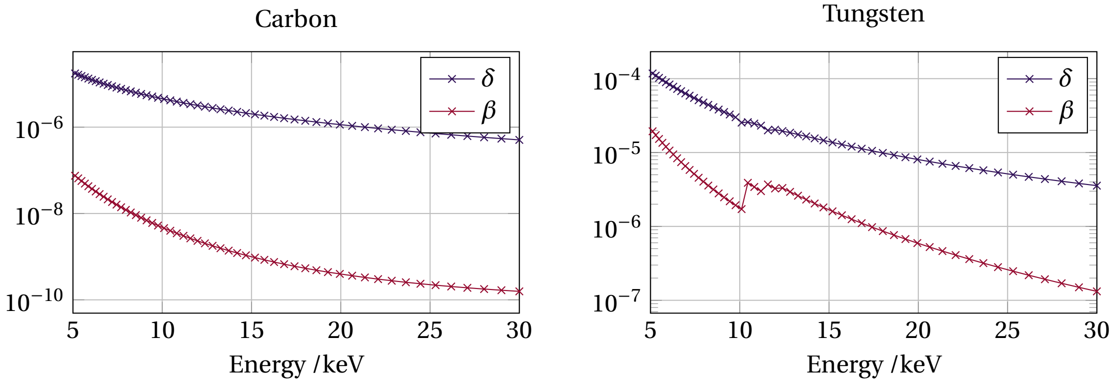

Figure 2.2.: Refractive index decrement δ and β of carbon and tungsten. δ is significantly larger than β for low x-ray energies, especially in light elements. The data is obtained from [22].

2.2. Absorption contrast imaging

The aim in absorption imaging is the measurement of the total linear attenuation coefficient μ of a material. The following section describes the formation of absorption contrast and the image reconstruction. It is derived from the book by Paganin [18].

The first step is to determine the propagated wave field from the unpropagated plane wave (equation 2.2). The projection approximation assumes, that either the scattering of the sample is weak or that the sample is thin. In both cases, the wave field propagates undisturbed between two parallel planes at $z = 0$ and $z = z_0$. The solution of the inhomogeneous Helmholtz equation (equation 2.1) for the propagated wave field can be expressed as

$$\begin{aligned} \psi_\omega(x,y,z=z_0) &= \exp\left(-ik\int_0^{z_0}\left[\delta_\omega(x,y,z) - i\beta_\omega(x,y,z)\right]\mathrm{d}z\right)\psi_\omega(x,y,z=0) \\ &:= T(x,y,z)\psi_\omega(x,y,z=0) \end{aligned} \tag{2.9}$$

$T(x,y,z)$ is called the transmission function. The assumption of line integration over δ and β is only valid if the diffraction in the sample is negligible. This is the case, if only the first Fresnel zone with $\rho_0 = \sqrt{z_0\lambda}$ contributes to the detected wave front. With a minimum wavelength of about 0.1 nm, a sample thickness of 1 cm and a maximum resolution of 5 µm, the projections approximation holds true for all experiments in this thesis. For larger samples, the propagation of the wave field can be approximated as a propagation through N thin slices. In this multi-slice approach, the projection approximation holds true for each slice and the propagation through the complete object can be calculated.

An x-ray detector measures the intensity I of the propagated wave field defined as

$$I = |\psi|^2 = I_0 \exp\left(-2k\int \beta_\omega \mathrm{d}z\right) = I_0 \exp\left(-\int \mu_\omega \mathrm{d}z\right). \tag{2.10}$$

This relation is called Beer-Lambert law of attenuation and can be directly solved for the linear attenuation coefficient μ. I_0, the so-called flat field, is the undisturbed intensity of the imaging setup. As a detector adds noise to the measured intensity due to its electronics, the intensity I_d is measured without beam and considered for the calculation of the absorption

$$\int \mu_\omega \mathrm{d}z = -\ln\left(\frac{I - I_d}{I_0 - I_d}\right) = -\ln T_\mu. \tag{2.11}$$

T_μ corresponds to the ratio between the intensities measured with and without the sample and is called transmission. Thus, the measurement of three intensity images I, I_0 and I_d allows the calculation of an absorption image of the sample. If the sample thickness is known, the total linear attenuation μ can be calculated. The contrast formation only depends on the energy-dependent linear absorption coefficient. For optimum absorption contrast, the x-ray energy should be chosen to be at a maximum of the linear attenuation coefficient. Weak absorbing materials as biological soft tissues result in a low absorption contrast. An increase of the absorption in biological soft tissue is possible using a staining. Its purpose is to bind a high-absorbing molecule to the soft tissue thus increasing its absorption.

To conclude, the implementation of absorption image is simple. An x-ray source and detector are sufficient to measure the intensity of the propagated x-ray wave fields, which is directly related to the x-ray absorption of the penetrated material. Low absorbing biological soft tissue needs a staining to provide sufficient absorption contrast.

2.3. Phase contrast imaging

Phase contrast imaging aims to measure the phase shift, that a sample induces on the propagated x-ray wave. The phase shift $\phi(x,y)$ between incoming and outgoing wave of a sample can be derived from equation 2.9 in the projection approximation:

$$\phi(x,y) = -k\int \delta_\omega \mathrm{d}z. \tag{2.12}$$

Especially in low-absorbing materials, the refractive index δ is larger than β (figure 2.2), which is related to the absorption. Therefore, phase imaging yields a higher contrast in comparison to absorption imaging. However, the phase shift cannot be directly measured using conventional x-ray detectors. Different x-ray imaging techniques have been developed to retrieve the phase contrast. They can be divided into three categories: propagation-based imaging, analyser-based imaging, and interferometric techniques. All techniques require a sufficient coherence of the wave-field. Analyser-based imaging and interferometric techniques require a precise alignment of x-ray source, sample, optical elements as crystals or gratings, and detector. Both techniques scan the refraction pattern of the x-ray wave-field to retrieve the phase of the sample. Propagation-based imaging retrieves the phase from intensity images taken at certain distances behind the sample. Along with multi-distance measurements, methods for phase retrieval from a single propagation distance are available. As single-distance propagation-based imaging bases on a single projection, it is favourable as phase imaging method for the planned imaging pipeline with short acquisition times. Several computation methods exist for single-distance phase retrieval. A requirement on the algorithm for the imaging of medaka is the application on an inhomogeneous sample consisting of low absorbing soft tissue and high absorbing bone. Paganin phase retrieval tolerates [23] inhomogeneous samples. In addition, it is the most stable phase retrieval algorithm in polychromatic beam [24]. This is advantageous due to a higher signal and thus shorter acquisition time in comparison to measurements in a monochromatic beam. Therefore, Paganin phase retrieval is used in this thesis.

This section presents the formation of phase contrast in propagation-based phase imaging and Paganin phase retrieval for single-distance phase imaging. If not stated otherwise, the following paragraphs are derived from the book by Paganin [18].

Coherence

Coherence describes the difference of a real x-ray beam to an ideal plane wave. These differences can be divided into deviations from a perfect monochromatic wave and deviations from a perfect propagation along the optic axis (figure 2.3). The following definitions regarding the coherence are adapted from [19].

The longitudinal coherence regards the polychromaticity of the beam. If two plane waves are in phase at $z_{=}0$, they will be out of phase after propagating a distance L_L. After the distance $2L_L$ they are in phase again. This distance L_L is called the longitudinal coherence length. It is defined as

$$L_L = N\lambda = (N+1)(\lambda - \Delta\lambda)$$

for two plane waves with wavelength λ and $\lambda - \Delta\lambda$, respectively. From the second equation $N = \frac{\lambda}{\Delta\lambda} + 1 \approx \frac{\lambda}{\Delta\lambda}$ is derived. The longitudinal coherence length results to

$$L_L = \frac{1}{2}\frac{\lambda^2}{\Delta\lambda}. \tag{2.13}$$

The different direction of two plane waves in propagation direction is described by the transverse coherence. The definition of the transverse coherence length L_T is similar to that of longitudinal coherence length. Two plane waves with the same wavelength λ emerge with the same phase from a source of width D. Their wave fronts coincidence at points with a distance $2L_T\Delta\theta = \lambda$. The transverse coherence length can be derived from figure 2.3b:

$$L_T = \frac{\lambda}{2\Delta\theta} = \frac{\lambda}{2}\frac{R}{D}. \tag{2.14}$$

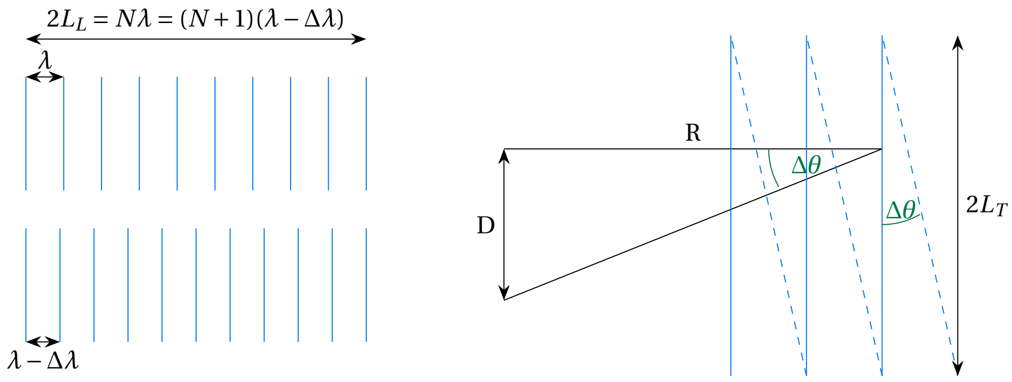

(a) Longitudinal coherence length L_L

(b) Transverse coherence length L_T

Figure 2.3.: Visual representations of (a) longitudinal and (b) transverse coherence length. (a) Two plane waves with a wavelength difference of $\Delta\lambda$ propagate in the same direction. Starting with the same phase, they are again in phase after propagating $2L_L$. (b) Two plane waves are emitted from opposite ends of a source with source size D. The angle between the propagation direction of the waves is $\Delta\theta$. Their phase is equal if the plane waves have the transverse distance $2L_T$. The figures are adapted from [19].

Fresnel diffraction

Propagation based phase retrievals base on the free space propagation of an elementary planar x-ray wave from the plane $z = 0$ to the plane $z = z_0$

$$\psi_{\omega,e}(x, y, z = z_0) = \exp\left(-ik_z z_0\right) \psi_{\omega,e}(x, y, z = 0). \tag{2.15}$$

In Fourier space, a plane wave can be written as linear combination of elementary plane waves. The multiplication with the wave propagator and substitution of $\mathbf{k}\cdot\mathbf{r} \overset{z=0}{=} k_x x + k_y y$ lead to the propagated wave field

$$\psi_\omega(x, y, z = z_0) = \frac{1}{2\pi} \int\int \exp\left(-ik_z z_0\right) \breve{\psi}_\omega(x, y, z = 0) \exp\left(i\left(k_x r + k_y r\right)\right) \mathrm{d}k_x \mathrm{d}k_y. \tag{2.16}$$

Thereby, $\breve{\psi}_\omega(x, y, z = 0)$ is the Fourier transform of $\psi_\omega(x, y, z = 0)$. k_z can be written as $k_z = \sqrt{k^2 - k_x^2 - k_y^2}$. Under the paraxial approximation, the wave vector k of all elementary plane waves has a small angle to the positive z-axis. Then, the following approximation is valid:

$$k_z = k - \frac{k_x^2 + k_y^2}{2k}.$$

With this approximation, the propagated wave field can be written as

$$\psi_\omega(x, y, z = z_0) = \mathscr{D}\psi\_\omega(x, y, z = 0) \tag{2.17}$$

with the diffraction operator

$$\mathscr{D} = \exp\left(ikz_0\right) \mathscr{F}^{-1} \exp\left(\frac{-iz_0\left(k_x^2 + k_y^2\right)}{2k}\right) \mathscr{F}. \tag{2.18}$$

$\mathscr{F}$ denotes the Fourier transformation and $\mathscr{F}^{-1}$ denotes the inverse Fourier transformation. A multiplication of two functions in Fourier space corresponds to a convolution in real space. This allows to rewrite equation as 2.17

$$\psi_\omega(x, y, z = z_0) = \psi_\omega(x, y, z = z_0) \star P(x, y, z = z_1) \tag{2.19}$$

with the Fresnel propagator P

$$P(x, y, z = z_0) = -\frac{ik \exp(ikz_0)}{2\pi z_0} \exp\left(\frac{ik(x^2 + y^2)}{2z_0}\right) \tag{2.20}$$

in real space. The introduction of the Fresnel number

$$N_F = \frac{b^2}{\lambda z_0} \tag{2.21}$$

aids to evaluate the effect of diffraction during propagation. Thereby, b denotes the radius of the unpropagated disturbance at the plane $z = 0$. The simulated transmission of a monochromatic x-ray beam through a gold sphere (top left), an aluminium sphere (top right), and a polymethylmethacrylate (PMMA, $(C_5O_2H_8)_n$, bottom) sphere demonstrates the formation of the diffraction pattern in dependence of the propagation distance z_0 (figure 2.4). The diameter of the spheres is 70.4 µm. The simulation was performed in the `syris` framework [25]. It simulates a monochromatic x-ray beam with an energy of 16 keV at the UFO station (section 2.6.1). The detector corresponds to the PCO.dimax camera (see section 2.6.1) with 10× magnification and a square sensor array with 256 pixel. In the contact regime at $z_0 = 0$, absorption contrast dominates. As the PMMA sphere corresponds to a pure phase object with 100 % transmission, it remains invisible. At small propagation distances with $N_F \gg 1$, the phase is proportional to the Laplacian resulting in edge-enhancement. In the Fresnel regime with $N_F \approx 1$, the diffraction pattern emerges. Further propagation with $N_F \ll 1$ increases the diffraction pattern. The gold sphere corresponds to a pure absorption object and thus the fringes have a low intensity.

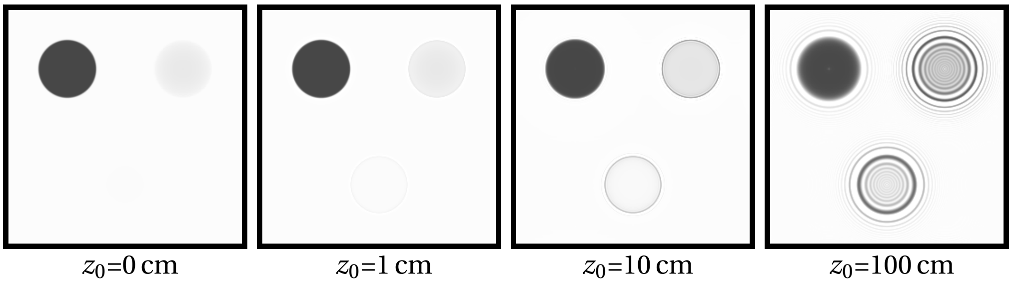

Figure 2.4.: Simulated projections of spheres with a diameter of 70.4 µm. The spheres are made of gold (top left), aluminium (top right), and polymethylmethacrylate (PMMA, bottom). The imaging setup corresponds to the UFO station (section 2.6.1) with a 16 keV x-ray beam. The simulated PCO.dimax camera has a size of 211.2 µm. The magnification of the detector system is set to 10× resulting in an effective pixel size of 1.1 µm. The wave field propagated 0 cm, 1 cm, 10 cm, and 100 cm between the spheres and the detector system. 0 cm is the contact image and displays absorption. With increasing propagation, the Fresnel diffraction pattern increases. The grey values display the transmission from 0 % to 100 % (black to white).
The simulations were performed using `syris` [25].

Paganin phase retrieval

Paganin et al. [23] developed an algorithm to extract the phase image from a single projection. The prerequisites are an incident monochromatic, paraxial wave and a thin, homogeneous sample. In this case, the paraxial approximation is valid.

The transport-of-intensity equation [26] describes the propagation of the intensity pattern of a paraxial, monochromatic wave:

$$\nabla_\perp \left(I(x,y,z)\nabla_\perp \phi(x,y,z)\right) = -k\frac{\partial}{\partial z} I(x,y,z). \tag{2.22}$$

The intensity of a homogeneous object under plane wave irradiation is well described by the Beer-Lambert law (equation 2.11). In addition, the phase at the exit surface becomes proportional to the projected thickness $D(x,y)$ (equation 2.12) for a sufficient thin, homogeneous object. Inserting both into the transport-of-intensity equation 2.22 leads to

$$-\frac{\delta}{\mu} I_0 \nabla_\perp^2 \exp\left(-\mu D(x,y)\right) = \frac{\partial}{\partial z} I(x,y,z=0) \tag{2.23}$$

with use of the identity

$$\nabla_\perp I_0 \exp\left(-\mu D(x,y)\right) \nabla_\perp \delta D(x,y) = -\frac{-\delta}{\mu} I_0 \nabla_\perp^2 \exp\left(-\mu D(x,y)\right).$$

The right-hand-side of equation 2.23 can be estimated by using intensity measurements in two planes separated by a small distance z_1

$$\frac{\partial}{\partial z} I(x,y,z=0) \approx \frac{I(x,y,z=z_1) - I_0 \exp\left(-\mu D(x,y)\right)}{z_1} \tag{2.24}$$

leading to

$$\begin{aligned} -\frac{\delta}{\mu} I_0 \nabla_\perp^2 \exp\left(-\mu D(x,y)\right) &= \frac{I(x,y,z=z_1) - I_0 \exp\left(-\mu D(x,y)\right)}{z_1} \\ \Rightarrow \left(-\frac{z_1\delta}{\mu}\nabla_\perp^2 + 1\right) I_0 \exp\left(-\mu D(x,y)\right) &= I(x,y,z=z_1). \end{aligned} \tag{2.25}$$

The small propagation indicates, that Paganin phase retrieval is valid in the near-field regime with $F_N \gg 1$. The next step is to take the Fourier transformation of the contact image $I_0 \exp\left(-\mu D(x,y)\right)$ and the propagated phase image $I(x,y,z=z_1)$ resulting in

$$\begin{aligned} \left(-\frac{z_1\delta}{\mu}\nabla_\perp^2 + 1\right) \mathscr{F}\left[I_0 \exp\left(-\mu D(x,y)\right)\right] &= \mathscr{F}\left[I(x,y,z=z_1)\right] \\ \Rightarrow \exp\left(-\mu D(x,y)\right) &= \mathscr{F}^{-1}\left[\mu \frac{\mathscr{F}\left[I(x,y,z=z_1)\right]/I_0}{z_1\delta\left|\boldsymbol{k}(x,y)\right|^2 + \mu}\right]. \end{aligned} \tag{2.26}$$

This equation can be solved for the projected thickness D after taking the inverse Fourier transform. The insertion into the relation of the phase $\phi(x,y,z=0)$ at the exit surface with the projected thickness D leads to

$$\begin{aligned} \phi(x,y,z=0) &= -k\delta D(x,y) \\ &= -k\frac{\delta}{\mu} \ln\left(\mathscr{F}^{-1}\left[\mu \frac{\mathscr{F}\left[I(x,y,z=z_1)/I_0\right]}{z_1\delta\left|\boldsymbol{k}(x,y)\right|^2 + \mu}\right]\right). \end{aligned} \tag{2.27}$$

With *a priori* knowledge of the ratio $\beta\delta^{-1}$, the phase can be reconstructed from two intensity images: I with a propagation distance of z_1 between sample and detector and I_0 measured without the sample. As mentioned in the introduction, Paganin phase retrieval remains valid in polychromatic beam and with multi-material samples [27]. In particular, it remains valid if the fraction $\beta\delta^{-1}$ is equal for the different materials [27]. This is the case for low absorbing materials with small β as biological soft tissue.

As in absorption imaging, three intensity images are sufficient to reconstruct the phase of the sample. A flat field without the sample, an image with the sample and a dark-field image without x-ray exposure to account for detector errors. The contrast formation depends on the propagation distance, the x-ray energy, and the energy-dependent refractive index. The optimum propagation distance depends on the imaging setup, mainly its transverse coherence length, as well as from the x-ray energy. So, all parameters depend on each other. The evaluation of the image quality by contrast, SNR, and resolution yields a relationship for the optimum image quality in dependence of the propagation distance [28]. The optimum ratio of object-detector-distance s_{OD} to the source-sample-distance s_{SS} results to

$$\frac{s_{OD}}{s_{SS}} = \frac{\tau_{det}^2}{\tau_{src}^2} \tag{2.28}$$

with the detector resolution τ_{det} and the source size τ_{src}.

To conclude, phase imaging is best suited for the imaging of low absorbing samples. Paganin phase retrieval allows the calculation of the phase by taking just three images. The demands on the imaging setup are a high coherent source and sufficient distance between sample and detector to generate a Fresnel diffraction pattern.

2.4. Grating interferometry

Grating interferometry bases on the so-called Talbot effect to exploit the changes of an x-ray wave induced by a sample. It accesses absorption, differential phase, and so-called visibility contrast of the sample from a set of radiograms. Thereby, the visibility contrast composes of scattering contrast and unresolved phase contrast [12]. Different interferometric setups allow the use of grating interferometry (GI) with high- and with low-coherent x-ray sources.

2.4.1. Talbot effect

The Talbot self-imaging effect states that the interference pattern behind a periodic object repeats itself and is a self-image of the periodic object at the Talbot distance d_T [29]. The periodic objects used in this thesis are one-dimensional absorption or phase gratings with a duty cycle [1] of 0.5 and a rectangular cross-section. Such gratings are known as Ronchi type gratings. The transmission function of such a grating with period p is defined as

$$f(x) = \begin{cases} T_1 & -\frac{p}{2} < x < 0 \\ T_2 & 0 < x < \frac{p}{2}. \end{cases} \tag{2.29}$$

The transmission functions T_1 and T_2 are the object transmission function as defined in equation 2.9. For an ideal absorption grating the transmission functions are $T_1 = 1$ and $T_2 = 0$. Common

---

[1] Ratio between grating period and absorbing part.

phase gratings in GI induce a $\pi/2$ or π shift on the transmitted x-ray wave. The ideal transmission functions result to $T_1 = 1$ and $T_2 = \exp\left(-i\frac{\pi}{2}\right)$ and $T_2 = \exp(-i\pi)$, respectively.

The propagation of a wavefront corresponds to the convolution of the wave front with the propagator, which can be calculated as multiplication in Fourier space. The Fourier series of the wave transmitted by the grating is [30]

$$\mathscr{F}\left((f(x))\right) = \frac{T_1+T_2}{2} - 2\frac{T_1-T_2}{\pi}\sum_{m=0}^{\infty}\frac{\sin\left(2\pi(2m+1)\frac{x}{p}\right)}{2m+1}. \tag{2.30}$$

The factor $2m+1$ indicates that non-zero even diffraction orders are forbidden for such gratings. Equation 2.18 is the free-space propagator in Fourier representation. Taking these considerations into account, the propagated wave field results in

$$\mathscr{F}\left(P(x,y,z)\right) = \exp(ikz)\exp\left(\frac{-iz\left(k_x^2+k_y^2\right)}{2k}\right) \tag{2.31}$$

with the propagation distance z. As the gratings are one-dimensional, k_y equals zero in the diffraction. Values for k_x are derived from the Ewald spere construction [19]. The radius of the Ewald sphere, or the Ewald circle in the case of one-dimensional gratings, is determined by the wave vector k of the incident beam. Intersections of the Ewald sphere or circle with the reciprocal representation of the scattering object represent possible direction of the diffracted x-ray waves. A one-dimensional grating with period p is represented as a set of rods with the reciprocal vectors $h_m = 2\pi m p^{-1}$ (figure 2.5). For diffraction at the one-dimensional grating, k_x must match h_m. Even diffraction orders are forbidden, therefore $k_x \overset{!}{=} \bar{h}_m = 2\pi(2m+1)p^{-1}$. The diffracted wave field results into

$$\mathscr{F}(P(x)) = \exp(ikz)\left[\frac{T_1+T_2}{2} - 2\frac{T_1-T_2}{\pi}\sum_{m=0}^{\infty}\frac{\sin\left(\bar{h}_m x\right)}{2m+1}\exp\left(-iz\frac{\bar{h}_m^2}{2k}\right)\right] \tag{2.32}$$

with the propagator being unity at the origin.

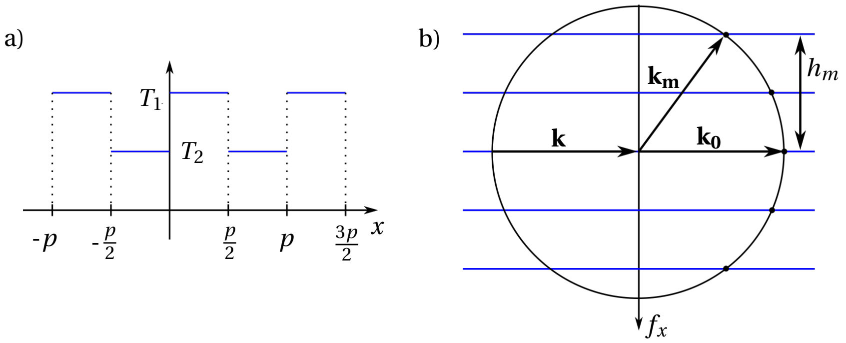

Figure 2.5.: (a) Real space and (b) reciprocal space representation of a Ronchi type diffraction grating with a duty cycle of 0.5 and a rectangular cross-section. (b) Intersections of the Ewald circle with the reciprocal grating lattice represent the possible directions of diffracted x-ray waves.

The wave field, called Talbot carpet, is periodic along z and its shape is repeated in

$$z\frac{\bar{h}_m^2}{2k} = n\pi \quad n \in \mathbb{N}. \tag{2.33}$$

The distances corresponding to the self-images are known as Talbot distance and are defined as

$$z_T = \frac{2np^2}{\lambda}. \tag{2.34}$$

Further evaluations (figure 2.6) reveal self-images of the gratings also at fractional Talbot distances defined as [31, 32]

$$d_T = n\frac{p_e^2}{2\lambda}. \tag{2.35}$$

The effective period p_e depends on the grating properties:

$$p_e = \begin{cases} p & \text{for an absorption grating or a phase grating shifting the x-ray wave by } \pi/2, \\ \frac{p}{2} & \text{for a phase grating shifting the x-ray wave by } \pi. \end{cases} \tag{2.36}$$

The fractional Talbot distances of a π-shifting phase grating are a quarter of the length of the ones of a $\frac{\pi}{2}$-shifting phase grating of the same period. The self-images of a phase grating at odd fractional Talbot orders show the grating pattern as an absorption image. For absorption gratings, this occurs for even Talbot orders and at odd Talbot orders the self-image resembles that of a $\frac{\pi}{2}$-shifting phase grating. In a cone beam setup, a grating is magnified by $M = \frac{L+d_T}{L}$ with L being the source-grating-distance. The Talbot distance increases accordingly to Md_T.

2.4.2. Grating interferometer

In general, a grating interferometer aims to measure the contrast of a sample by detecting the differences in the self-image of a phase grating G1. Grating interferometry, and analyser-based methods in general, retrieves the phase by integration over the refractive angle between incoming and refracted x-ray wave. The direction of the refracted beam is given by the unit vector [19]

$$\frac{\boldsymbol{k'}}{k'} = \frac{\lambda}{2\pi}\nabla\phi(\boldsymbol{r}) \tag{2.37}$$

with $\phi(\boldsymbol{r}) = \boldsymbol{k'} \cdot \boldsymbol{r}$ and in paraxial approximation. The angular deviation α in the plane perpendicular to the propagation direction results in

$$\alpha_x = \frac{\lambda}{2\pi}\frac{\partial\phi(x,y)}{\partial x} \tag{2.38}$$

$$\alpha_y = \frac{\lambda}{2\pi}\frac{\partial\phi(x,y)}{\partial y}. \tag{2.39}$$

The size of the angular deviation α is small. It can be estimated by Snell's law $n_1 \sin(\alpha_1) = n_2 \sin(\alpha_2)$. n_i is the refractive index of the corresponding materials and α_i the angle between the beam and the boundary normal. In the x-ray regime, the refractive index is close to unity. A small incident angle therefore results in a small angle of refraction. For small angles, $\sin(\alpha) \approx \alpha$. With the second material being air ($n_2 = 1$), the angular deviation results in

$$\alpha = \alpha_1 - \alpha_2 = \alpha_1(n_1 - 1) = -\alpha_1\delta. \tag{2.40}$$

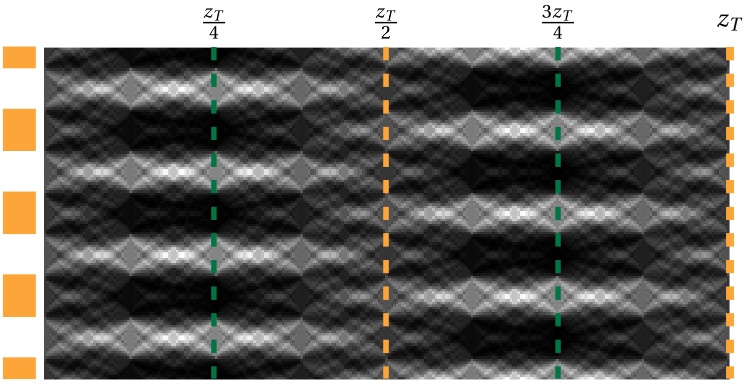

(a) $\frac{\pi}{2}$-shifting grating.

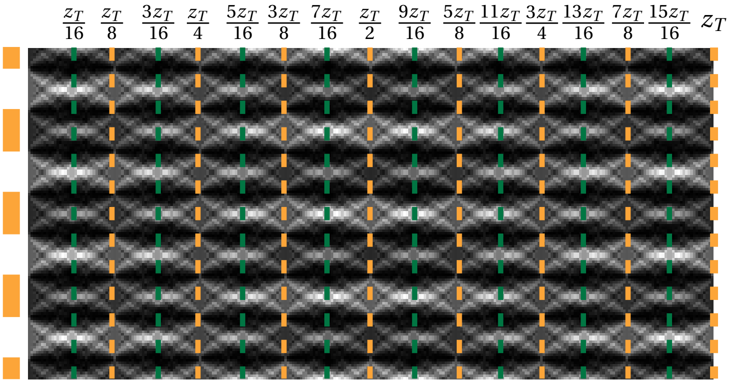

(b) π-shifting grating.

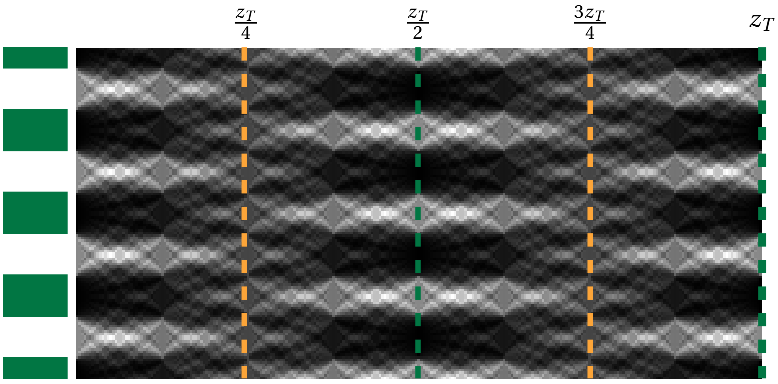

(c) Absorption grating.

Figure 2.6.: Simulated Talbot carpets of Ronchi-type gold gratings with an aspect ratio of 0.5 in monochromatic x-ray beam: (a) phase grating with $\frac{\pi}{2}$-shift, (b) phase grating with π-shift, and (c) absorption grating. Marked are the fractional Talbot distances of phase self-images (orange) and absorption self-images (green) of the gratings. (b) Self-images appear twice as often in a π-shifting phase grating compared to (a) a $\frac{\pi}{2}$-shifting grating or (c) an absorption grating.
The simulations were performed using `syris` [25].

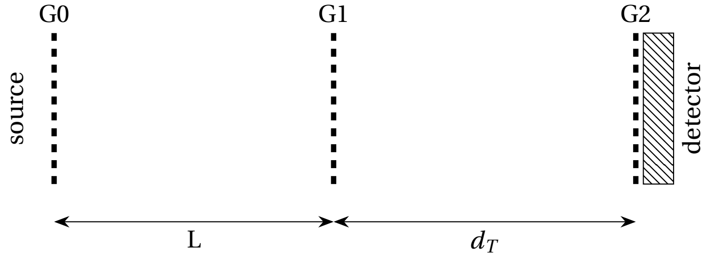

Figure 2.7.: Schematic drawing of a Talbot-Lau interferometer. The source grating G0 and the analyser grating G2 are absorption gratings, G1 is a phase grating. Without the source grating, the setup corresponds to a Talbot interferometer.

Both, α and the refractive index decrements δ, are small, therefore resulting in a small angular deviation.

At highly coherent sources as a synchrotron, it is sufficient to place either a high-resolving detector or an analyser grating G2 coupled with a conventional CCD detector at the Talbot distance of a phase grating G1 to measure the angular deviation. This setup is called Talbot interferometer, as it bases solely on the Talbot effect. The resolution of detector or analyser grating must be high enough to resolve the effective period of G1 in its self-image, which is usually in the range of some micrometres. The prerequisite for the absorption grating G2 is a period of $p_2 = p_{1,e}$ in parallel beam and $p_2 = Mp_{1,e}$ in a cone-beam setup.

A Talbot interferometer requires a small transverse coherence length L_T (equation 2.14) of the beam perpendicular to the grating slits to avoid destructive interference. Therefore, L_T must be smaller than $\frac{Mp_2}{2} = \frac{p_{1,e}}{2}$. The maximum source size for a Talbot interferometer results to

$$s = \lambda \frac{d_T + L_T}{p_{1,e}} = \frac{p_2 L_T}{2d_T}. \tag{2.41}$$

This condition is met by a synchrotron source, but not by conventional x-ray tubes. It is possible to overcome this limitation with the introduction of a source grating G0 [13]. This grating is placed near to the x-ray source and splits the beam into an array of line sources. Figure 2.7 shows a schematic drawing of such a Talbot-Lau interferometer. For constructive interference of the individual line sources at G2, the period of G0 must match [13]

$$p_0 = \frac{L}{d_T} p_2. \tag{2.42}$$

2.4.3. Phase stepping and image reconstruction

Phase stepping [33] is chosen as reconstruction method for GI. It allows to retrieve absorption, differential phase, and visibility contrast. Other approaches yield but one contrast [34, 35] or result in a smaller spatial resolution [36, 37].

In a phase stepping scan, either the phase or the analyser grating is moved in several steps smaller than its effective period. The movement is perpendicular to the x-ray beam and perpendicular to the grating lamella. The resulting intensity variations in each detector pixel (m, n) depend on the ratio of the grating position x_g and the effective grating period p (see figure 2.8). The resulting phase stepping curve can be written as a Fourier series [14, 33]

$$I_{m,n}(x_g) = \sum_l a_l(m,n)\cos\left(lkx_g + \phi_l(m,n)\right). \tag{2.43}$$

The wave number k thereby is defined as $k = \frac{2\pi}{p}$ with p the effective period of the stepped grating. The Fourier components equal the intensity a_0 and the phase ϕ_1 in each detector pixel. The visibility, which shows scattering and unresolved phase contrast [12], is defined as $V = \frac{2a_1}{a_0}$ [14]. The Fourier components can be calculated from the phase stepping curve using different approaches: a direct Fourier analysis [14, 33] and an algebraic retrieval [38]. The contrasts result from the differences in amplitude and phase between the phase stepping curves of an object scan and a reference scan without the sample in the beam.

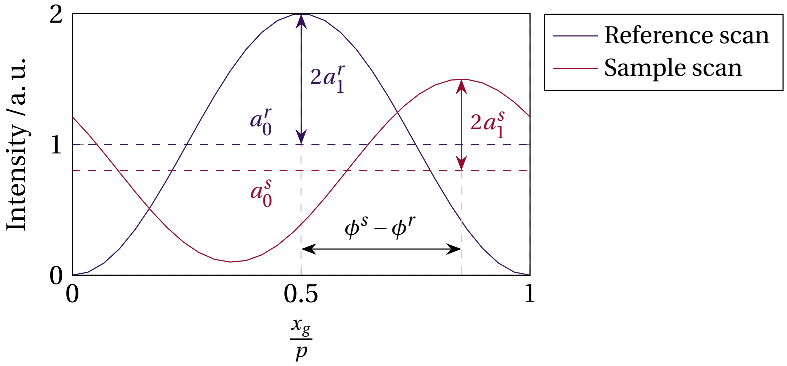

Figure 2.8.: Ideal phase stepping curves of sample and reference scan recorded in one detector pixel. The phase stepping is performed over one effective grating period p. The sample induces an intensity loss and a phase shift $\Delta\phi$ in the recorded intensity.

Fourier analysis

In an ideal grating interferometer, the first order of the Fourier series

$$I_{m,n}(x_g) \approx a_0(m,n) + a_1(m,n)\cos\left(kx_g + \phi_1(m,n)\right) \tag{2.44}$$

is sufficient to completely describe the phase stepping curve. With equidistant steps in the phase stepping scan, a Fast Fourier transform (FFT) directly yields the Fourier coefficients a_0, a_1 and ϕ_1. A FFT performs best if the number of grating positions and thus images equals 2^n with $n \in \mathbb{N}$. Thus, the phase stepping scan should map 2^n equidistant positions over one grating period with $n \geq 2$ to fulfil the Shannon-Nyquist sampling theorem. From reference and object scan, the transmission T_μ, the differential phase $\Delta\Phi(m,n)$ and normalized visibility contrasts V result as [14]

$$T_\mu(m,n) = \frac{a_0^s(m,n)}{a_0^r(m,n)}, \tag{2.45}$$

$$\Delta\phi_x = \phi_1^s(m,n) - \phi_1^r(m,n) \tag{2.46}$$

$$V(m,n) = \frac{a_1^s(m,n)a_0^r(m,n)}{a_0^s(m,n)a_1^r(m,n)}. \tag{2.47}$$

The absorption contrast is related to the transmission by equation 2.11. The differential phase has two constraints: It is limited to the region $]-\pi, \pi]$ as a sine curve is periodic with period 2π, and it is measured only along the stepping direction. The phase is reconstructed from the differential phase with the following considerations on the lateral shift $S(m,n)$ of the refracted beam:

$$S(m,n) = d_T \tan\alpha \approx d_T \alpha \tag{2.48}$$

$$S(m,n) = \Delta\phi_x(m,n)\frac{p_2}{2\pi}. \tag{2.49}$$

Equation 2.48 relates the lateral shift $S(m,n)$ to the angular deviation α of the refracted wave after the propagation from sample to analyser grating. The lateral shift maximizes with a maximum distance between sample and analyser grating. Therefore, the sample should be placed as close the phase grating as possible resulting in a propagation distance equal to the Talbot distance d_T. Additionally, the lateral shift is proportional to the differential phase between refracted and undisturbed wave field as resulting from the signal measured in each detector pixel (equation 2.43). Equation 2.49 considers that the measurement of the phase is performed by an analyser grating with period p_2. With equation 2.38 and a phase stepping in x-direction, the gradient of the phase results to [33]

$$\nabla_x \Phi = \frac{p_2}{\lambda d_T}\Delta\phi. \tag{2.50}$$

With the usage of real gratings, twin-peaks appear in the phase stepping curve caused by the non-ideal gratings [39]. Their cause is a different thickness of the grating lamella at the top and the bottom of the gratings leading to a beat frequency identic to two grating periods. Therefore, a phase stepping over two grating periods is required to acquire the complete phase stepping curve. The contrasts than result out of the zeroth and second order Fourier coefficients.

Algebraic analysis

The algebraic approach solves the Fourier series algebraically for its Fourier components [38]. The retrieval considers the twin-peak phenomenon induced by non-ideal gratings [39] by stepping over two effective grating periods. The Fourier series of such a phase stepping scan includes the second order Fourier coefficients:

$$\begin{aligned} I_{m,n}(x_g) &\approx a_0(m,n) + a_1(m,n)\cos\left(\frac{kx_g}{2} + \phi_1(m,n)\right) + a_2(m,n)\cos\left(kx_g + \phi_2(m,n)\right) \\ &= a_0 + C_2\cos\theta_{x,2} - S_2\sin\theta_{x,2} + C_1\cos\theta_{x,1} - S_1\sin\theta_{x,1} \end{aligned} \tag{2.51}$$

with the definitions $\theta_{x,l} = \frac{lkx_g}{2}, S_l = a_l \sin\phi_l, C_l = a_l\cos\phi_l$ and $l = 1,2$.

The calculation of the Fourier coefficients is most stable with five equidistant grating steps over two grating periods [38]. They are calculated for each detector pixel using matrix multiplication:

$$\begin{pmatrix} a_0 \\ C_2 \\ S_2 \\ C_1 \\ S_1 \end{pmatrix} = \begin{bmatrix} 1 & \cos\theta_{1,2} & \sin\theta_{1,2} & \cos\theta_{1,1} & \cos\theta_{1,1} \\ 1 & \cos\theta_{2,2} & \sin\theta_{2,2} & \cos\theta_{2,1} & \cos\theta_{2,1} \\ 1 & \cos\theta_{3,2} & \sin\theta_{3,2} & \cos\theta_{3,1} & \cos\theta_{3,1} \\ 1 & \cos\theta_{4,2} & \sin\theta_{4,2} & \cos\theta_{4,1} & \cos\theta_{4,1} \\ 1 & \cos\theta_{5,2} & \sin\theta_{5,2} & \cos\theta_{5,1} & \cos\theta_{5,1} \end{bmatrix}^{-1} \begin{pmatrix} I_1 \\ I_2 \\ I_3 \\ I_4 \\ I_5 \end{pmatrix}. \tag{2.52}$$

The second order Fourier coefficients result as

$$\phi_2 = \arctan\frac{S_2}{C_2} \tag{2.53}$$

$$a_2 = \frac{\cos\left(\arctan\frac{S_2}{C_2}\right)}{C_2}. \tag{2.54}$$

Due to the periodicity of the arctangent, the measured differential phase contrast is mapped to the region $[-\pi/2, \pi/2]$. Transmission, differential phase, and visibility contrast are calculated according to the equations 2.45 to 2.47 in the Fourier approach.

2.4.4. Phase unwrapping

Algebraic and Fourier reconstruction map the differential phase $\Delta\phi$ to the domain $]-\pi,\pi]$ and $]-\frac{\pi}{2},\frac{\pi}{2}]$ respectively. Larger phase shifts are not depicted correctly (figure 2.9b). This phenomenon is called phase wrapping. The phase can be unwrapped based on the absorption image [40, 41] or using a multi-energy approach [42]. The phase unwrapping algorithm used in this thesis bases on Besag's statistical consideration of image analysis [43].

Besag's approach uses two assumptions: First, the value or colour of each pixel provides information on the true colour. Second, neighbouring pixels in the original image tend to have similar colours. Both assumptions are valid in GI. First, the true differential phase differs from the measured phase by multiples of π (algebraic) or 2π (Fourier). Second, the phase in a pixel is similar to most of its neighbours as large phase shifts mostly occur at borders between two materials. Under Besag's assumptions, a Markov-Random-Field (MRF) algorithm can be applied to reduce the difference of each pixel to its neighbours and to reconstruct the original differential phase. In the first iteration, the MRF compares the mean of large pixel blocks to take the full image data into consideration. In following iterations, the size of the compared block is reduced systematically down to a single pixel to reconstruct the original image. As the MRF bases solely on the results of the previous iteration, it could be parallelized to reduce the computation time. Figure 2.9 shows a differential phase image before and after phase unwrapping.

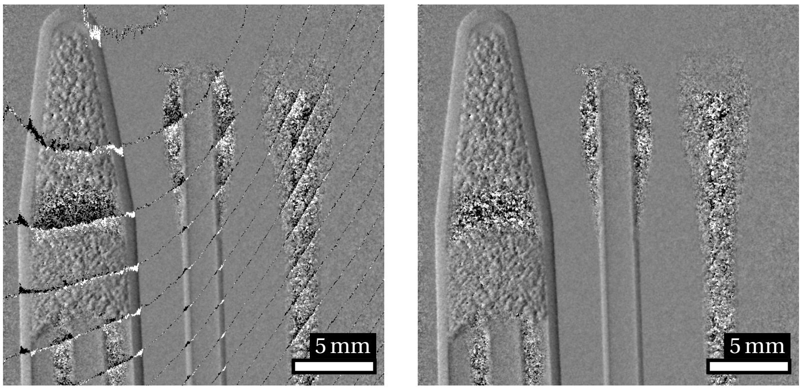

(a) Wrapped differential phase. **(b)** Unwrapped differential phase.

Figure 2.9.: (a) Wrapped and (b) corresponding unwrapped differential phase image. The samples are (left to right): an Eppendorf tube filled with salt, coffee, sugar, and head of a cotton bud (top to bottom), a cotton bud with a plastic rod, and a cotton bud with a wooden rod. The grey values display the range from $-\pi/2$ to $-\pi/2$.

Resulting images

The advantage of grating interferometry is the provision of absorption, differential phase, and visibility contrast from a set of images. This allows precise matching of the different contrasts yielding additional information of the sample. Figure 2.10 shows images resulting from a phase stepping scan with 16 steps over 4 periods and reconstructed using the Fourier approach. The samples are an Eppendorf tube (left), a cotton bud with a plastic rod, and a cotton bud with a wooden rod. The Eppendorf tube is filled with salt, coffee powder, sugar, and the head of a cotton bud (top to bottom). Absorption contrast (a) is proportional to the linear attenuation coefficient. The differential phase (b) is proportional to the phase gradient and therefore sensitive to edges. Visibility (c) displays scattering and unresolved phase contrast [12].

The gain of additional information is most prominent between absorption and visibility contrast. Whereas the salt and sugar yield a similar visibility, the higher linear attenuation coefficient of salt makes distinguishment easy in absorption contrast. Due to its smaller grain size coffee powder results in a higher visibility contrast than salt and sugar. The cotton buds have a low linear attenuation coefficient and thus low contrast in absorption. The small structure of the cotton and especially the wooden rod results in a string scattering of x-rays and high signal in visibility contrast. The plastic rod and the Eppendorf tube are best displayed in differential phase.

To conclude, the combination of all three contrasts gives the whole picture of the sample.

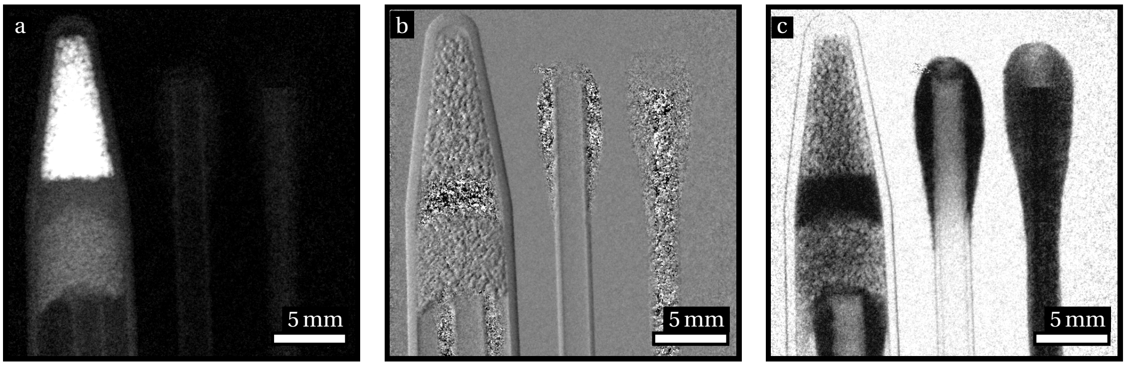

Figure 2.10.: (a) Absorption, (b) differential phase, and (c) visibility contrast reconstructed from a phase stepping scan covering 4 periods with a total of 64 equidistant steps using the Fourier approach. The samples are (left to right): an Eppendorf tube filled with salt, coffee, sugar, and head of a cotton bud (top to bottom), a cotton bud with a plastic rod, and a cotton bud with a wooden rod. Each contrast highlights different areas in the samples. The grey values display the absorption from 0 to 0.4, the differential contrast from $-\pi/2$ to $-\pi/2$, and the visibility from 0 to 1.

2.4.5. Image artefacts

The following paragraphs address possible artefacts appearing in grating interferometry.

Mechanical stability A grating interferometer is sensitive to instabilities perpendicular to the grating slits. A stable lateral position of the gratings is necessary to exactly match reference and sample scan. A stability below one-tenth of the grating period p_2 is desirable [44] to avoid artefacts.

Moiré fringes Moiré fringes are a well-known phenomenon in interferometry. They appear if two similar patterns overlap [45]. In the case of GI, they appear if the self-image of a grating mismatches the shape of the next grating.

At the position of the analyser grating G2, the self-image of the phase grating G1 matches an intensity pattern. The transmission function of absorption gratings is given by [45]

$$f_n(x,y) = a_n + \sum_{j=1}^{\infty} b_{n,j} \cos\left[j\phi_n(x,y)\right]. \tag{2.55}$$

If self-image and grating are rotated by an angle of 2α to each other, the grating functions become

$$\phi_n(x,y) = k_n\left(x\cos\alpha + (-1)^{n-1}\right)\sin\alpha. \tag{2.56}$$

For both functions, n equals 1 or 2 for each of the gratings. The superposition of the transmission functions is given by their product [45]

$$f_1(x,y)f_2(x,y) = a_1a_2 + a_1\sum_{m=1}^{\infty} b_{2,m}\cos\left[m\phi_2(x,y)\right] + a_2\sum_{n=1}^{\infty} b_{1,n}\cos\left[n\phi_1(x,y)\right] \tag{2.57}$$

$$+ \sum_{m=1}^{\infty}\sum_{n=1}^{\infty} b_{1,n}b_{2,m}\cos\left[n\phi_1(x,y)\right]\cos\left[m\phi_2(x,y)\right]. \tag{2.58}$$

The first three parts provide the information of each of the original gratings. The last term represents the superposition of the gratings. With $\cos(x)\cos(y) = \frac{1}{2}\left(\cos(x-y)+\cos(x+y)\right)$, the term $\frac{1}{2}b_{11}b_{12}\cos\left(\phi_1(x,y)-\phi_2(x,y)\right)$ represents the pattern differences. The equation shows that the moiré or beat form lines defined as

$$\phi_1(x,y) - \phi_2(x,y) = (k_1-k_2)x\cos\alpha + (k_1+k_2)y\sin\alpha \tag{2.59}$$

with the centres at $\phi_1(x,y)-\phi_2(x,y) = m2\pi$. The beat wavelength

$$\lambda_{beat} = 2\pi\frac{\lambda_1\lambda_2}{\lambda_2-\lambda_1} \tag{2.60}$$

results from the difference of the wavevectors $k_1 - k_2$.

In the case of grating interferometry, the overlapping objects are the self-image of G1 and the analyser grating G2. Differences can occur for non-ideal gratings or if the alignment is not perfect. In a cone beam setup, plane gratings result in moiré fringes. The propagated self-image of the phase grating is curved according to the curvature of the propagating wave front and does not exactly match the analyser grating (figure 2.11). Bend gratings will reduce the moiré fringes if the bending matches the wave front curvature. In general, a low number of moiré fringes correlates with a high quality of the grating interferometer. As the moiré fringes are independent of the sample, they cancel out in the contrast reconstruction from reference and sample scan.

Polychromaticity A polychromatic beam affects GI, as the design energy of the phase grating and the Talbot distance do not match for the whole wave front. Engelhardt et al. [46] demonstrate, that the interference pattern of a phase grating for a realistic x-ray source maintains a high lateral fringe contrast and flattens with the propagation distance. Therefore, GI tolerates small shifts of the grating positions from the exact Talbot distance for the contrast measurements. For exact evaluation of the measurement data, the application of an effective energy [13] or a correction factor [46] is possible.

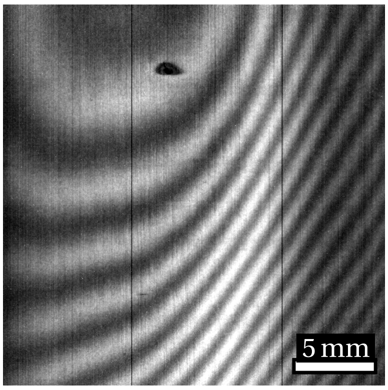

Figure 2.11.: Moiré fringes resulting from a mismatch between propagated self-image of the phase grating in the curved wave-field of a cone-beam setup and the plane analyser grating.

2.5. Computed tomography and tomographic reconstruction

Tomographic reconstruction accesses the 3D structure of a sample from its 2D projections. First reported in the 1970's, computed tomography (CT) is nowadays widely used in medical diagnostics, biomedical imaging, and non-destructive testing. Different reconstruction algorithms allow the reconstruction for a variety of beam geometries and applications.

This section presents a standard tomography setup and the filtered backprojection used for reconstructions in this thesis. Finally, it summarizes common artefacts and limitations of CT.

2.5.1. Experimental setup

A standard CT setup (figure 2.12 (a)) consists of an x-ray source, a sample stage equipped with a rotation axis and a detector. The alignment of the axis of rotation z is as follows:

- perpendicular to the propagation in y-direction of the x-ray wave,
- parallel to the wave front spanning $x-y$,
- parallel to the detector plane $x-y$,
- perpendicular to the pixel rows along x of the detector.

A non-perfect alignment can be corrected automatically prior to the reconstruction but needs additional computation time and sometimes even manual assistance. The sample is placed in the middle of the detector's field of view (FOV). For the measurement, the sample rotates continuously 360° around z to reduce artefacts (see section 2.5.3). At equidistant angular steps, the projection of the sample is measured and used for the tomographic reconstruction (figure 2.12 (b)). The resulting tomogram, consisting of several CT slices, is used for 3D analysis of the sample. If the sample does not fit into the FOV, several CT scans are measured and stitched together after reconstruction. If the sample is extended in only one direction, helical CT can be used. In this case, the longer dimension of the sample is placed parallel to the axis of rotation. During the CT scan, the sample moves along the axis of rotation in z-direction. It is important, that each point in the sample remains in the FOV for at least a 360° rotation. Advantages of helical CT are the avoidance of the stitching and reduction of ring artefacts [47].

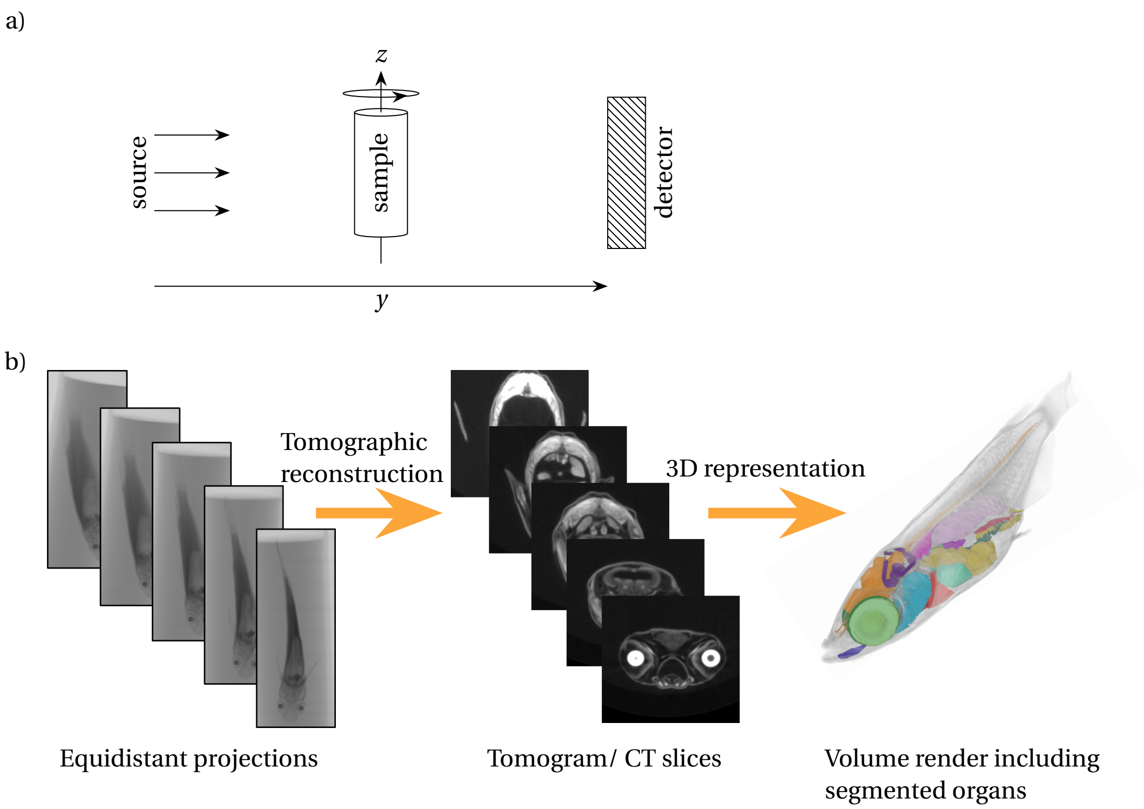

Figure 2.12.: Scheme of computed tomography. (a) Sketch of a standard CT setup in a parallel x-ray beam. The sample rotates around the z-axis, which is parallel to detector and wave front. (b) Equidistant projections are reconstructed to obtain a tomogram consisting of several CT slices. A volume render of the tomogram yields the 3D information of the sample.

2.5.2. 3D reconstruction

Reconstruction algorithms base either on algebraic solutions or on Fourier analysis. Algebraic solutions often incorporate *a priori* knowledge of the sample to gain accurate results, but they are usually computationally expensive. Fourier based reconstruction is faster in computation and can provide reconstructed data already during the experiment. This section presents Fourier based tomographic reconstruction for parallel and cone beam geometry and discusses its adaption for helical CT.

Parallel beam The reconstruction algorithm is easiest derived in absorption contrast and can be applied to phase and dark-field contrast. In parallel beam, the reconstruction is a 2D problem, as each detector line is independent of the others. The reconstruction of the same detector line in each projection results in a 2D slice. The stacking of all 2D slices results in a tomogram containing the 3D information.

The one-dimensional projection of a sample with a non-uniform distribution of absorption $\mu(x, y)$ is

$$I(x) = I_0(x)\exp\left(-\int \mu(x, y)\mathrm{d}y\right) \tag{2.61}$$

$$\Rightarrow \ln\left(\frac{I_0}{I}\right) = \int \mu(x, y)\mathrm{d}y, \tag{2.62}$$

if the x-ray wave is planar and propagates along y. The absorption hereby depends only on the thickness of the absorber. With a rotation of the sample, the angle θ between the object coordinates (x', y') and the laboratory coordinates (x, y) changes. Each measured projection depends on θ and is called Radon transform $R(\theta, x = 0)$.

The Fourier slice theorem (FST)

$$\begin{aligned} P(q_x) &= \int p(x)\exp(iq_x x)\mathrm{d}x \\ &= \int \left(\int f(x, y)\mathrm{d}y\right)\exp(iq_x x)\mathrm{d}x = F\left(q_x, q_y = 0\right) \end{aligned} \tag{2.63}$$

directly connects the Fourier transformation $P(q_x, q_y)$ of a projection $p(x, y = 0)$ and the 2D Fourier transformation $F(q_x, q_y = 0)$ of the slice $f(x, y)$ from which the projection p is generated. Figure 2.13 visualizes the FST. The FST is valid for all projections of the two-dimensional function in the (x, y) plane.

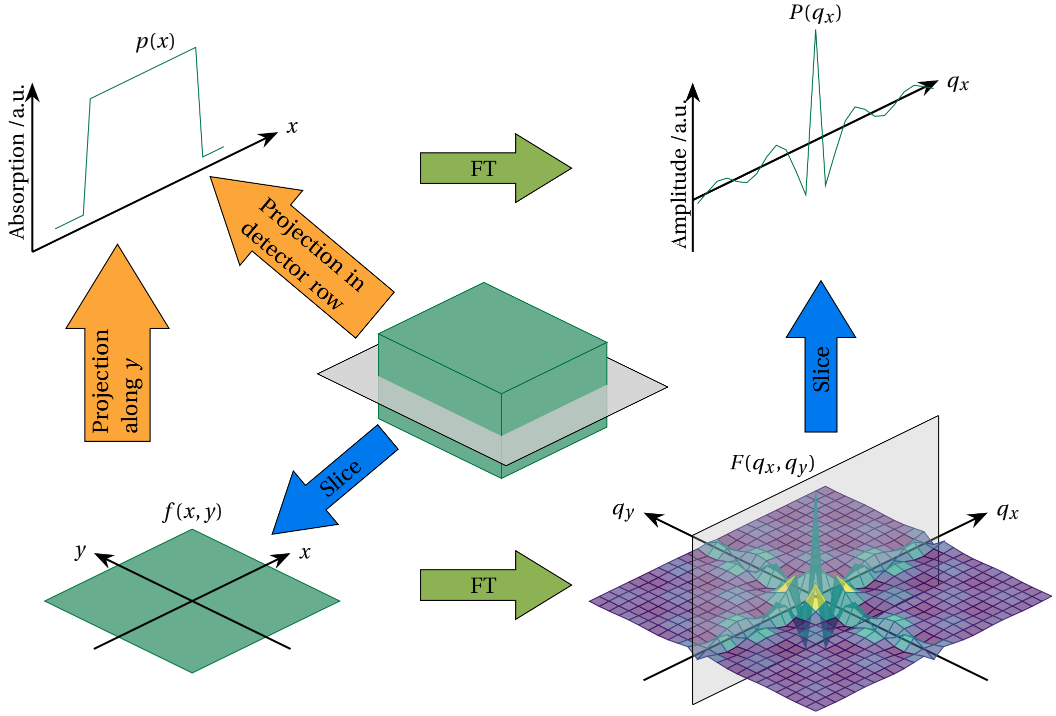

Figure 2.13.: Representation of the Fourier slice theorem [adapted from 19, p. 310]. The slice through the cuboid is a two-dimensional top hat function $f(x, y)$. Its projection along y results in a one-dimensional top hat function $p(x)$. The Fourier transform $P(q_x)$ of $p(x)$ equals a slice of the Fourier transform $F(q_x, q_y)$ of $f(x, y)$ at $q_y = 0$.

Under consideration of the FST, the Fourier transformations of a set of Radon transforms fill a function $M(q_x, q_y)$ in Fourier space. An inverse 2D Fourier transformation than yields the 2D slice $\mu(x, y)$ representing the linear attenuation coefficients of the sample. This approach leads to sampling artefacts as $M(q_x, q_y)$ is known but in the frequency domain. The filtered backprojection overcomes this issue by resampling $M(q_x, q_y)$ before the inverse Fourier transformation. Additionally, filtered backprojection is computationally efficient. Key of the reconstruction is to perform the inverse Fourier transformation in polar coordinates

$$\mu(x, y) = \int_0^{2\pi} \int_0^{\infty} \omega M(\omega, \theta) \exp\left(2\pi i \omega (x \cos\theta + y \sin\theta)\right) \mathrm{d}\omega \mathrm{d}\theta \tag{2.64}$$

with ω a correction factor arising from the conversion of the coordinate system. The Fourier transform of a signal is symmetric and the projections 180° apart equal each other, which allows to adapt the integration limits:

$$\mu(x, y) = \int_0^{\pi} \int_{-\infty}^{\infty} |\omega| \, M(\omega, \theta) \exp\left(2\pi i \omega (x \cos\theta + y \sin\theta)\right) \mathrm{d}\omega \mathrm{d}\theta. \tag{2.65}$$

The Fourier slice theorem now allows to replace the Fourier transformation with the Fourier transformation $P(\omega, \theta)$ of the projections. To conclude, each projection is filtered with a correction term, before being backprojected onto the 2D slice. Thus, the filtered backprojection is suited for online reconstruction during an experiment [48] as each projection updates the slices.

Helical CT

The reconstruction matches the filtered backprojection in parallel beam, if

- the z-movement Δz between two projections is known,
- each section of the sample performed a 180° rotation inside the FOV.

Each part of the sample moved by Δz between two projections. The information of a 2D slice is therefore located at different detector lines in the projection. As Δz is known, the corresponding detector lines can be gathered and reconstructed by FBP.

Cone beam

In a cone beam setup, the wave front is curved and the x-rays are no longer limited to the (x, y)-plane. The Feldkamp algorithm [49] bases on filtered backprojection and considers the angle of each x-ray to the (x, y)-plane for the reconstruction. However, this algorithm shows a blur in z-direction for large angles between x-ray and (x, y)-plane. New algorithms adapt the Feldkamp algorithms for example by rebinning the data onto 2D [50, 51].

2.5.3. Artefacts and their avoidance

Several artefacts can arise in computed tomography (see figure 2.14) and the corresponding 3D reconstruction [52, 53]. The following paragraphs address the artefacts encountered in this thesis.

Beam hardening Beam hardening artefacts arise in a polychromatic beam. The absorption of x-rays with low energies is higher than for high energies (section 2.1). In this case, the assumption of a linear dependence of attenuation of x-rays and absorber thickness taken in the Radon transform no longer holds true. Instead, the attenuation has an additional dependence on the x-ray energy. The sample acts like a high-pass filter. The effect is called beam hardening. As only higher energies pass an absorbing feature, the attenuation behind this feature is lower as the linear attenuation coefficient μ is energy dependent. This non-linear contribution of x-rays to image formation results in streaks arising from the high absorbing feature in the reconstructed tomograms and in too low values in the reconstructed linear attenuation coefficients inside a high absorbing structure, for example a skull. Beam hardening artefacts can be avoided by hardening the x-ray beam before the sample. Common is the use of metal filters as aluminium to remove low energies from the x-ray beam. Iterative reconstruction algorithms offer the possibility to correct the beam hardening during CT reconstruction [54].

Motion artefact Sample movement during the scan leads to a blurred image of sample features in the reconstructed slice (figure 2.14c), as the reconstruction assumes a stationary sample. A fixation of the sample onto the sample stage avoids motion artefacts.

Ring artefact Ring artefacts arise from static errors in the imaging system for example a defect detector pixel. They are reconstructed as rings centred on the rotation axis by the filtered backprojection. In 180° CT scans, half rings appear (figure 2.14d). Reduction of ring artefacts is possible by application of ring filters during tomographic reconstruction. Helical CT includes a relative movement, which also reduces ring artefacts [47].

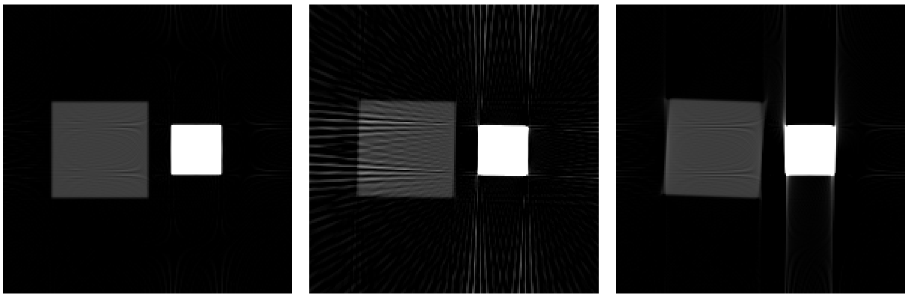

(a) Optimum. **(b)** Undersampling. **(c)** Motion artefact.

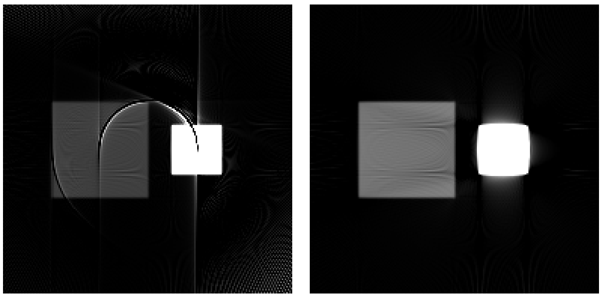

(d) Ring artefact. **(e)** Beam hardening.

Figure 2.14.: Simulated CT slices to demonstrate different CT artefacts. The samples are a cube made of polymethylmethacrylate (PMMA) with 64 µm edge length (left) and an aluminium cube with 32 µm edge length (right). The 180° CT scan is simulated with a 16 keV x-ray beam. (a) The slice of an ideal CT scan and reconstruction displays the exact representation of the cubes. (b) Reconstruction using every third projection leads to undersampling artefacts in form of streaks. (c) Motion of the samples during the CT scan results in blurring, especially on the edges. (d) Measurements of zero intensity in a fixed spot on the detector, for example a broken pixel, are reconstructed as ring artefacts. (e) A polychromatic beam with an energy range from 5 keV to 29 keV results in beam hardening artefacts at the aluminium cube.
The simulations were performed using `syris` [25].

Undersampling Undersampling is related to a violation of the Nyquist sampling theorem. Two requirements avoid an undersampling in Fourier space:

- equidistant projections of a 360° or 180° in parallel beam scan,
- a minimum number of projections of $N_\theta = \frac{\theta_\pi}{4} N_{\text{pixel}}$.

Thereby θ_π is the rotation angle in radians and N_{pixel} is the number of pixels on the detector along x covered by the sample. Violating these requirements leads to streaks in the reconstructed images resulting from the backprojection (figure 2.14b).

2.6. Image acquisition and post-processing

A prerequisite for the high-throughput imaging setup is a high availability. The Institute for Photon Science and Synchrotron Radiation(IPS, KIT) operates a high-throughput imaging setup, called UFO station, at KIT Light Source as well as an x-ray laboratory based on a conventional x-ray tube. The access to the UFO station is restricted by application for beamtime, which is usually a few days per year. The availability for the laboratory setup is higher.

This section presents both imaging setups used for the experiments in this thesis. Furthermore, it presents the image post-processing and analysis of experimental data.

2.6.1. Synchrotron setup

The UFO station at KIT Light Source offers a tomographic setup for high-speed tomography (figure 2.15a). The storage ring is filled with electrons once per day in the morning. A 1.5 T bending magnet provides a white x-ray beam with an energy range from 6.1 keV to 40 keV. Vertical and horizontal slits, a monochromator and material filters as aluminium in different thicknesses are available for beam conditioning. A beryllium window separates the synchrotron's vacuum from the air in the experimental hutch.

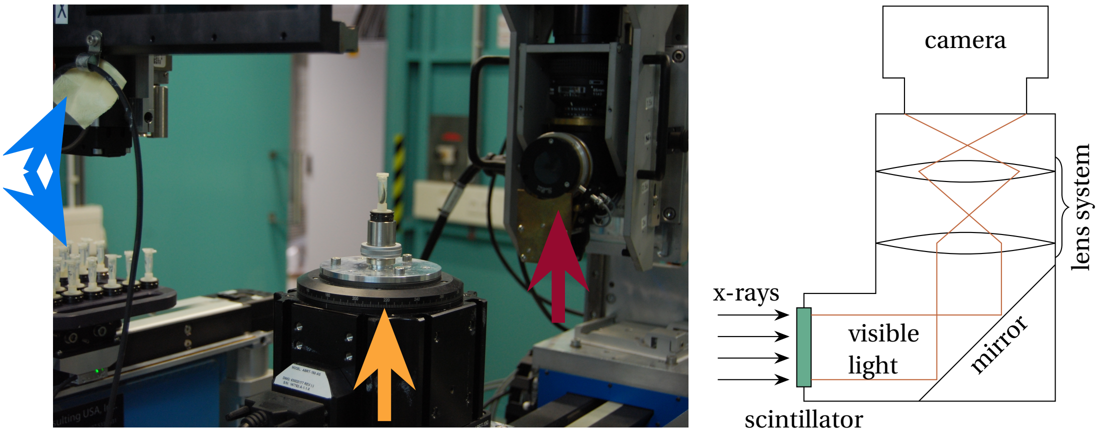

(a) Tomographic station.

(b) Scheme of the detector system.

Figure 2.15.: (a) Tomographic setup of the UFO station at KIT synchrotron. The x-ray beam projects the sample placed on the rotation axis (mid, orange arrow) onto the scintillator (right, red arrow). The detector system (right, top of the scintillator) takes the images. The sample changer robot (left, blue arrows) can hold up to 49 samples. (b) Scheme of a synchrotron detector system. The scintillator converts x-rays into visible light. The microscope comprises a mirror and a lens system. It magnifies and projects the light onto a camera.

The sample position is about 30 m from the source. The sample stage has two degrees of freedom in vertical and horizontal direction perpendicular to the beam for sample alignment. The sample is mounted on a rotary stage that rotates continuously during tomographic scans. A sample changer robot can automatically exchange up to 49 samples in an experimental series.

For image acquisition, a detector system is used (figure 2.15b). A 50 µm thick LuAG scintillator converts x-rays into optical light. The light is magnified by an optical lens system. Three microscopic systems offering different magnifications M are available for white beam imaging: an Elya white beam microscope, a single Optique Peter microscope and an Optique Peter twin mic. The microscopic system projects the light onto a high-speed CMOS camera (PCO.dimax, 2016×2016 pixels, 11 µm×11 µm pixel size) for image acquisition. The effective pixel size ps_{eff} of the detector system results to

$$ps_{\text{eff}} = \frac{ps_{\text{Camera}}}{M}$$

and is stated separately in each experimental description. ps_{Camera} denotes the pixel size of the camera. The theoretically achievable resolution of the imaging setup is $2ps_{\text{eff}}$.

The complete beam line including the tomographic scans is operated by the control system concert [48]. In combination with the UFO platform [55], it offers the possibility to reconstruct a preview of the tomogram during the CT scan at the cost of a longer acquisition time.

2.6.2. Laboratory setup

The Computed Laminography laboratory (CL-Lab) is a custom build x-ray imaging system located at the Institute for Photon Science and Synchrotron Radiation (IPS) of Karlsruhe Institute of Technology (KIT). The setup is highly flexible and allows various applications from computed tomography and laminography to grating interferometry (figure 2.16).

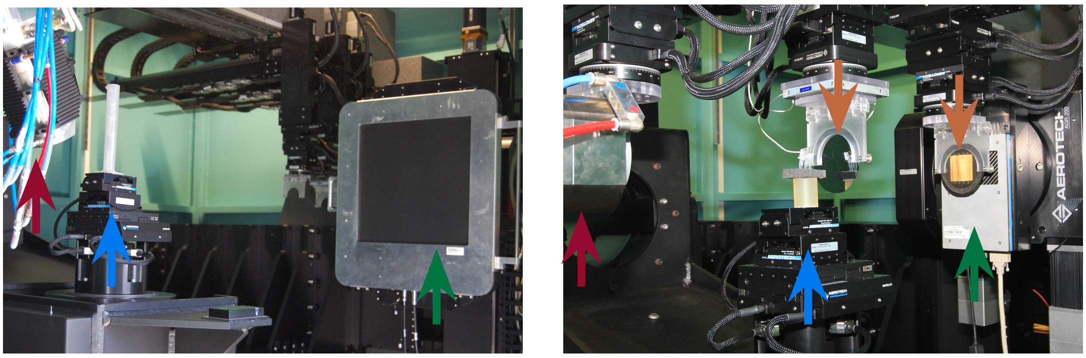

(a) Setup for computed tomography. **(b)** Grating interferometer in Talbot configuration.

Figure 2.16.: Imaging setups at the Computed Laminography laboratory. (a) The computed tomography (CT) setup consists of the microfocus tube head (left, red arrow), the sample stage (mid, blue arrow) and the PerkinElmer detector (right, green arrow). (b) The Talbot interferometer uses the nanofocus tube head (left, blue arrow), sample stage (mid, red arrow), and Dexela detector (right, green arrow). Optic stages (top, orange arrows) hold the two gratings.

The x-ray source is an x-ray tube (XWT-225, X-RAY worX) with a tungsten target. It can operate with a microfocus and a nanofocus tube head. Two different detectors are available. The XRD1621

CN (PerkinElmer) is a flat panel detector with a DRZ+ scintillator. The effective sensor area is 400 mm×400 mm with a pixel size of 200 µm. The Dexela 1207 (Varex Imaging) uses a CsI scintillator. The sensor area is 114 mm×64.6 mm with a pixel size of 74.8 µm.

The sample stage is equipped with a rotation axis and has 6 degrees of freedom for sample alignment: three translations and three rotations around the translation axes. Due to the cone-beam of the x-ray tube, the sample position defines the magnification M and the effective pixel size ps_{eff} of the imaging setup:

$$M = \frac{\text{SDD}}{\text{SSD}}$$
$$ps_{\text{eff}} = \frac{ps_{\text{Detector}}}{M}.$$

Thereby SOD is the source-sample-distance and SDD is the source-detector-distance. ps_{Detector} denotes the pixel size of the detector. The theoretically achievable resolution of the imaging setup is $2ps_{\text{eff}}$. Additional stages allow the placement of optical elements as gratings. All stages have six degrees of freedom for alignment. One stage is equipped with a piezo motor (Mad City Labs Inc.) for high precision positioning and phase stepping.

The control system concert [48] is used to operate the whole laboratory setup including the experiments. New experiments can be easily implemented as a Python script.

2.6.3. Image post-processing

The post-processing of the images depends on the imaging method. In grating interferometry, the absorption, phase, and visibility contrasts were calculated by a script written in Python programming language (http://www.python.org). For tomographic reconstruction, absorption and phase images were processed and reconstructed using a new development of the UFO platform [55]. It includes absorption reconstruction and Paganin's phase retrieval. In addition, UFO offers ring filters for artefact reduction as well as online reconstruction during data acquisition. The tomographic reconstructions ran on two RTX 8000 graphic cards (NVIDIA).

In step CT, the tomographic volumes were stitched by a script written in Python to gain the complete 3D volume of the sample. For the segmentation of organs and structures, the image data was transformed to 8bit using Fiji [56] to reduce data size. The tomographic volumes containing the complete medaka were additionally binned by a factor of two prior to segmentation. The semi-automated segmentation of tomograms started with manual labelling of the selected structures in MITK [57]. The number and distance of the labelled slices was adapted to the complexity of the segmented organ. To complete the segmentation, image and segmentation were uploaded to the web application of biomedisa [58]. Biomedisa uses random walks to interpolate between labelled slices based on image contrast. For display in this thesis, the tomographic volumes were aligned according to their brain in Amira 2019.2 (Thermo Scientific). Orthogonal CT slices were created in Fiji and the background was removed using GIMP 2.10.8 (https://www.gimp.org). Axial views display the medaka from head to tail and coronal views display it from the back to the abdomen. Volume displays were rendered using Amira 2019.2 or Drishti [59].

2.6.4. Image analysis

For comparison of contrast and staining quality, the brain, the liver, and a part of the tail muscle were segmented (see figure 2.17). These structures proved to be the most difficult for the staining in absorption contrast as resulting from a comparison of tomographic results with histological slices [60]. Additionally, they give a complete overview of the sample: They consist of different tissues and are located at different positions on the sample (figure 2.17). From the segmentations, contrast-to-noise ratios (CNRs) and the distribution of grey values were evaluated.

The CNR is a measure for image quality related to contrast and noise. Its definition is

$$CNR = \frac{\left|\bar{\mu}_s - \bar{\mu}_{bg}\right|}{\sqrt{\sigma_s^2 + \sigma_{bg}^2}} \tag{2.66}$$

with $\bar{\mu}$ the mean value and σ the standard deviation of the sample region (s) and the background (bg) respectively. A high value corresponds to an image quality with high contrast and low noise.

The distribution of grey values of a selected area provides information about the uniformity of the contrast and thus, for absorption contrast, the success of the staining. Histograms are an approximate representation of a distribution and are used in this thesis to assess information of the distribution of grey values. The following definitions and symbols are used to define the staining efficiency based on histogram analysis:

- X unstained: More than 5 % of the segmented voxels have values below the threshold and the histogram is unimodal.
- (✓) partially stained: The histogram is multimodal with either more than 5 % of all values below the threshold, one maximum below the threshold or a minimum with a height smaller than 20 % of the mean height of all maxima.
- ✓ completely stained: Less than 5 % of the segmented area is unstained and all maxima are above the threshold.

The threshold corresponds to the background mean for synchrotron data and twice the background mean for laboratory data. This definition considers the beam hardening of the unfiltered polychromatic x-ray beam at the laboratory source, which results in a higher measured background contrast inside the sample. A Python script was written to calculate the CNR and to analyse the histograms. Based on the resulting values, the staining of the sample region is assigned to one of the three defined categories for staining efficiency.

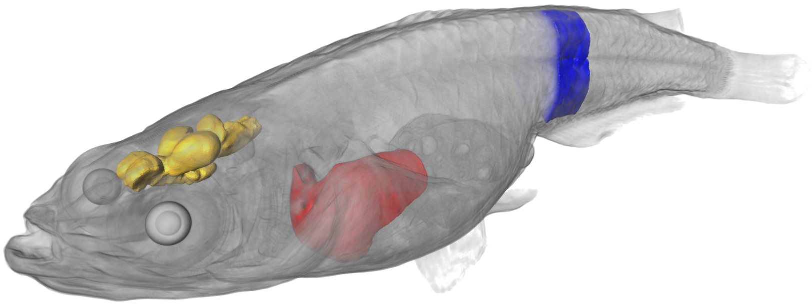

Figure 2.17.: Semi-transparent volume render of a 17 months old medaka. The brain (yellow), the liver (red), and the thickest part of the tail muscle (blue) were used for the calculation of the contrast-to-noise-ratios and for histogram analysis.

Chapter 3

Choice of the imaging method for 3D full-body imaging of medaka

The first task in the development of the high-throughput imaging pipeline for adult medaka was the choice of the x-ray imaging method. The method influences all steps of the pipeline from sample preparation to image reconstruction and is key to receive sufficient contrast in the resulting 3D representation. As discussed in introduction (chapter 1) and theory (chapter 2), absorption imaging, grating interferometry (GI), and single-distance phase imaging based on Paganin phase retrieval are chosen as possible imaging methods. All three imaging methods can yield a 3D representation of the sample, if they are combined with micro computed tomography (µCT) . In this chapter, the imaging methods are optimized for a short acquisition time per sample and tested regarding the resulting image quality and resolution.

The following considerations on the acquisition time are true for absorption imaging, GI, and single-distance phase imaging. Three main aspects contribute to the acquisition time:

- sample loading and alignment,
- data acquisition,
- sample unloading and data read-out.

Sample loading and alignment is fastest with an automated sample exchange. In this case, the time-consuming safety procedure, as hutch search, prior to an x-ray measurement is only performed once for a set of samples. Additionally, the robot places all samples at the same position. If the samples are standardized, a single alignment procedure is sufficient for a complete measurement series. The time for data acquisition is the product of the number of projections and the exposure time. The reduction of either will thus minimize the acquisition time. The number of projections includes flat fields, dark fields, and projections of the samples. The number of flat and dark fields for image correction is lowest in a stable imaging setup. In this case, they remain valid for the complete duration of a tomographic scan, and it is sufficient to measure them once. The minimum number of projections needed for µCT is $\frac{\pi}{2}N_{\text{pixel}}$ to avoid undersampling artefacts in a 360° scan (section 2.5.3). Thereby, N_{pixel} is the pixel number of the detector perpendicular to the axis of rotation. In the parallel beam of a synchrotron, a sample rotation of 180° is sufficient to retrieve the complete 3D information of the sample if it fits into the horizontal detector field of view (FOV). The minimum number of projections then reduces to $\frac{\pi}{4}N_{\text{pixel}}$. A large vertical FOV additionally minimizes the number of vertically translated CT scans needed to cover the full medaka body. Therefore, a large FOV reduces the acquisition time. The exposure time depends on flux density, quantum efficiency of the detector, and the absorption of the sample. It should be long enough to ensure a sufficient signal on the detector without overexposure. The flux density is higher in a polychromatic beam than in a monochromatic beam. Additionally, it is higher at synchrotron sources than at laboratory sources. Therefore, measurements using a synchrotron white beam allow the shortest measurement time. This comes at the cost of a lower coherence than provided by a monochromatic beam and a comparably high heat load at the sample. The heat load can be reduced by filtering low x-ray energies. Just like the loading, the unloading of the sample is fastest with an automated sample exchange. The transfer rate between camera and storage defines the speed of the data read-out. The total duration of the camera read-out depends on the total number of acquired projections. Thus, a low number of projections minimizes the time needed for data acquisition and camera read-out.

A large FOV as well as the use of polychromatic beam lower the possible resolution of an imaging setup. Therefore, the time reduction for each method is studied in this chapter under the aspects of image quality, resolution, and sample preservation.

The expected result of this chapter is a decision for absorption imaging, GI, or phase imaging for the use in high-throughput imaging. Therefore, the acquisition time is minimized for each imaging method. The measures for the decision are the total time effort per sample as well as image quality and resolution of the 3D representation of an adult medaka. Inner organs and tissues should be resolved and well distinguishable.

3.1. Absorption imaging

Absorption contrast displays the attenuation of x-rays by a sample (section 2.2). As biological soft tissues have a low natural absorption, a staining with an absorbing element is needed to ensure sufficient contrast in medaka. The aim for full-body imaging is to use a staining agent, which binds to all tissue types. The staining should sufficiently increase x-ray absorption across the entire medaka, while preserving the tissue structure. A preserved tissue structure supports differentiation of organs and tissues in the tomograms and is important for morphometric analysis. The staining agent phosphotungstic acid (PTA) yielded the best results in a comparison of different staining agents on medaka [61].

Figure 3.1 shows the flowchart of the imaging pipeline for absorption imaging. The highlighted tasks are optimized in the following sections for a synchrotron as well as a laboratory setup. The synchrotron setup was based on an imaging setup developed for high-resolution imaging of medaka by Weinhardt et al. [61]. The resulting tomograms from synchrotron and laboratory measurements were analysed regarding sample preservation, image quality, resolution, and acquisition time.

3.1.1. Sample preparation

Medaka were sacrificed and prepared as stated in table 3.1. The sample preparation was adapted from Weinhardt et al. [61]. The fixation solution is 4 % paraformaldehyde (PFA) mixed with 1 % glutaraldehyde (GA). Washing steps using phosphate buffered saline (PBS) were included into the protocol to remove excess chemicals. A single dehydration step with ethanol was exchanged to a dehydration series with increasing ethanol concentrations to reduce the risk of tissue shrinkage. The medaka were stained using 70 % phosphotungstic acid (PTA) solved in 70 % ethanol. A lab shaker ensures sufficient contact to the chemicals during fixation, dehydration, staining, and washing of medaka. Each medaka was embedded in a 2 ml-Eppendorf tube using 4 % agarose after the last washing step. The preparations were performed at the Institute of Biological and Chemical Systems (IBCS) of KIT by Narendar Aadepu.

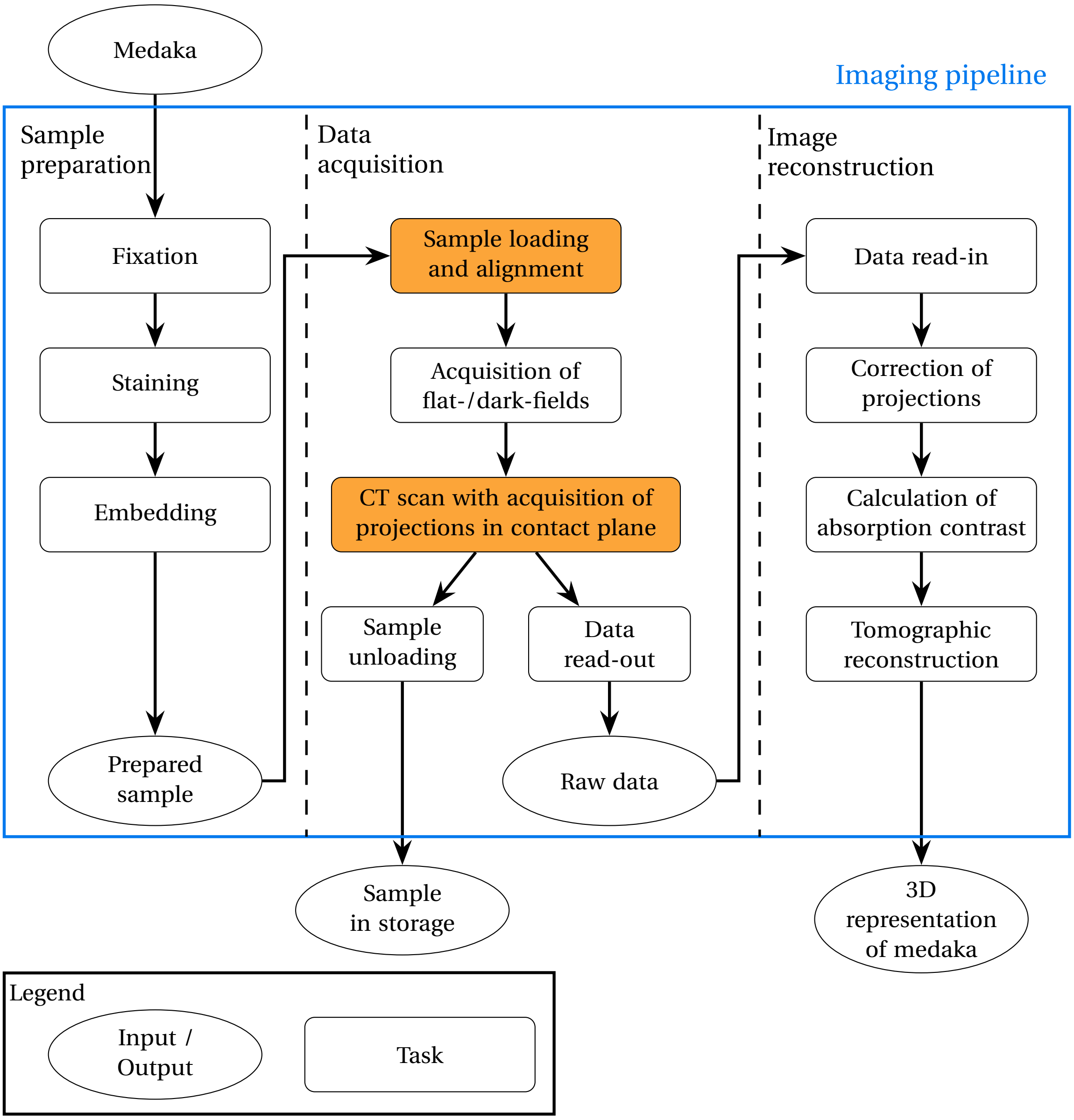

Figure 3.1.: Workflow for 3D x-ray imaging of a single medaka in absorption. Highlighted are the tasks that are optimized in this section for high-throughput imaging.

3.1.2. Synchrotron setup

Weinhardt et al. [57] developed a pipeline for high-resolution absorption imaging of two months old medaka at the UFO station (section 2.6.1). Their imaging setup uses monochromatic x-ray beam at 16 keV with an effective pixel size of 1.81 µm. Each sample is placed and aligned manually prior to the CT scan. The CT scans cover 360° with off-centred rotation axis to fit the samples into the field of view (4.6 mm×3.9 mm). One scan takes about 20 min. Five vertically stacked scans cover the entire length of a medaka resulting in a total acquisition time of 120 min per medaka. This is too long for high-throughput imaging. Therefore, this existing high-resolution setup was

Table 3.1.: Sample preparation for a full-body staining of medaka adapted from Weinhardt et al. [61]. The chemicals are exchanged every 48 h. The abbreviations are listed in table A.1.

Step	Agent	Duration
Fixation	4 % PFA/ 1 % GA	3 days
Washing	PBS	3× 10 min
Dehydration	10 %, 25 %, 50 %, and 70 % ethanol	10 min each step
Staining	0.3 % PTA in 70 % ethanol	3 days
Washing	PBS	3× 10 min
Embedding	4 % agarose	

adapted for high-throughput using the considerations for general reduction of acquisition time. The corresponding optimized tasks are highlighted in figure 3.1. The first task is the sample loading and alignment, which was minimised with the use of the sample changer robot provided by the UFO station. The reduction of acquisition time of a CT scan was possible with an increased flux density and an adaption of the FOV to the sample size. The flux density was increased with the use of a filtered white beam instead of a monochromatic x-ray beam. The horizontal FOV was adapted to fit the sample size to allow 180° scans halving the acquisition time. The size of the prepared samples equals a 2 ml Eppendorf tube with an inner diameter of 8.8 mm and a height of 40 mm [62]. Two different magnifications of the white beam Elya detector system (section 2.6.1) result in a horizontal field of view (FOV) suitable for the samples: 2× with 11.09 mm and 2.5× with 8.87 mm. Both magnifications were tested in an experimental series to check the resulting resolutions as well as precise alignment needed for 2.5× magnification.

Experimental setup

The CT measurements were carried out at the tomographic UFO station at the KIT synchrotron (section 2.6.1). The x-ray beam was filtered with 0.7 mm aluminium to remove low x-ray energies. The filter thus reduces heat load on the sample and beam hardening artefacts (section 2.5). The detector system was the Elya macroscope. The distance between sample and detector was 100 mm resulting in edge enhancement due to angular deviation (section 2.3). A tomographic scan consisted of 1500 equiangular projections over a 180° rotation. The next sample was automatically loaded during the camera read-out of the last tomogram of the previous sample to save time.

The measured medaka were two months old. 14 medaka of the inbred line iCab were measured with 2× magnification. The square FOV has a side length of 11.09 mm. The effective pixel size is 5.5 µm. The exposure time was 100 ms per projection. Five CT scans taken at different vertical positions covered the whole length of the Eppendorf tube and took about 18 min including automated sample exchange and camera read-out. 14 medaka of the inbred line 4-2a and 14 medaka of the inbred line 8-2 were measured with 2.5× magnification. The FOV reduces to 8.87 mm. An Eppendorf tubes thus fits perfectly into the horizontal FOV. The effective pixel size is 4.4 µm. Five vertically translated tomographic scans covered the entire length of a medaka. The exposure time per projection was set to 30 ms due to a higher ring current during the experiments. The time per full body scan of a medaka was 14 min. For both magnifications, the slits limited the beam to an area slightly smaller than the FOV to reduce the heat load.

Results

The results are divided into the analysis of time effort, sample preservation, resolution, and image quality. The analysis of image quality further divides into visual impression, histogram analysis, and CNRs of selected organs.

The measurements confirmed a mean acquisition time per medaka of about 18 min and 14 min, respectively. Regarding the post-processing, the automated reconstruction of a tomogram took about 35 min. Due to bubble growth during the CT scan, automated reconstruction failed for several tomograms. The manual finding of the position of the axis of rotation added an additional 20 min to the reconstruction. The semi-automated stitching of five tomograms took about 40 min per medaka. All operations were performed on two RTX 8000 graphic cards (NVIDIA). The semi-automated segmentation of brain, liver, and tail muscle for the histogram analysis took about 1.5 h per medaka.

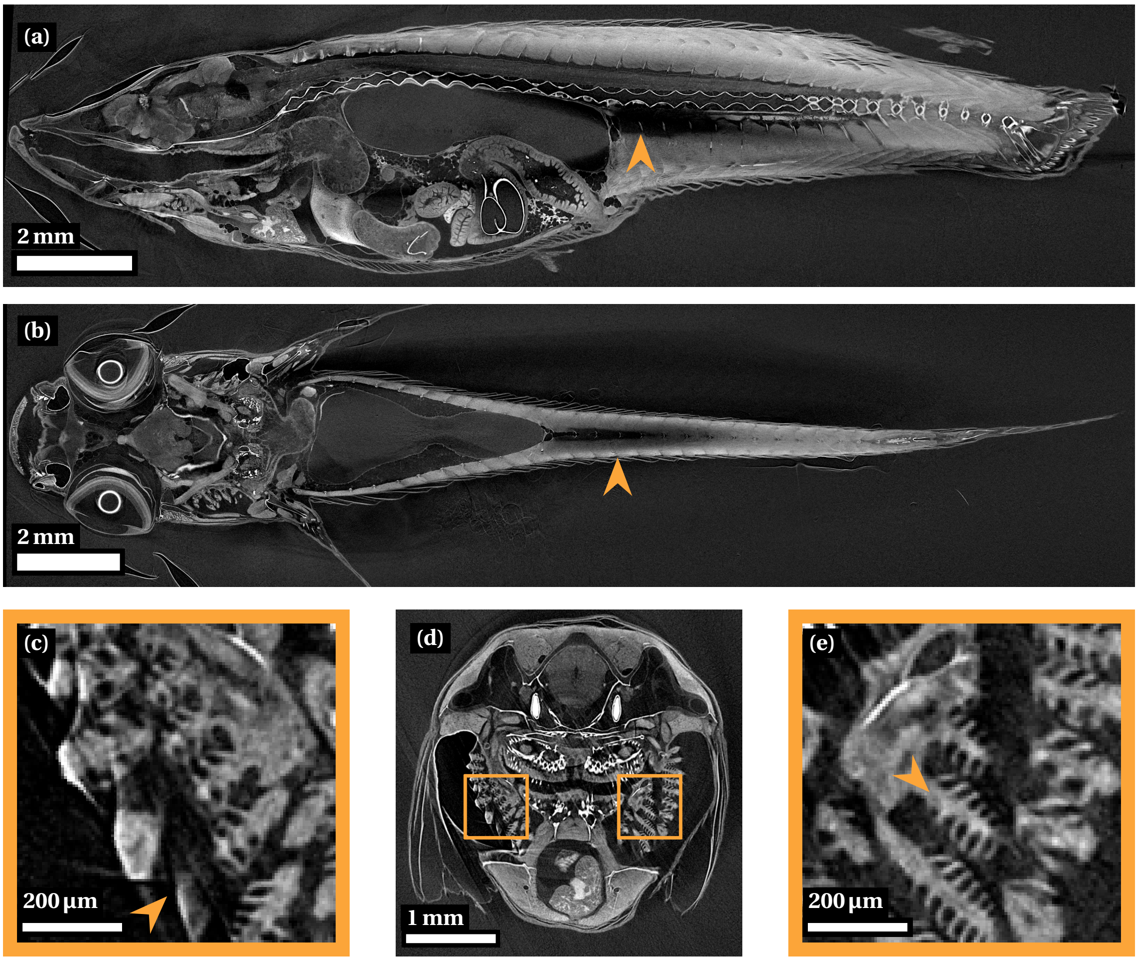

Figure 3.2.: (a) Sagittal, (b) coronal, and (c,d,e) axial slices of a male iCab. (a,b) The tail muscle remained unstained in its thickest part (arrows). (c) and (e) show a detailed view of the axial slice (d) representing the gills. (e) In general, their structure is resolved. (c) Bubble growth in agarose leads to motion artefacts and local reduction of the resolution. The grey values display the linear attenuation from 0 cm^{-1} to 3.64 cm^{-1} (black to white).

Figure 3.2 shows slices of the stitched tomograms of an iCab. The sample preparation preserved the tissue structure by fixation and increased the absorption of soft tissues by staining. The staining resulted in different absorption in different organs and tissues. Even different brain regions are distinguishable. None of the samples showed any shrinkage artefact. A small part of the tail muscle remained unstained in some iCab. The staining of inner organs was insufficient in most medaka of the other two inbred lines. The resolution of the imaging setup was high enough to resolve the structure of the gills also with 2× magnification. The higher resolution with 2.5× magnification eases distinction of fine structures in the gills or of the retinal layers. The sample stayed in the horizontal FOV also for 2.5× magnification. Bubble growth in the embedding agarose led to motion artefacts and lowered the resolution locally. Most bubbles built in areas scanned twice to generate the overlap for later stitching. The bubble growth disturbed the automated tomographic reconstruction, so that most tomographic reconstructions needed manual assistance to find the position of the axis of rotation.

To assess the contrast and thus the staining quality, a histogram analysis (section 2.6.4) was performed. Exemplary, six histograms are displayed in detail. Selected are two brains, two livers, and two tail muscles. One of each pair is completely stained, the other partially or unstained as resulting from visual impression and histogram analysis (figure 3.3). Pairs with similar CNR were selected. Background denotes the embedding material agarose against which the contrast of the selected structures was measured. The volume renders (figure 3.3 (a)) give an impression of the analysed structures and indicate the plane selected for image display (figure 3.3 (c) and (e)). On the CT slices, the contours of the segmented regions are highlighted. The grey values of the images were adapted individually for each image for best display. The histogram analysis evaluates several parameters of the distribution of the grey values in the segmented structure. The first aspect is the number of voxels with grey values below the background mean. In the displayed histograms ((b) and (d)), this corresponds to all values left from the background mean (green line). If more than 5 % of all voxels are below the background mean, the structure is evaluated as unstained. This is the case for the first brain displayed (brain in (b) and (c)). The second aspect is the shape of the histogram. The number of maxima in a histogram gives an estimate of the uniformity of the staining. The histogram is unimodal for both brains, the second liver and the second tail muscle (brain in (b) and (d), liver in (d), tail in (d)) indicating a uniform staining. Uniformity thereby can include a broad range of grey values as in histogram and image of the first brain (brain in (b) and (c)). The multimodal histograms of the first liver and the first tail muscle (liver and tail muscle in (b)) correspond to the regions with different contrasts distinguishable in the according images (liver and tail muscle in (c)). Both histograms have a clear separation between the left maxima and the next maxima marking the sample regions as partially staining. The clear separation is defined by the height of the minimum between the maxima (section 2.6.4). The histograms in (d) all indicate a complete staining. The results from the histogram analysis could be visually verified in the according tomograms as exemplary seen in the CT slices ((c) and (e)).

Table 3.2 displays the values of the six presented histograms as resulting from the Python script for histogram analysis. The assignment to a category of staining efficiency was based on these values.

The analysis of all histograms yielded a complete staining in all three examined regions for 11 of 42 medaka (table 3.3). All 11 are from the inbred line iCab. The remaining 31 medaka were partially stained in at least one of the analysed regions. The brains showed the highest success rate in the staining. From the inbred lines 8-2 and iCab, 13 brains of each were completely stained. From the inbred line 4-2a, 12 brains were completely stained. The remaining 4 brains from the

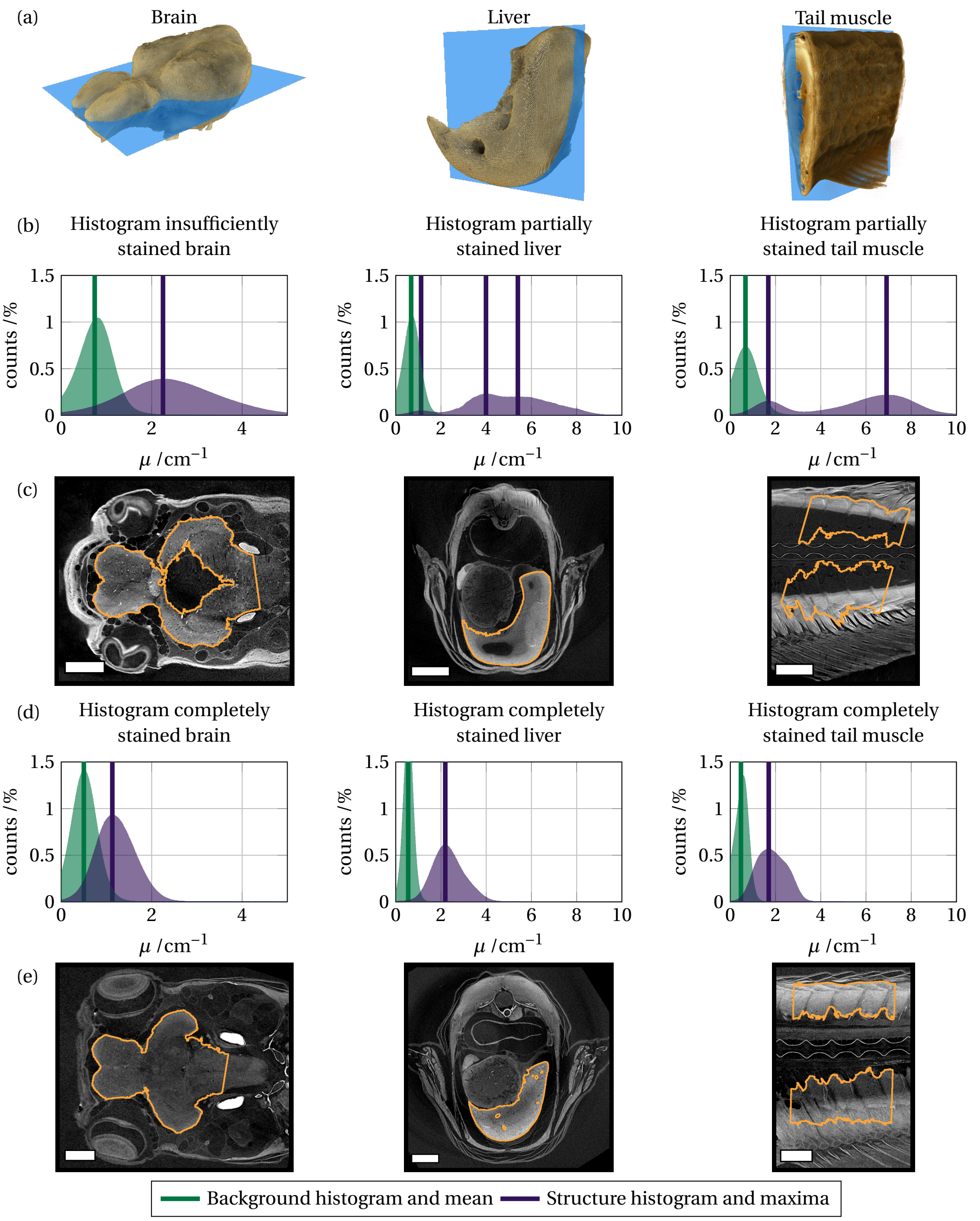

Figure 3.3.: (a) Volume render, (b and d) histograms, and (c and d) CT slices of brains, livers, and tail muscles of two months old medaka. (a) The volume renders display the image plane of the CT slices (c and e). (b) Histograms and (c) CT slices are examples of unstained (brain) or partially stained regions (liver and tail muscle). (d) Histograms and (e) CT slices are examples of completely stained regions. (c and e) The grey values were optimized for best contrast separately for each CT slice. The scale bars represent 500 µm.

Table 3.2.: Results of the histogram analysis of two brains, two livers, and two tail muscles as defined in section 2.6.4. The results are assigned into the three categories unstained, partially stained, and completely stained to get an estimate of the staining efficiency. The corresponding histograms of the analysed regions are displayed in figure 3.3

Sample	region	CNR	Background mean /cm^{-1}	Unstained voxels /%	Maxima at /cm^{-1}	Separated maxima	Resulting category
4-2a_11	brain	1.35	0.72	5.75	2.26	no	unstained
iCab_05	brain	1.32	0.50	4.44	1.13	no	complete
8-2_08	liver	2.37	0.68	0.97	1.12, 3.99, 5.40	yes	partial
iCab_12	liver	2.45	0.55	0.35	2.19	no	complete
4-2a_04	tail muscle	1.88	0.67	1.28	1.68, 6.91	yes	partial
iCab_13	tail muscle	1.90	0.47	0.57	1.70	no	complete

different inbred lines were unstained, thus more than 5 % of the voxels had a grey value below the mean of the surrounding agarose. All livers of the inbred line iCab were completely stained. No liver of the inbred line 4-2a was completely stained. 11 livers remained partially, and 3 livers remained unstained. In the inbred line 8-2, 4 livers were completely stained, 8 partially stained and 2 unstained. The success of the staining in iCab was size dependent. The two tail muscles with the largest volume remained unstained and partially stained, respectively. All tail muscle of the other two inbred lines were only partially stained despite having a smaller volume than iCab.

Table 3.3.: Evaluation of the staining efficiency by histogram analysis. The brain, the liver, and a part of the tail muscle of 42 medaka from the inbred lines 4-2a, 8-2, and iCab were analysed resulting in a low staining efficiency of only 11 completely stained medaka.

	4-2a			8-2			iCab		
Staining	Brain	Liver	Tail muscle	Brain	Liver	Tail muscle	Brain	Liver	Tail muscle
insufficient	2	3	0	1	2	0	1	0	1
partial	0	11	14	0	8	14	0	0	1
complete	12	0	0	13	4	0	13	14	12
all organs complete	0 of 14			0 of 14			11 of 14		

Fig. 3.4 shows boxplots of the contrast-to-noise ratios (CNRs) for brains, livers, and tail muscles in dependence on the inbred line. The CNRs in the brain are similar for all three inbred lines. In liver and tail muscle, the CNRs are significantly higher in iCab. The green and red lines in the boxplots combine the CNRs with the results from the histogram analysis. All regions with a CNR above the green line are completely stained. It is at 1.42 for brains, 2.40 for livers, and 2.00 for tail muscles. All regions below the red line are insufficiently or partially stained. It is at 1.30 for brains, at 1.60 for livers and at 1.70 for tail muscles. There is no detectable relation between CNRs and histogram analysis in the area between the red and the green line.

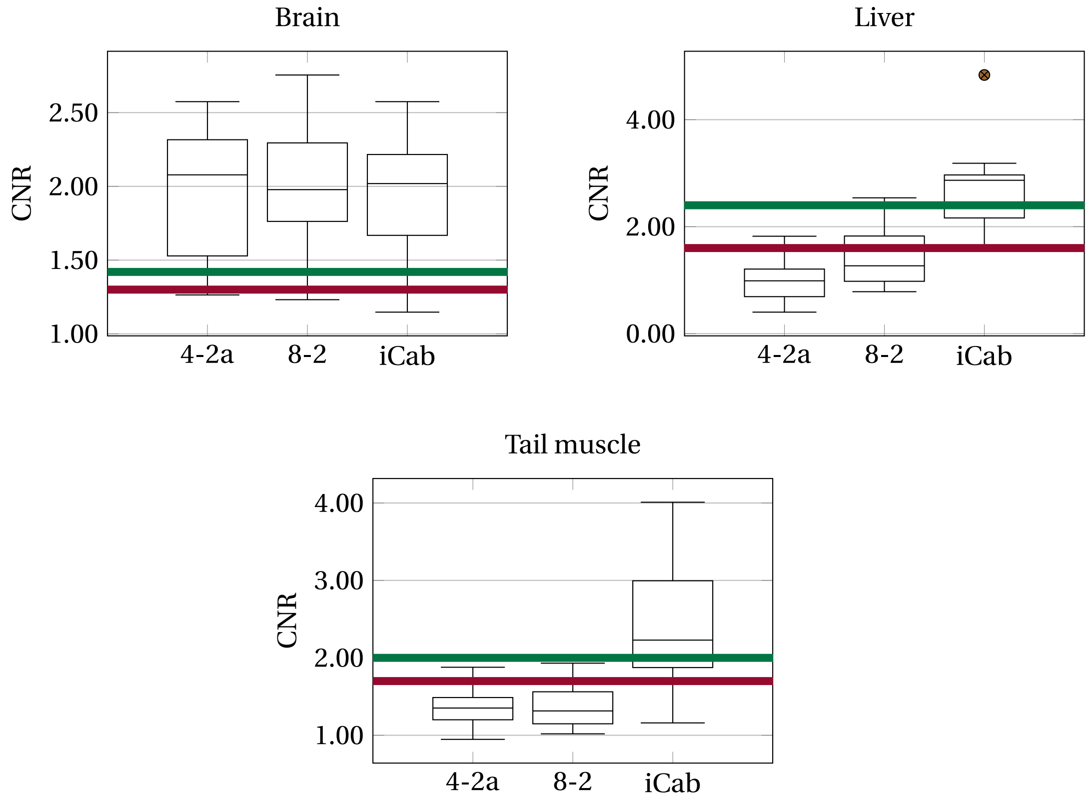

Figure 3.4.: Boxplots of the contrast-to-noise ratios (CNRs) in (a) brain, (b) liver, and (c) tail muscle of the three inbred lines 4-2a, 8-2, and iCab. 14 individuals of each inbred lines were analysed. The green and red lines combine the CNRs with the results from the histogram analysis. All organs with a CNR above the green line are completely stained. It is at 1.42 for brains, at 2.40 for livers, and at 2.00 for tail muscles. All organs with a CNR below the red line are insufficiently or partially stained. It is at 1.30 for the brains, at 1.60 for livers, and at 1.70 for tail muscles. There is no relation between CNR and staining quality in the area between the red and the green lines.

Discussion

Absorption CT scans were carried out with two different magnifications at the synchrotron setup. This discussion addresses the questions of time effort, image quality, resolution, and sample preservation regarding the use of absorption CT for the imaging pipeline.

In a first step, the high-resolution absorption imaging setup presented by Weinhardt et al. [61] was optimized for measurement speed. Full-body absorption CT of two months old medaka needed 18 min with a low ring current and 14 min with a high ring current. The total time includes the sample exchange. This is a time reduction of 88.33 % per sample compared to the acquisition time of the previously reported imaging setup. In addition, the use of the sample changer robot avoided a time-consuming manual sample exchange and alignment procedure. The beam line control in combination with the sample changer robot allowed to scan up to 49 samples without human intervention.

The semi-automated post-processing time comprises of reconstruction and stitching. It was about 3 h per medaka. Bubble growth disturbed the automated reconstruction in some samples.

Manually assisted reconstruction was possible for all samples. The semi-automated stitching of the tomograms took 40 min per medaka. In total, the time effort per sample from acquisition to final tomogram was about 4 h. For large measurement campaigns, automated reconstruction and stitching are desirable to reduce manual workload.

The resolution was sufficient to resolve the structure of the gills in both magnifications. The higher magnification facilitated distinguishment of fine structures as retinal layer. Also, the samples completely stayed in the FOV in both magnifications. Bubble growth in the embedding agarose during CT scans locally reduced the resolution. The bubbles deformed surrounding tissue and led to motion artefacts in the tomographic reconstruction. It also disturbed automated reconstruction. Bubble growth occurred mostly in region scanned twice to generate an overlap for stitching. Therefore, the heat load might cause local gas formation in agarose leading to bubble growth. Additional filters decrease the heat load by filtering low x-ray energies at the cost of a lower signal and possibly longer exposure time. Another option is to replace agarose with another embedding material that is stable under synchrotron radiation.

The image quality is related to the achieved contrast and thus to the staining quality in absorption imaging. To access staining efficiency, the histograms of brains, livers, and a part of the tail muscle were analysed. It yielded a complete staining in all three regions for 11 of the 42 examined medaka leading to a 26.2 % success rate. The other 31 medaka showed insufficient staining in at least one of the regions. The 11 completely stained medaka were all from the inbred line iCab. The staining efficiency was higher in smaller iCab. Still, even smaller medaka from the inbred lines 4-2a and 8-2 remained unstained. The protocols and chemicals used for the sample staining were identical so that no staining difference was expected. As iCab were stained in May and the other two inbred lines in November, maybe a different air temperature during the staining procedure had an influence on PTA penetration. Another explanation is a dependence on the inbred line. Up to now, no studies on the properties of skin of different medaka inbred lines are available. The visual analysis showed that a successful PTA staining yields sufficient contrast to distinguish between different organs and tissues. Even different brain regions and the retinal layers were distinguishable by contrast.

In addition, the CNR was calculated for each examined region. A high CNR corresponds to a high image quality with a high contrast and a low noise. The CNR of the brains is similar for all inbred lines. In livers and tail muscles, the CNR of iCab is significantly higher due to a higher staining efficiency as resulting from the histogram analysis. The comparison of CNR and histogram analysis shows that the CNR cannot give an estimate of staining efficiency. The CNR for sufficient contrast differed between the examined regions. This indicates a different absorption which eases distinguishment of the organs and tissues. The overlap of CNRs for completely and insufficiently stained organs as defined by histogram analysis results from different noise in the tomograms. In general, the noise was higher if the segmented region was located at the upper or lower detector edge during the CT scan. In these regions, the flux density is lower due to the beamline geometry. A larger overlap between the tomograms thus would lead to a higher image quality.

From a visual comparison to histological slices [60], all organs and structures in the medaka were well preserved except for fatty tissue. Fat is dissolved by ethanol which is used in the staining protocol. However, fat is of no special interest for morphometric analysis.

To conclude, the optimized absorption imaging setup is suited for high-throughput measurements of medaka. Both tested magnifications yielded a similar CNR. The higher magnification should be favoured, as the higher magnifications provides a higher level of detail in the 3D representations. A larger overlap between the step CT scans might improve the image quality in the stitched parts at the cost of an additional CT scan. Another option would be helical CT configuration, which also reduces post-processing time, as no stitching is necessary. The sample preparation used is not suited for large scale experiments. The PTA staining protocol yielded no reliable results. Bubble growth in the embedding agarose locally reduced the resolution and disturbed automated tomographic reconstruction. Before implementing absorption imaging into the imaging pipeline, an optimization of the staining and the embedding are required. An optimized embedding is also useful for the other imaging methods.

3.1.3. Laboratory setup

Some phenotypic features in medaka establish with age. As medaka keep growing with age, older medaka do not fit into the available FOV of a synchrotron setup. A laboratory setup offers a larger FOV and thus is suited for the measurement of old, large medaka. In addition, laboratory setups are easier available. The drawback is a longer acquisition time due to a lower flux density in comparison to a synchrotron setup.

This section tests absorption imaging at the laboratory setup on 17 months old medaka to gain an estimate for image quality, resolution, and acquisition time.

Experimental setup

The experiments were carried out at the Computed Laminography laboratory (section 2.6.2). The settings of the x-ray tube were 40 keV and 15 W. The samples were 17 months old medaka with about double the size of a two months old medaka. The sample position was adapted such, that the medaka fit completely into the FOV. The resulting distances were 148 mm between x-ray tube and sample and 1711 mm between x-ray tube and detector. With the PerkinElmer detector, the effective pixel size resulted to approximately 17.3 µm. The cone-beam CT scans ran over 360° with 2048 equidistant projections. The exposure time per projection was 4 s. This results in an acquisition time of 2.5 h. Sample change and alignment were carried out manually.

Results

The results divide into the time effort and a visual evaluation of image quality and resolution.

Each medaka was scanned in about 2.5 h. Manual sample exchange and alignment added an additional 15 min to the acquisition time for each medaka.

The medaka showed a low absorption contrast on the inside (figure 3.5). From the soft tissues, only regions close to the surface or open to the outside as skin, mouth, gills, and anal region were stained and showed sufficient contrast. In addition, the natural absorption of the bones resulted in absorption contrast. The resolution is not sufficient to resolve the complete structure of the gills (figure 3.5 (d)). Due to the low contrast, segmentation of brain, liver, and tail muscle for further analysis was not possible.

Discussion

The discussion addresses the absorption imaging at the laboratory setup in general and the encountered issues.

The 3D imaging of 17 months old medaka in absorption was successful at the CL-Lab. A full-body scan took 2.75 h including manual sample exchange and alignment. This is a comparable acquisition time to that of the high-resolution setup developed by Weinhardt et al. [61]. The difference is a much lower resolution achieved in the laboratory setup.

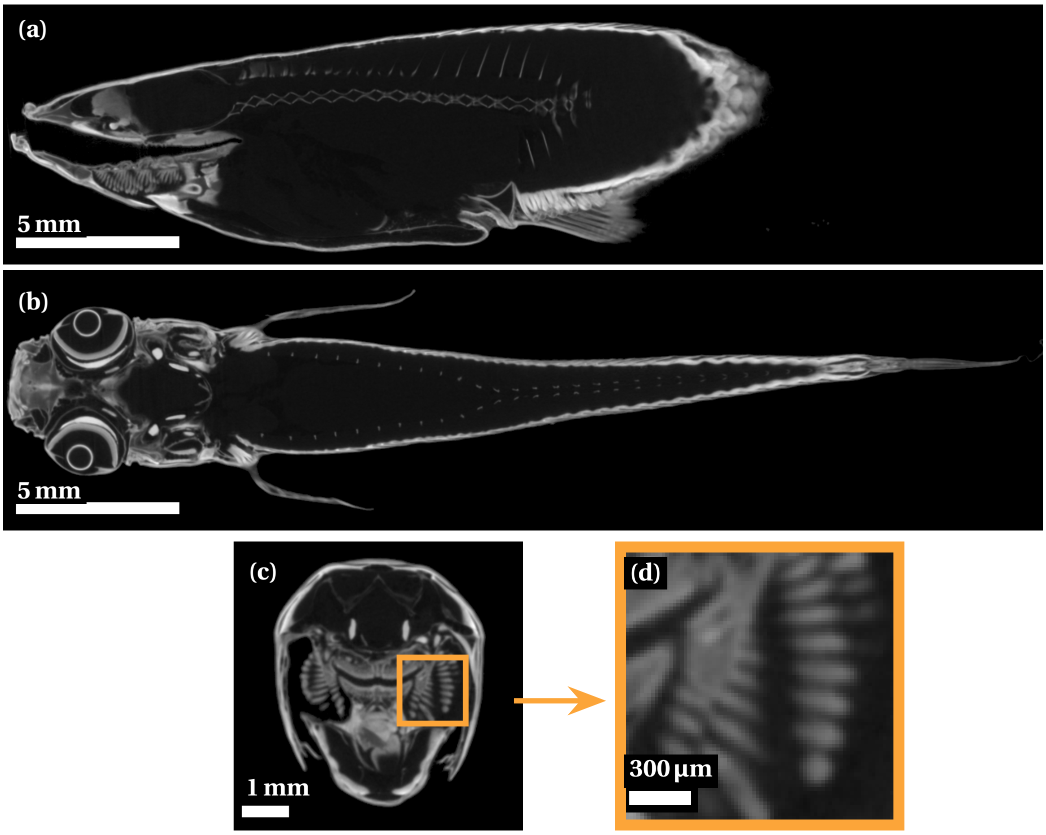

Figure 3.5.: (a) Sagittal, (b) coronal and (c and d) axial slices of a 17 months old medaka. The medaka is only stained in regions close to the surface. (d) The gill filaments are not resolved. The grey values display the linear attenuation coefficient from 0 cm^{-1} to 0.64 cm^{-1} (black to white).

The medaka were stained only in regions open to the outside. This indicates a low penetration depth of the PTA staining, which had been developed for two months old medaka of half the size. For the imaging of larger medaka, an adapted staining is required.

As expected, the resolution was not high enough to resolve the complete structure of the medaka gills. It can be increased by adaption of the source-sample-distance. If the magnified medaka no longer fits into the field of view (FOV) of the detector, additional CT scans with translated sample positions are necessary.

Regarding high-throughput imaging, short acquisition times are desirable. A higher tube voltage or power increase the signal on the detector and allow for shorter exposure times. However, an increased power increases the source size of the x-ray tube and limits the resolution of the system. An increased voltage might lead to beam hardening artefacts due to the higher mean energy of the x-ray beam.

To conclude, absorption imaging at a laboratory is easily implemented. The FOV is adaptable and allows imaging of relatively large samples. An adaption of the staining to the sample size is required. Due to the long acquisition time, absorption imaging in a single laboratory is not suited for high-throughput imaging. However, several laboratories might be operated in parallel to scan large sample numbers.

3.1.4. Conclusion

In this section, absorption imaging was successfully implemented in a synchrotron as well as a laboratory setup. The data acquisition time at the laboratory setup was about five times longer than that at the synchrotron setup. PTA staining increased the soft tissue absorption contrast and allowed differentiation of relevant and tissues. Selected organs could be segmented in 3D using the synchrotron data. However, the staining adapted from previous work was insufficient in most medaka. It did not penetrate the complete body resulting in unstained areas with low contrast. Additionally, the embedding material formed bubbles during the CT scans in the synchrotron pink beam. For the use of absorption imaging in the high-throughput pipeline, a reliable full-body staining and a stable embedding material would be required to ensure repeatable results.

3.2. Grating interferometry

Grating interferometry (GI) offers the possibility to access absorption, phase, and visibility contrast in a single measurement at the cost of a longer acquisition time in comparison to absorption or single distance phase imaging. The flowchart of the imaging pipeline (figure 3.6) gives an overview of the tasks needed to scan and reconstruct a single medaka in GI. As a short acquisition time is favourable in high-throughput imaging the according task of CT acquisition (highlighted) is studied in detail in this section. In grating interferometry, the acquisition time depends on the chosen reconstruction algorithm (section 2.4). The Fourier approach requires 2^n equidistant grating steps over a grating period with $n \geq 2$ and $n \in \mathbf{N}$ for image reconstruction. Measuring over two instead of one period and with large n increases the image quality. In comparison, the optimum for the algebraic approach is only five steps measured over two grating periods.

This section presents the influence of different numbers of steps and grating periods as well as the used reconstruction algorithm on the image quality. As medaka embedded in agarose yielded no contrast, dried medaka are used as samples.

3.2.1. Sample preparation

Four two months old medaka were sacrificed and fixed. Two medaka were additionally stained with phosphotungstic acid (PTA). Fixation and staining followed the sample preparation presented in table 3.1 and were carried out at IBCS by Narendar Aadepu. Table 3.4 gives the details on the preparation for each sample.

Table 3.4.: List of samples for the evaluation of grating interferometry in a laboratory setup. The abbreviations are listed in table A.1.

Sample	age	fixation	staining
M1	2 month	4 % PFA/ 1 % GA	–
M2	2 month	4 % PFA/ 1 % GA	–
M3	2 month	4 % PFA/ 1 % GA	0.3 % PTA in 70 % ethanol
M4	2 month	4 % PFA/ 1 % GA	0.3 % PTA in 70 % ethanol

After fixation and staining the medaka were dried using a critical point dryer (Leica EM CPD300, Leica) by Janes Odar (IPS, KIT). The medaka were placed in Eppendorf tubes on top of silica gel and crumpled paper to prevent rehydration. Additionally, the tubes were sealed using hot glue.

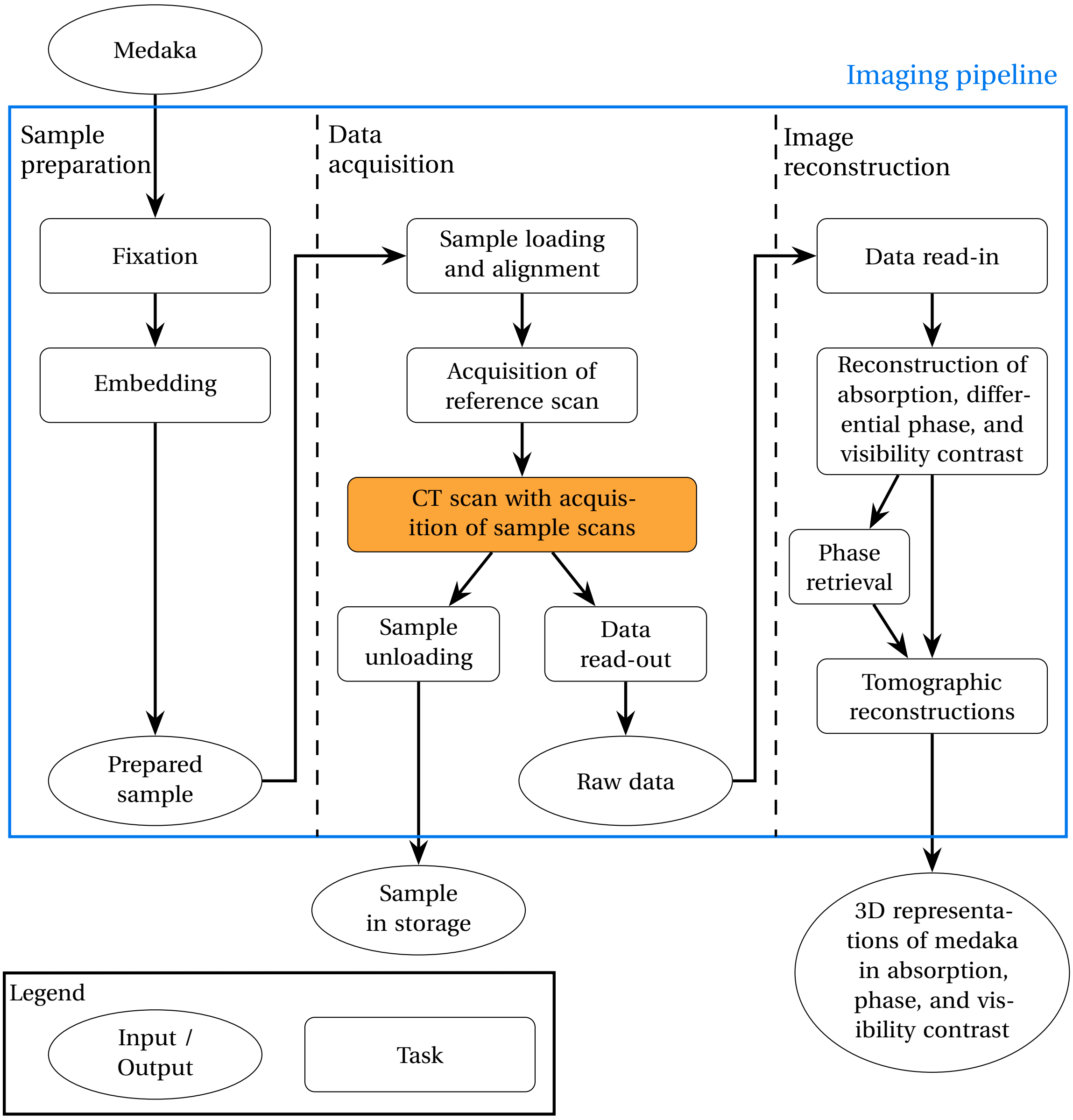

Figure 3.6.: Workflow of a single medaka in grating interferometry. Highlighted are the tasks that are analysed for optimization in this section.

3.2.2. Imaging setup

A Talbot-Lau grating interferometer was set up at the CL-Lab (sections 2.4 and 2.6.2). The interferometer is a symmetric setup with 557 mm inter-grating distance in third Talbot order. Table 3.5 lists the gratings' properties. The gratings were placed as close as possible to the x-ray tube and the detector. The grating lamella were vertically aligned. The symmetry of the setup results in a magnification of two and thus in a maximum resolution of 74.8 µm using the Dexela detector. The maximum field of view corresponds to the area of the analyser grating G2 of 50×50 mm^2. The samples were placed as close as possible behind the phase grating. This maximizes the magnification and the propagation distance of the diffracted wave for best phase contrast. The tube voltage of the polychromatic beam was set to 55 kV to get a maximum in the x-ray spectrum at 40 keV, the design energy of the phase grating G1. The tube power was 100 W. The exposure time per projection was 2 s. Each sample was scanned over four grating periods with 40 imaging steps per period resulting in an acquisition time of 320 s per sample.

Table 3.5.: Properties of the gratings used in the Talbot-Lau interferometer. The gratings were fabricated by the Institute for Microstructure Technology (KIT).

Grating	position	grating area / mm^2	period /µm	material	height /µm	phase shift
1067-5	G0	50×50	4.8	gold	120	
0851-2	G1	50×50	4.8	gold	7.8	π at 40 keV
1105-5	G2	50×50	4.8	gold	120	

The Fourier analysis was performed with four or eight equidistant steps per period over one (F4P1 and F8P1), two (F4P2 and F8P2) and four periods (F4P8 and F8P8). The algebraic analysis used five equidistant steps over two periods. The calculation uses only the first two periods of the phase stepping scan for algebraic reconstruction. To calculate the CNR, a region in the stomach of each sample was selected in addition to a background region just outside the Eppendorf tube.

3.2.3. Results

The three contrasts yielded complementary information (figure 3.7). Differential phase and visibility contrast are detectable only parallel to the vertical grating lamella. The hot glue (top left, red arrow) was clearly visible in absorption and differential phase (figures 3.7a and 3.7b). In visibility contrast (figure 3.7c), only its contour was displayed. Silica gel (bottom left and right, dark green arrows) and crumbled paper ((bottom mid, orange arrow)) showed differing contrasts in absorption and visibility. Whereas silica gel led to a strong absorption contrast, the paper showed almost no absorption. In visibility contrast, silica gel resulted in low contrast, whereas the paper yielded a strong contrast. The shape of the silica gel and the paper was visible in differential phase contrast. In the dried medaka, high absorbing areas also yielded a high visibility contrast. The contrast of bones, especially the skull, was stronger in visibility contrast. While the eye lenses could be sensed in absorption contrast, they were not detectable in visibility contrast. The differential phase contrast gave additional information on the outer shape. It enhanced the contrast of inner organs and especially the eye lenses. The retrieval of the one-dimensional phase contrast (horizontal) from the differential phase resulted in strong horizontal artefacts from the integration of noisy areas. The samples were hardly detectable except for the hot glue. Grating defects resulted in horizontal stripes in absorption and differential phase images, as well as a small artefact in the top mid in all three contrasts.

In the comparison of different reconstruction methods, the intensity of moiré fringes increased with a decreasing number of grating steps in Fourier reconstruction (figure 3.8). The remaining moiré fringes in algebraic reconstruction were comparable to F8P1 (8 steps over 1 period) and F4P2 (4 steps over 2 periods), both calculated using eight grating steps.

The CNRs confirmed the visual impression (see figure 3.9). It generally increased with increasing step number or period coverage in the Fourier approach. The CNR of the algebraic approach was comparable to F8P1 and F4P2 in absorption and visibility contrast for all samples and for M1 and M3 in phase contrast. The CNR of the stained samples M3 and M4 was higher in absorption

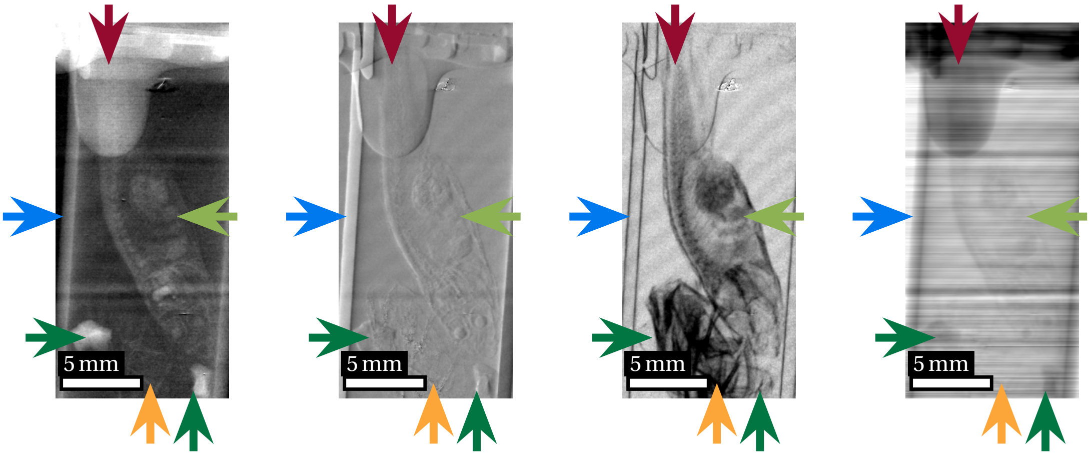

(a) Absorption contrast. **(b)** Differential phase. **(c)** Normalized visibility. **(d)** 1D phase.

Figure 3.7.: (a) Reconstructed absorption, (b) differential phase, (c) visibility contrast, and (d) integrated one-dimensional phase contrast of an unstained, dried medaka (sample M1). The images are reconstructed using the Fourier approach with eight steps per period over four grating periods, The displayed grey values range (a) from 0 to 0.2 (black to white) in absorption contrast. (b) In differential phase, the grey values range from $-\pi/2$ to $-\pi/2$ (black to white). (c) In visibility contrast, the grey values range from 0.2 to 1.1 (black to white). (d) The integrated one-dimensional phase ranges from -64π to -5π (black to white).

contrast in algebraic approach and with a smaller number of steps in Fourier approach than that of the unstained samples M1 and M2. The CNRs were comparable for all samples with a large number of steps in Fourier approach. In phase contrast, algebraic approach and F4P1 (4 steps over 1 period) yielded the lowest CNR.

Due to the expected long acquisition time, no CT scan with medaka was run.

3.2.4. Discussion

The study showed the advantage of GI in comparison to other x-ray imaging methods by obtaining absorption, differential phase, and visibility contrast in a single measurement. Each contrast provides additional information of the sample. Absorption provides the absorption of different materials. Differential phase gives an impression of the shape and enhances the contrast of low absorbing structures. Visibility provides information on scattering as well as unresolved phase contrast. Thus, it is most sensitive to strong changes in a sample, for example at edges. The integration of the differential phase yielded strong artefacts. For phase retrieval, less noise is required. This could be achieved with a more stable grating setup to reduce moiré fringes, higher grating quality, or application of a smoothing function as a gaussian blur prior to integration. Due to the orientation of the gratings, the information on phase and visibility is strong on vertical and low on horizontal features (compare theory in section 2.4). A 2D grating or an additional stepping with sample or gratings rotated by 90° would yield the information in a second direction.

In the comparison of the reconstruction methods (section 2.4), the Fourier approach yielded the best image quality with eight images per period and covering four periods. This meets the expectations, as more images increase the number of points defining the phase stepping curve.

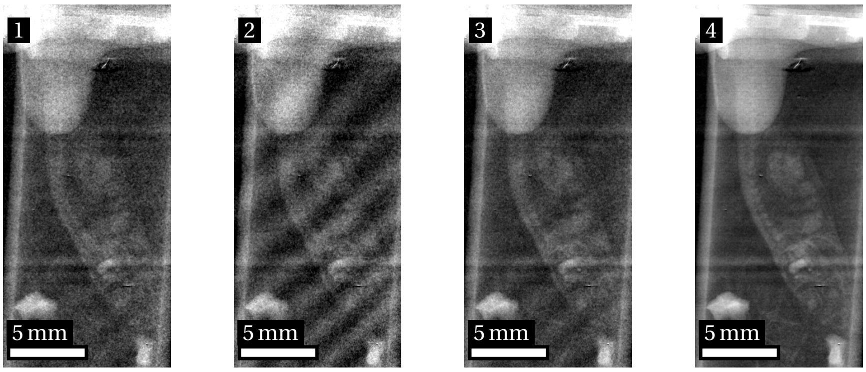

(a) Absorption contrast.

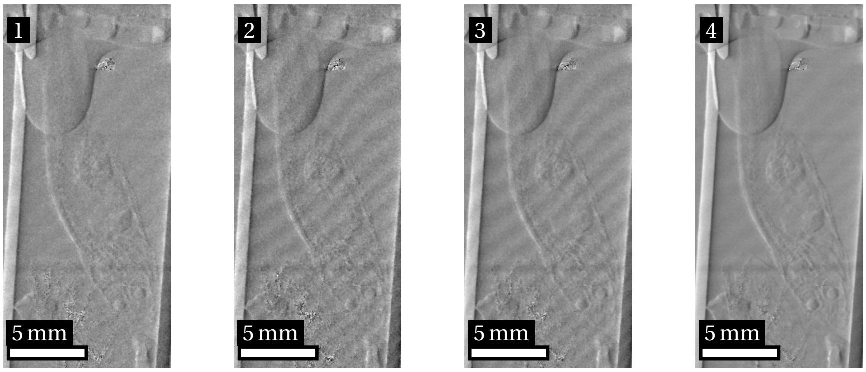

(b) Differential phase.

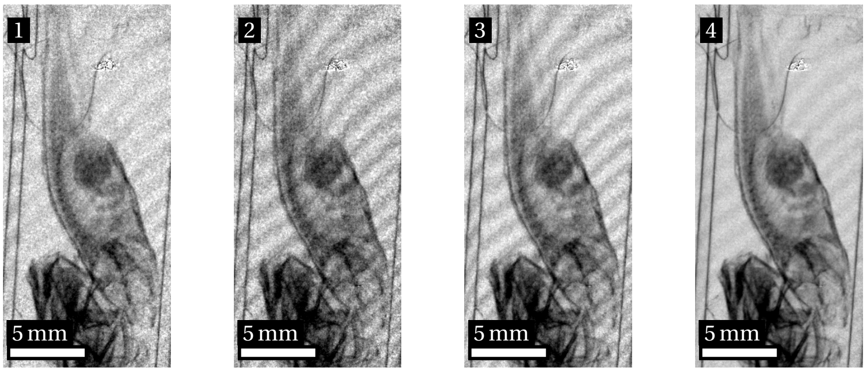

(c) Normalized visibility.

Figure 3.8.: Comparison of the projections of a two months old, unstained, dried medaka (sample M1) after reconstruction of the contrasts in grating interferometry. The contrasts were reconstructed from the same phase stepping scan using (1) algebraic reconstruction and five steps covering two grating periods, or Fourier reconstruction with (2) four steps or (3) eight steps covering one grating period or (4) eight steps per period covering four grating periods. Displayed are (a) absorption contrast, (b) differential phase, and (c) visibility contrast. The image quality increases with the use of algebraic reconstruction or a larger number of steps in Fourier reconstruction. The displayed grey values (black to white) range (a) from 0 to 0.2 in absorption contrast. (b) In differential phase, they range from $-\pi/4$ to $-\pi/4$ for the algebraic reconstruction (1) and from $-\pi/2$ to $-\pi/2$ for the Fourier reconstructions (2,3,4). (c) In visibility contrast, they range from 0.2 to 1.1.

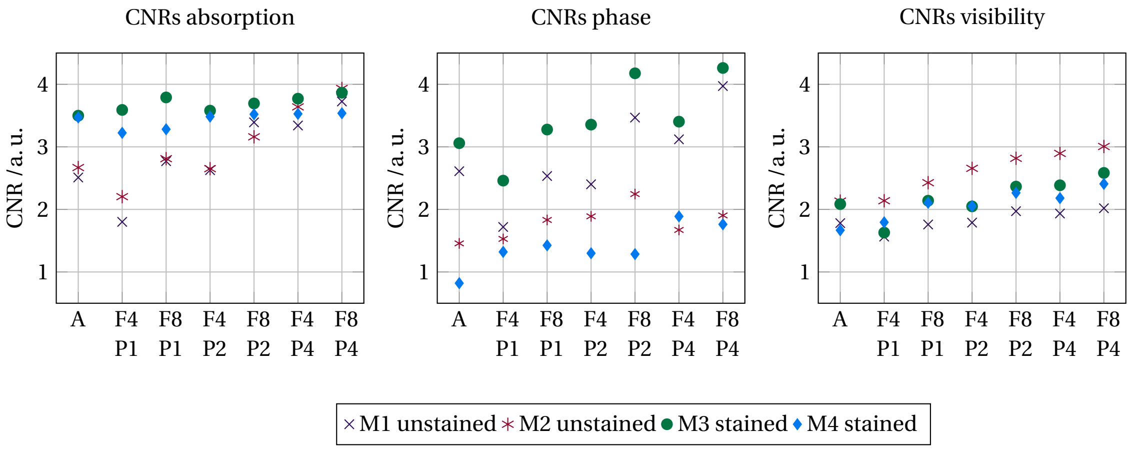

Figure 3.9.: Comparison of the CNR of the three contrasts resulting from different image reconstructions of a phase stepping scan. The samples were two months old, dried medaka. Two medaka were stained, two were unstained. The contrast images were reconstructed from the same phase stepping scan, which covered four grating periods with 40 steps per period. The reconstructions used (A) the algebraic approach with five steps covering two periods and the Fourier approach with four or eight steps per period covering (F4P1 and F8P1) one grating period, (F4P2 and F8P2) two grating periods and four grating periods (F4P4 and F8P4). The CNR increase with an increasing number of steps used for reconstruction.

An increase of the periods makes the measurement more robust towards outliers caused by small movements of the gratings. In addition, it avoids artefacts caused by twin-peaks [39]. Therefore, moiré fringes from reference and sample scan cancel out (section 2.4) in the reconstructed images. The low intensity of the moiré fringes in the algebraic reconstruction indicates a robust method. The CNR slightly increased with the number of images and periods especially in the visibility contrast in the Fourier approach. To conclude, the Fourier approach yields the best image quality with a high number of steps and covered periods in the phase stepping. The algebraic reconstruction is a suitable alternative if a short acquisition time or a low dose are important. It requires but five steps and the results are comparable to eight steps reconstructed with the Fourier approach. With the setup used, the acquisition time per phase stepping scan results in roughly 10 s with algebraic contrast retrieval. This results in at least 6 h of sample scans for a complete CT scan. The instability of the used grating interferometer would require several reference scans during this time. Due to an expected total acquisition time of more than 8 h, running a CT scan with medaka was not considered.

In general, a new grating interferometer would be needed for high-throughput measurements of medaka especially regarding resolution. One approach would be the use of an asymmetric grating setup at the laboratory. It offers the possibility of a higher magnification and thus lower resolution. One requirement is an analyser grating, which is large enough to cover the whole area of the magnified phase grating. Recent research shows first approaches of enlarging the grating area either by assembling smaller gratings [63] or by a modified production [64]. Another requirement is a matching source grating with small area, but a high aspect ratio [1] with a small grating period in a high quality. With the use of a nano focus tube head, a Talbot interferometer without source

---

[1] Ratio between the height of the grating lamella and the grating period.

grating would be sufficient for imaging at the cost of a longer acquisition time. Another approach is the usage of GI in combination with an x-ray beam with high flux density and coherence as provided by synchrotron sources. The advantages are a shorter exposure time and the possibility to use a Talbot interferometer without a source grating due to the high coherent x-ray beam. McDonald et al. [65] demonstrated an approach for a combination of GI and CT measurements on a rat brain with a pixel resolution of 7 µm at the Swiss Light source. This would be sufficient for the measurements of medaka. The acquisition time of 84 min however is too long for high-throughput measurements. Dark-field in-vivo chest imaging of a mouse was demonstrated at the Munich Compact Light source [15]. The time resolution was 0.1 s and a pixel size of 172 µm. In this case, the resolution is not sufficient for imaging of medaka.

To conclude, GI is well suited for the imaging of biological samples. Absorption, differential phase, and visibility contrasts give complementary information on the sample. Further research is required to combine high-resolution with short acquisition times for high-throughput imaging of medaka and other small vertebrates.

3.3. Single distance phase contrast imaging

Phase contrast imaging is well suited to display low absorbing materials such as biological soft tissue. Figure 3.10 shows the flowchart for an imaging pipeline for phase imaging of a single medaka. The highlighted tasks are analysed and discussed in this section.

For the imaging pipeline, Paganin phase retrieval is chosen as phase imaging method (section 2.3). It is a single distance propagation method, which allows for short acquisition times. In addition, it tolerates the use of a polychromatic beam as well as an inhomogeneous sample as medaka. Propagation-based phase imaging demands the use of a sufficiently coherent x-ray beam. Therefore, it is implemented at the synchrotron.

This section presents phase measurements using Paganin phase retrieval on two months old medaka and discusses the resulting tomograms regarding image quality and resolution.

Sample preparation

Two months old medaka were sacrificed and fixed in 4 % PFA/ 1 % GA for 3 days at room temperature. Afterwards, they were embedded in 0.5 ml Eppendorf tubes using 4 % low melting agarose (LMA). The preparations were performed at the IBCS by Narendar Aadepu.

Imaging setup

The imaging experiments were carried out at the UFO station (section 2.6.1) at KIT synchrotron. The x-ray beam was filtered with 1.5 mm aluminium and the resulting mean energy is about 22 keV. The detector system was the Elya macroscope with 2.5× magnification resulting in a FOV of 8.87 mm width. The vertical FOV was cropped to 1536 pixel (about 6.76 mm) to avoid the noisy regions at the top and bottom of the detector. The effective pixel size is 4.4 µm. The propagation distance between sample and scintillator was set to its optimum of approximately 165 mm (equation 2.28). The samples were measured using helical CT scan with 2000 projections per 180° turn. The vertical travel speed was adapted to the exposure time of 40 ms per projection. The vertical travel per 180° covered 1336 pixel (about 5.34 mm). All medaka were completely scanned with 29 mm vertical travel. The time for image acquisition sums up to roughly 8 min. The sample changer robot only aligns the bottom of the sample. Therefore, the vertical alignment of each Eppendorf was checked prior to the experiment to ensure that the sample stays inside the FOV during travel.

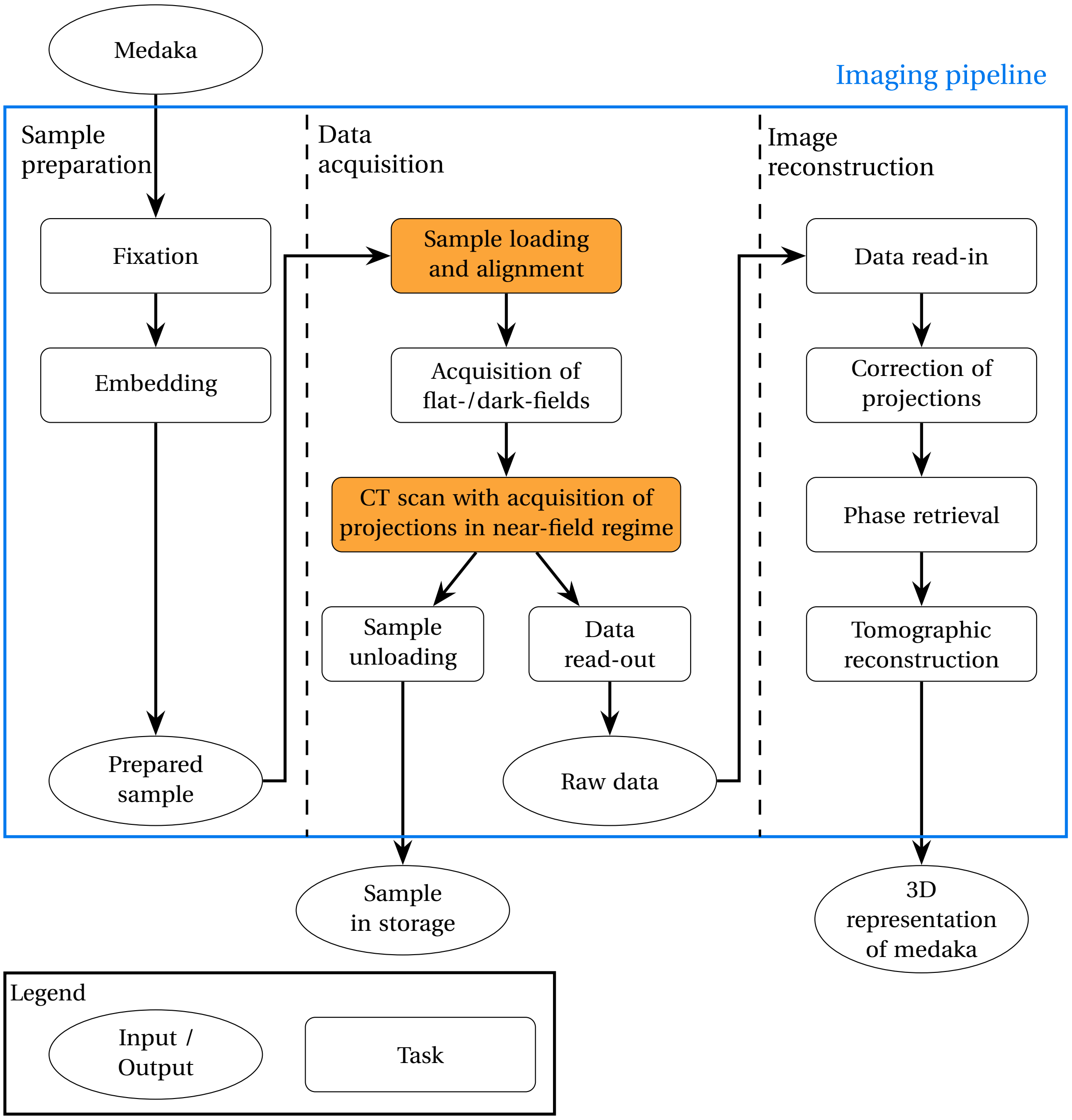

Figure 3.10.: Workflow of a single medaka in phase imaging. Highlighted are the tasks that are optimized and analysed in this section.

The Paganin phase retrieval implementation of the UFO platform was used for phase retrieval. The unretrieved absorption data was used to automatically find the reconstruction parameters for tomographic reconstruction.

To generate sagittal and coronal CT slices for display in this thesis, the tomogram was binned by a factor of two prior to alignment in Amira 2019.2. The phase-retrieved reconstruction was registered onto the unretrieved data to ease comparison.

Results

The results are divided into the analysis of the time effort, the image quality, and the resolution.

The analysed time effort divides into measurement and post-processing. The measurement resulted in 16 min per medaka including sample exchange and camera read-out. The up-to-date camera read-out took the longest time. Each helical CT scan covered the entire length of an Eppendorf tube whereas the medaka filled only about half of it. The computation time of helical CT reconstruction was about 1.5 h. It returned the complete tomographic volume without further processing. Each reconstruction needed manual assistance based on the absorption data to find the exact reconstruction parameters.

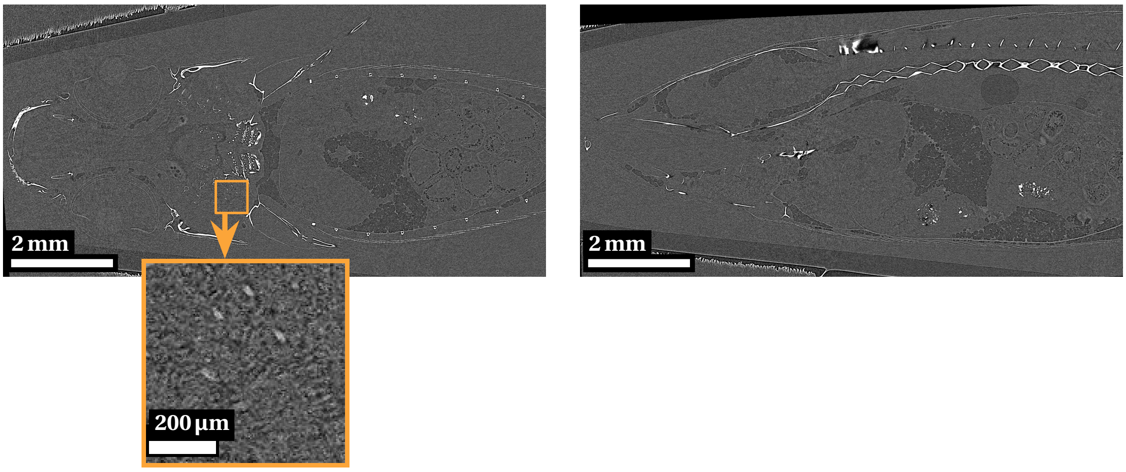

(a) Reconstruction without phase retrieval.

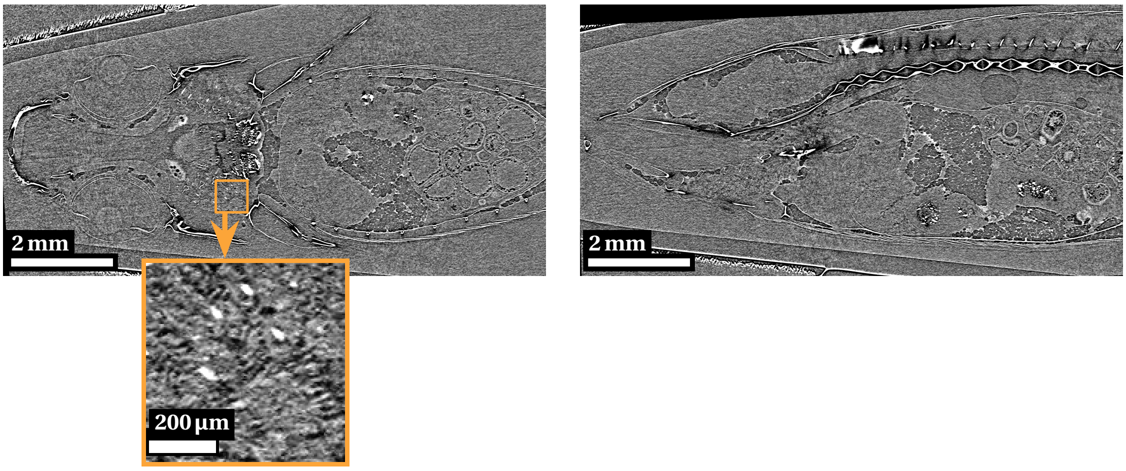

(b) Reconstruction with phase retrieval.

Figure 3.11.: Comparison of CT reconstruction of the same data set (b) with and (a) without Paganin's phase retrieval. Displayed are coronal (left) and sagittal (right) slices through a two months old, unstained medaka. The position of the slices is identical in both representations. The propagation distance was 16 cm. (b) Phase retrieval significantly increased soft tissue contrast in comparison to (a) the reconstructed absorption. The grey values range from (a) $-1.14\,\mathrm{cm}^{-1}$ to $3.94\,\mathrm{cm}^{-1}$ and (b) from −2.27 mm to 3.05 mm (black to white).

The image quality and resolution were evaluated by visual assessment. Paganin phase retrieval significantly increased the contrast and thus the image quality of soft tissue borders in comparison to a reconstruction based on absorption contrast (figure 3.11). In both reconstructions, the bones were most prominent. The enhanced contours allowed to differentiate inner organs. Different tissues, for example in the brain, could not be distinguished. Semi-automated segmentation failed due to low contrast differences between adjacent structures. Regarding the resolution, the gills (detailed view) were resolved in some areas. In the other areas, the gills were either unresolved or not visible due to low contrast. An additional result is that the embedding LMA was stable during roughly 9 min irradiation with filtered white beam.

3.3.1. Discussion

Propagation-based phase contrast imaging was implemented and tested for 3D imaging of two months old medaka. The chosen phase retrieval method was the Paganin approach (section 2.3).

Regarding time effort, a helical CT scan took 16 min per medaka including sample exchange and camera read-out. The camera read-out took the longest time. Its duration could be reduced with a smaller amount of data, for example by shorter vertical travel. The vertical travel was more than sufficient to display the complete medaka. However, the vertical position of medaka inside the Eppendorf tube varied. It might be possible to embed the medaka in smaller sized Eppendorf tubes to reduce vertical travel. In addition, a smaller size would ease alignment of the samples in the horizontal FOV. The computation of helical CT reconstruction took 1.5 h per medaka. However, the correlation-based optimization of reconstruction parameters failed. The parameters could be found manually. For large campaigns, the automated detection of the UFO platform [48] should be optimized for phase contrast.

Regarding the image quality, Paganin phase retrieval successfully enhanced the soft tissue contrast in unstained medaka in comparison to absorption contrast. The contours of inner organs were well displayed which is sufficient for morphometric analysis. As expected, (see section 4.2), LMA formed no bubbles during the tomographic scan. Semi-automated segmentation was not possible due to the low contrast difference between adjacent structures. The resolution of the gills showed local differences, which can result from a low contrast or the size being at the resolution limit. The contrast at the gills might be lower due to the surrounding skull. The absorption and the refractive index decrement of bone is higher than that of the surrounding tissue violating the assumption of a homogeneous material for Paganin's phase retrieval (section 2.3). Implementation of the multi-material approach proposed by Beltran et al. [66] might overcome this issue. Prerequisite is the known thickness of the different materials. The thickness of bones can be retrieved from an absorption reconstruction for the bones. The thickness of the Eppendorf tube is known from its data sheet [62], which also gives the maximum thickness of LMA and medaka. The thickness of medaka can be measured.

A simulation on polymethylmethacrylate (PMMA, $(C_5O_2H_8)_n$) spheres (figure 3.12) demonstrates the resolution limit of the imaging setup used (figure 3.12 (a)). The spheres with a diameter of 8.8 µm (upper left pack) are not resolved. Thus, gill filaments with a size of 10 µm [8] cannot be resolved. The other sphere packs have a diameter of 17.2 µm (top right), 26.4 µm (bottom left), and 35.2 µm (bottom right). A higher magnification (figure 3.12 (b) and (c)) increases the resolution for the measurement of the diffraction pattern resulting in better resolution and contrast. An increased propagation distance and thus broader diffraction pattern further improves resolution and contrast (figure 3.12 (d), (e), and (f)). To satisfy equation 2.28, the x-ray source size is adapted according to propagation distance and detector resolution in all simulations. The simulations show the need for setup adaption in imaging of medaka. However, a higher magnification or a larger source size decrease the available FOV, which was matched to the size of a medaka. A compromise with the existing setup could be 5× magnification combined with 360° CT scans at the cost of a longer measurement time and a longer post-processing. 360° scans allow to cover a horizontal area almost double the 4.4 mm FOV of the 5× magnification setup. Thus, the Eppendorf tube should still fit into the scanned FOV. In addition, a 360° helical CT reconstruction algorithm or the use of the step CT configuration would be required.

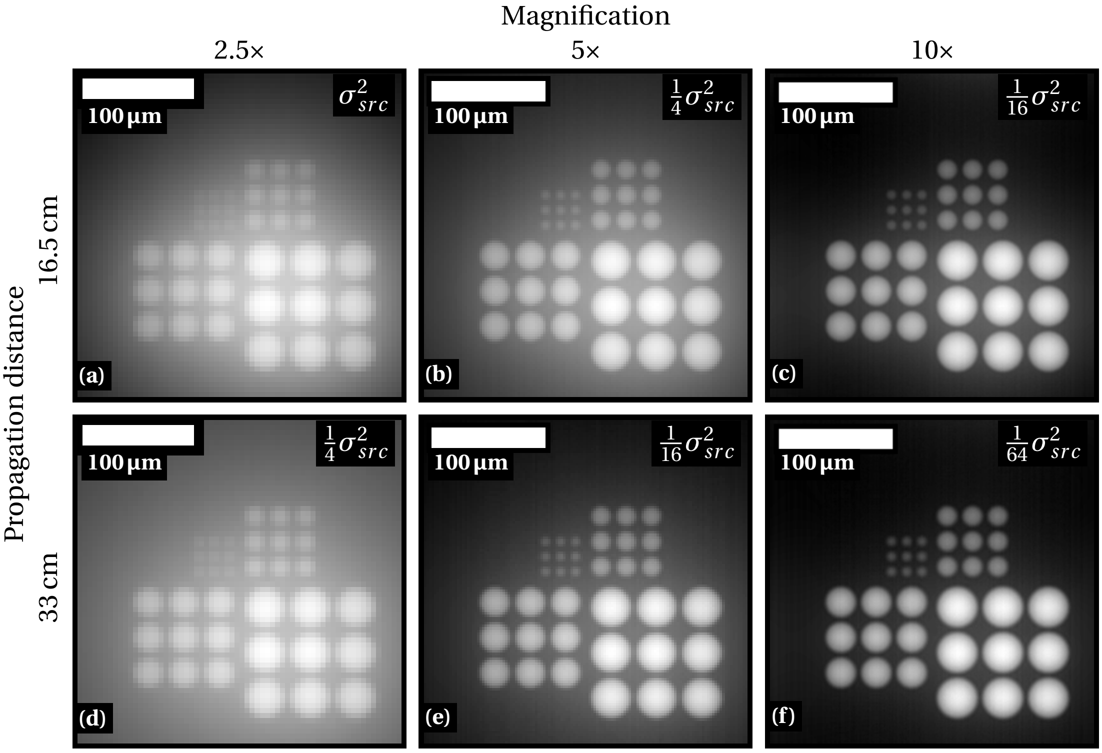

Figure 3.12.: Simulations of the reconstructed thickness of polymethylmethacrylate (PMMA) spheres using Paganin phase retrieval. The diameters of each set of nine spheres are (top left) 8.8 µm, (top right) 17.6 µm, (bottom left) 26.4 µm, and (bottom right) 35.2 µm. The distance between the spheres in each set is 4.4 µm. The parameters of the x-ray beam for the simulation are the same as in the experimental phase retrieval performed on medaka. The simulated camera corresponds to the PCO.dimax with 256×256 pixel. The magnifications are 2.5×, 5×, and 10×. The resulting effective pixel sizes are 4.4 µm, 2.2 µm, and 1.1 µm, respectively. In the simulations, magnification, propagation distance, and source size σ^2_{src} are adjusted, so that equation 2.28 for optimum phase contrast is satisfied. A higher magnification or a longer propagation distance, both coupled with a smaller source size, increase the resolution and the contrast. The grey value range (black to white) of the reconstructed thickness is adapted to the minimum and maximum of each image. It is (a) 1.21 µm to 1.97 µm, (b) 1.04 µm to 1.60 µm, (c) 2.00 µm to 2.43 µm, (d) 2.05 µm to 2.32 µm, (e) 5.38 µm to 5.62 µm, and (f) 5.70 µm to 5.89 µm.

To conclude, single distance phase imaging with Paganin's phase retrieval yielded an enhanced soft tissue contrast. The current configuration of the imaging setup is not suited for full-body imaging of medaka in the required resolution. Additionally, the overall phase contrast in the medaka is low. Both can be optimized with an adaption of the imaging setup.

3.4. Conclusion

In this chapter, grating interferometry, absorption imaging, and single distance phase contrast imaging were applied on medaka and analysed regarding acquisition time, image quality, and resolution.

Absorption imaging has been demonstrated at the CL laboratory (section 2.6.2) and the UFO station (section 2.6.1) at KIT synchrotron. All relevant structures and organs were resolved. PTA staining increased the contrast of the low absorbing soft tissue sufficiently. The contrast between different tissues allowed to distinguish even brain regions and retinal layers. Dissolvement of fat and fatty tissue was the only alteration detected on the sample due to the staining. The PTA staining did not penetrate all medaka completely resulting in areas with low to no contrast. The embedding material agarose formed bubbles during the CT scan. This resulted in motion artefacts and locally reduced resolution in the reconstructed tomograms.

Grating interferometry has been demonstrated at the CL laboratory. It provides absorption contrast, phase contrast, and visibility contrast in a single experiment. The contrasts complement each other, which gives an overall picture of the sample's properties. The minimum number of projections per rotation step in the CT scan is five to ensure sufficient image quality. A larger number of projections increases the image quality. For imaging of medaka, another interferometer is necessary to achieve the required resolution.

Single distance phase contrast imaging was demonstrated at the UFO station using Paganin phase retrieval. The resulting contrast was sufficient to distinguish different organs but too low for semi-automated segmentation. The resolution differed locally. Using a higher magnification will improve resolution and contrast at the cost of a longer measurement time.

Under the aspect of the use in the high-throughput imaging pipeline for morphometric analysis, absorption contrast imaging is chosen for further optimization due to the excellent tissue differentiation. The synchrotron setup is preferable to the laboratory setup for high-throughput campaigns despite limited access. Scanning 100 medaka in absorption at similar resolution takes about one day at the UFO station as opposed to 31 days at CL-Lab. The PTA staining allowed to differentiate between different organs and tissues. A higher staining efficiency and an embedding material stable under x-ray radiation are desirable for large scale measurement campaigns.

Chapter 4

Optimization of sample preparation and imaging setup for absorption computed tomography of medaka at a synchrotron

From the x-ray imaging techniques evaluated in this thesis, absorption micro computed tomography (µCT) was chosen for further optimization regarding imaging of medaka. The remaining challenges from the previous chapter are a low staining efficiency and bubble formation in the embedding material. The staining showed significant differences between the samples regarding penetration depth and homogeneity. Furthermore, a faster and fully automatized post-processing is desirable.

This section discusses optimizations of the sample preparation and the imaging setup regarding a higher image quality and a reduction of processing time (see figure 4.1). The first part discusses the influence of different parameters in the staining protocol on the staining efficiency. Then, different embedding materials are analysed for their application in pink beam CT at the synchrotron. Finally, step and helical CT are compared regarding image quality and time effort from measurement to final 3D volume.

4.1. Optimization of PTA staining

In the previous experiments (section 3.1), the phosphotungstic acid (PTA) staining showed a significant difference in efficiency between different samples. High-throughput imaging requires a sample preparation that ensures a complete staining in each sample. Studies reporting penetration issues with PTA [67–70] propose sample sizes up to a few millimetres or extraction of the region of interest from the sample to ensure a complete staining. Both approaches are no option for full-body imaging of medaka. The aim is to develop a sample preparation based on PTA, which overcomes the penetration limit and provides a homogeneous and complete staining of the sample. An exchange of PTA for another staining agent is not considered as it is resulted as the best for full-body imaging of medaka [61]. In addition, PTA binds unspecifically to positive charges [71], allows excellent tissue differentiation [9], and shows excellent results at high resolutions in histotomography [72].

In general, the sample preparation comprises the fixation, the staining, and the embedding of the sample. Embedding has no influence on the staining and will be considered in section 4.2. The following paragraphs discuss the influence of the detailed steps of fixation and staining on staining efficiency as well as possible actions to improve the staining efficiency.

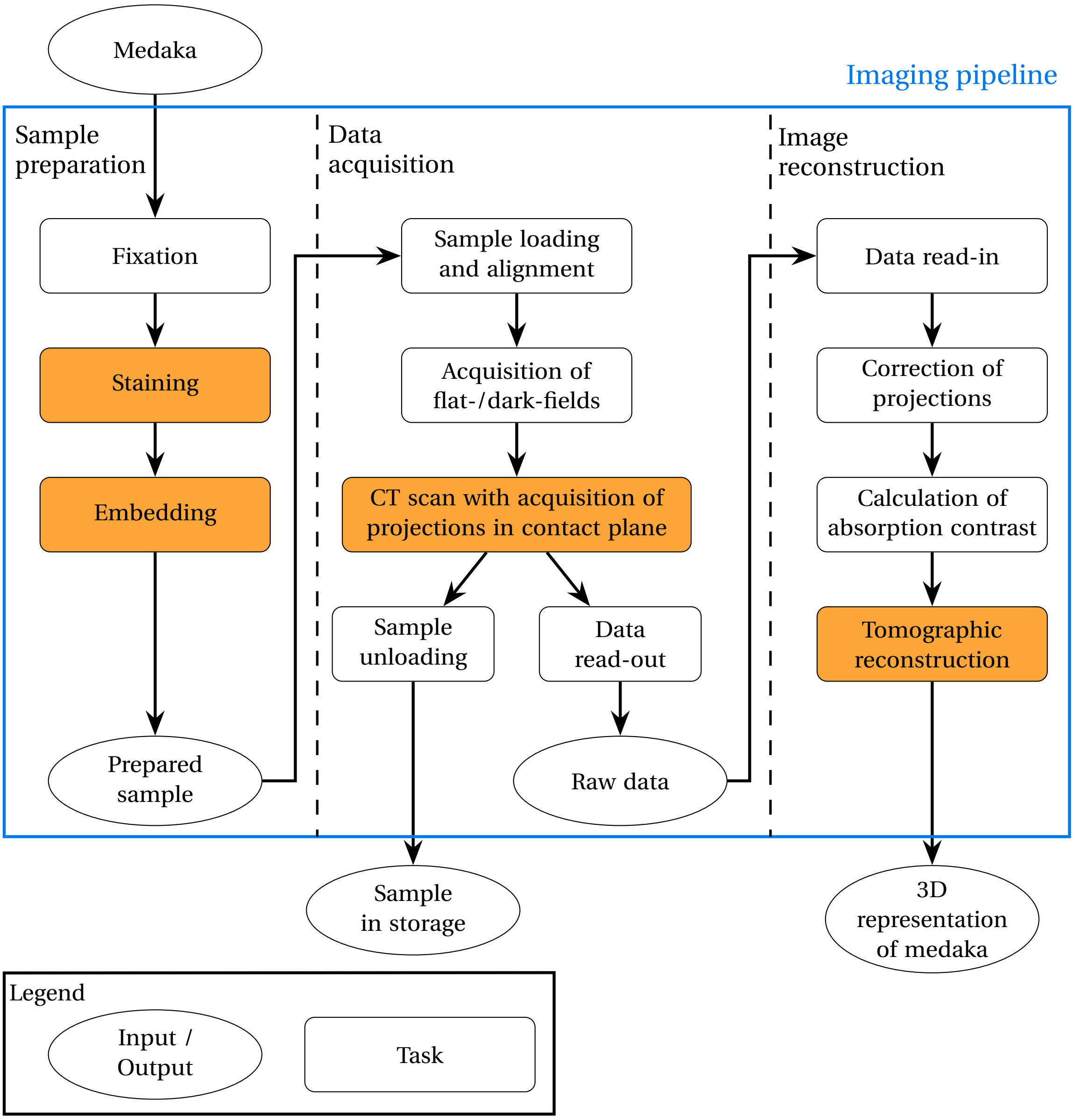

Figure 4.1.: Workflow of a single medaka in absorption imaging. Highlighted are the tasks that are analysed in this chapter to optimize the performance of the imaging pipeline.

A strong fixation preserves the sample in its natural shape and allows storage but lowers the diffusion speed and penetration depth of PTA [68]. Weinhardt et al. [61] use a mixture of 4 % paraformaldehyde (PFA) and 1 % glutaraldehyde (GA) for fixation. GA is a strong fixative, which might hinder the penetration of the staining agent. The staining starts with a dehydration to remove water from the sample. If the dehydration occurs too fast or the fixation is not strong enough, the sample might shrink. Therefore, the concentration of the dehydration agent is increased stepwise until reaching the concentration used in the PTA solution. The used dehydration ethanol acts like a fixative and hardens tissue [73] and thus might decrease the penetration of PTA. A different dehydration agent therefore might increase the penetration depth of PTA. A possible replacement is acetone. It influences the PTA molecule similar to ethanol [74] so that PTA binds to positively charged groups by electrostatic force [71]. As positively charged groups are present in all tissues, this ensures a homogeneous staining.

In the staining step, the staining efficiency might be increased with a higher PTA concentration, a higher temperature, or a longer staining duration to ease diffusion. Important is a short staining time, as a long staining induces shrinkage [75].

Washing steps in between fixation, dehydration, and staining remove excess chemicals.

This section presents different experiments to test the influences of the fixation, the dehydration agent, the staining temperature, the PTA concentration, and the staining duration on efficiency of PTA staining in adult medaka. The analysis of the tomograms and the evaluation of the staining efficiency follow the guidance on image analysis in section 2.6.4. The samples for the first experiments were 17 months old medaka, as they were easier available. Their cross section was about 7 mm×4 mm at the thickest parts and they were about 30 mm long. The results are a starting point for the optimization of the staining protocol for 13 weeks old medaka of about half the size. They are similar in size of 10 weeks old medaka, which will be the age of the adult medaka for phenotype-genotype correlation studies to minimize the time needed for breeding.

4.1.1. Sample preparation

Medaka were sacrificed and stained according to the basic protocol (table 4.1) adapted from Weinhardt et al. [61]. Further details on the staining are stated in the according section of each experimental series. If not noted otherwise, the ambient room temperature during dehydration and staining was 22 °C. All medaka were embedded in Eppendorf tubes using agarose after the staining. The sample preparation was performed at the IBCS by Narendar Aadepu.

Table 4.1.: Basic staining protocol for a full-body staining of two months old medaka adapted from Weinhardt et al. [61]. Chemicals were exchanged every 48 h. The abbreviations are listed in table A.1.

Step	Agent	Duration
Fixation	4 % PFA/ 1 % GA	3 days
Washing	PBS	3×10 min
Dehydration	10 %, 25 %, 50 %, and 70 % ethanol	10 min each step
Staining	0.33 % PTA in 70 % ethanol	3 days
Washing	PBS	3×10 min

4.1.2. Imaging setup

The CT measurements were carried out at the CL-Lab (see section 2.6.2). The chosen tube voltage was 40 keV to mimic the energies provided at the beamline. The power was 15 W. Images were acquired using the PerkinElmer detector. Each 360° CT scan consisted of 2048 projections with 4 s exposure time each. This results in a duration of 2.5 h per CT scan. The resolution of the setup was adapted for each experimental series in dependence of the sample size. The aim was to scan each medaka in a single CT scan with the highest resolution achievable.

4.1.3. Influence of fixation on staining efficiency

This experimental series investigated the influence of fixation on the staining efficiency and on tissue preservation.

Samples and effective pixel size

Three 17 months old medaka of the inbred line 2-3 (O-GFP) were prepared with different fixatives as stated in table 4.2. Washing, staining, and embedding were performed according to the basic staining protocol (table 4.1).

Table 4.2.: Staining variations.

Sample	fixation
201804_0006	2 % PFA
201804_0005	4 % PFA
201804_0002	4 % PFA/ 1 % GA

The sample placement resulted in an effective pixel size of 17.3 µm.

Results

The histogram analysis of the segmented brains, livers, and tail muscles (table 4.3) yielded an improved staining efficiency with decreasing fixation. 68.70 % of the brain, 98.25 % of the liver and 89.13 % of the tail muscle remained unstained in the medaka fixed with 4 %PFA/1 % GA. Without GA, the unstained fractions reduced to 0 % for brain 0.02 % for the liver, and 11.95 % for the tail muscle. The unstained fraction further decreased to 0 % for brain and liver and 0.01 % for the tail muscle in the medaka fixed with 2 % PFA.

A visual analysis of the tomograms of the different medaka confirmed the results of the histogram analysis (figure 4.2). The fixation with 4 % PFA/ 1 % GA resulted in a staining of the skin and other areas open to the outside, as the gills. Inner organs remained unstained. The fixation with 4 % PFA led to completely stained inner organs. For example, the ovaries are clearly visible. However, a further decrease of the fixation to 2 % was required to achieve a complete staining of the tail muscle. No shrinkage was detected in the medaka fixed with either concentration of PFA, in particular the brains filled the cranial cavity. The shrinkage of the medaka fixed with 4 % PFA/ 1 % GA was not accessible due to the insufficient staining of inner organs.

Conclusion

The experimental series on fixation showed that a decrease of the amount or concentration of fixatives improves the staining efficiency. The omission of GA thereby had a stronger effect than a reduced PFA concentration as GA is a stronger fixative than PFA. No shrinkage was detectable with a reduced amount of fixative.

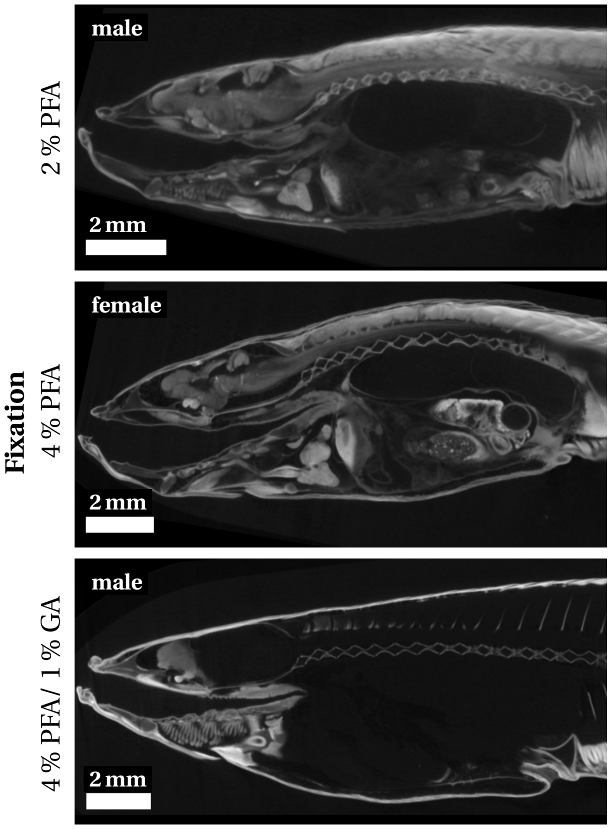

Figure 4.2.: Sagittal slices of 17 months old medaka. The medaka were fixed with 2 % PFA, 4 % PFA, or 4 % PFA/ 1 % GA. The staining depth decreases with stronger fixation. The grey values display the reconstructed linear attenuation coefficient from 0 cm^{-1} to 0.64 cm^{-1} (black to white).

Table 4.3.: Staining quality of brain (B), liver (L) and tail muscle (TM) based on the histogram analysis of 17 months old medaka. The medaka were fixed with 2 % PFA, 4 % PFA, or 4 % PFA/ 1 % GA and stained according to the given protocol (table 4.1). Green ticks mark a complete staining. Orange ticks mark partial staining. Red crosses mark an insufficient staining. The percentages indicate the proportion of voxels with a grey value below twice the mean background for the analysed region. The staining quality decreases with stronger fixation.

Fixation		B	L	TM
	2 % PFA	✓ 0.00 %	✓ 0.00 %	✓ 0.01 %
	4 % PFA	✓ 0.00 %	✓ 0.02 %	(✓) 11.95 %
	4 % PFA/ 1 % GA	(✓) 68.70 %	✗ 98.25 %	✗ 89.13 %

4.1.4. Influence of staining temperature and dehydration agent on staining efficiency

This experimental series investigated the influence of the ambient air temperature and the dehydration agent on staining efficiency. It compares the dehydration agents ethanol and acetone as well as the staining temperature.

Samples and effective pixel size

The five samples were 17 months old medaka of the inbred line 2-3 (O-GFP). Table 4.4 summarizes the protocol variations. Acetone and ethanol were tested as dehydration agent and used as solvent for PTA. The temperature during dehydration and staining was 22 °C, 37 °C or 60 °C. A staining with acetone at 60 °C is impossible, as the boiling point of acetone is at 56 °C. All other parameters and steps of the sample preparation remained as stated in the basic staining protocol (table 4.1).

The sample placement resulted in an effective pixel size of 17.3 µm.

Table 4.4.: Staining variations.

Sample	Dehydration agent	PTA solvent	Temperature /°C
201804_0008	acetone	acetone	21
201804_0012	acetone	acetone	37
201804_0002	ethanol	ethanol	21
201804_0010	ethanol	ethanol	37
201804_0016	ethanol	ethanol	60

Results

Table 4.5 summarizes the results of the histogram analysis. The staining efficiency increased with a higher temperature. In the medaka dehydrated and stained with acetone as well as in the medaka dehydrated and stained with ethanol, the medaka with the highest temperature achieved the best staining. However, the medaka dehydrated and stained with ethanol at 60 °C remained partially stained in brain and tail muscle. The replacement of ethanol by acetone improved the staining efficiency even more than the temperature increase. At 22 °C ambient air temperature, the replacement of the dehydration agent lead from an unstained medaka to an almost completely stained medaka. Only the tail muscle remained partially stained. The unstained fraction of each organ dropped significantly: in the brain from 68.72 % to 0.85 %, in the liver from 98.30 % to 1.54 % and in the tail muscle from 89.4 % to 5.56 %. At 37 °C, the medaka dehydrated with acetone was completely stained. The unstained fraction was 0 % for brain and liver and 0.01 % for the tail muscle. The medaka dehydrated with ethanol remained partially stained in the brain and unstained in liver and tail muscle. The unstained fraction was 37.12 % for brain, 86.48 % for the liver, and 86.43 % for the tail muscle. In comparison to 22 °C, the unstained fraction of each organs decreased.

Table 4.5.: Staining quality of brain (B), liver (L) and tail muscle (TM) based on the histogram analysis of 17 months old medaka. The medaka were dehydrated and stained with either acetone or ethanol at 22 °C or 37 °C. In addition, staining with ethanol at 60 °C was evaluated. Green ticks mark a complete staining. Orange ticks mark partial staining. Red crosses mark an insufficient staining. The percentages indicate the proportion of voxels with a grey value below twice the mean background for the analysed region. The use of acetone significantly increases the staining quality. A higher temperature slightly increases the staining quality.

		Dehydration agent					
		Acetone			Ethanol		
Temperature	22 °C	B ✓ 0.63 %	L ✓ 1.53 %	TM (✓) 5.08 %	B (✓) 68.70 %	L ✗ 98.25 %	TM ✗ 89.13 %
	37 °C	B ✓ 0.00 %	L ✓ 0.00 %	TM ✓ 0.01 %	B (✓) 37.12 %	L ✗ 86.48 %	TM ✗ 86.43 %
	60 °C	Boiling point at 56 °C.			B (✓) 10.31 %	L ✓ 0.00 %	TM (✓) 47.91 %

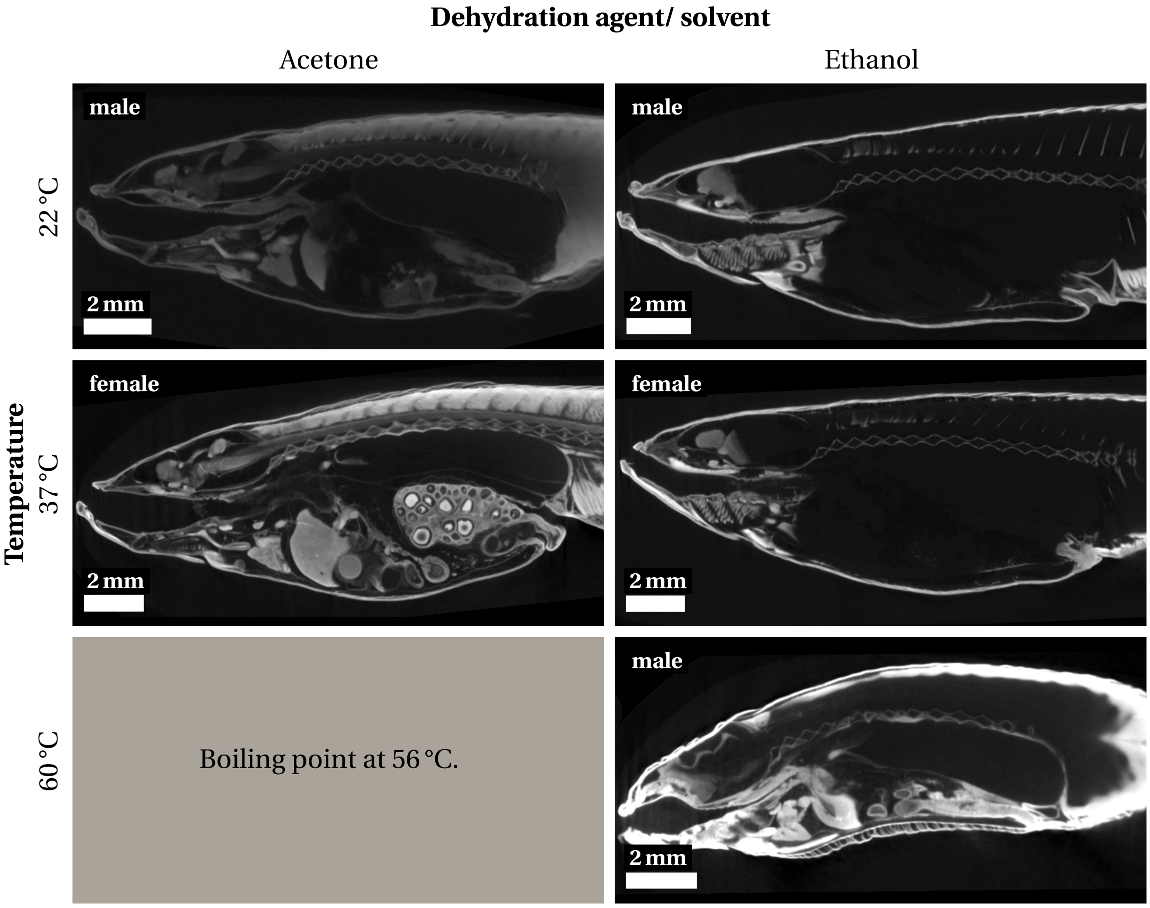

Figure 4.3.: Sagittal slices through the tomograms of 17 months old medaka. The medaka were dehydrated and stained either with acetone or ethanol at 22 °C or 37 °C. Staining with ethanol at 60 °C was additionally evaluated. The use of acetone significantly increases the staining depth. A temperature increase slightly increases staining depth and contrast in stained regions, The grey values display the reconstructed linear attenuation coefficient from 0 cm^{-1} to 0.64 cm^{-1} (black to white).

A visual evaluation of the tomograms confirmed the results of the histogram analysis as seen exemplary in the sagittal slices (figure 4.3). The medaka dehydrated with ethanol at 21 °C and 37 °C were stained only in regions near the body surface as the mouth or the skin. At 60 °C, the staining penetrated the abdomen. However, the dorsal muscle remained unstained. The shrinkage cannot be evaluated due to the insufficient staining. The medaka dehydrated with acetone at 37 °C was completely stained. However, the brain shrunk as it did not fill the cranial cavity. In the medaka dehydrated with acetone at 22 °C, a gradient remained in the tail muscle and the overall contrast was lower. It showed no shrinkage.

Conclusion

The experimental series showed that a replacement of ethanol by acetone as dehydration agent and PTA solvent is a promising way to improve the staining efficiency. Solely this exchange led from an insufficient staining to an almost complete staining at 22 °C and to a complete staining at

37 °C. In particular, the fixation remained 4 % PFA/ 1 % GA. Therefore, the replacement of ethanol by acetone has a greater influence regarding staining efficiency than a reduction of the fixative. Likewise, the effect of the replacement on staining efficiency is larger than that of a temperature increase. The excellent contrast of the medaka dehydrated with acetone at 37 °C allowed tissue differentiation even between different brain regions. However, this medaka showed shrinkage of the brain. The increased temperature might lead to a faster dehydration, which induces the shrinkage. To avoid the shrinkage, the dehydration steps could be adapted, or the temperature lowered during the dehydration step. The evaluation of the shrinkage was not possible for the ethanol-based samples due to insufficient staining of inner organs.

4.1.5. Influence of staining duration and PTA concentration on staining efficiency

This experimental series adapted the staining protocol to 13 weeks old medaka, which are of similar size than the 10 weeks old medaka planned for later studies. The influence of different PTA concentrations and staining durations on the staining efficiency was tested. To minimize the total time needed for the staining, PTA is added to the dehydration agent in the according concentration.

Samples and effective pixel size

Six 13 weeks old medaka of the inbred line Ho5 were sacrificed and stained with varying PTA concentrations and staining durations. Table 4.6 states the differences of each sample in comparison to the basic staining protocol (table 4.1). The use of acetone as dehydration agent implies the usage of acetone also as PTA solvent. Two medaka were stained with 0.075 % PTA, two others with 0.15 % PTA and the last two with 0.33 % PTA. The staining duration was 24 h for one medaka of each of these pairs and 48 h for the other. They were stained at 37 °C. The dehydration agent and PTA solvent were acetone. Fixation, washing steps and embedding remained as presented in table 4.1.

Table 4.6.: Staining variations. The PTA concentration in dehydration agent and staining is the same.

Sample	Dehydration agent	PTA concentration /%	Staining duration /h
201810_0081	acetone + PTA	0.33	24
201810_0082	acetone + PTA	0.33	24
201810_0083	acetone + PTA	0.15	24
201810_0084	acetone + PTA	0.15	48
201810_0085	acetone + PTA	0.075	24
201810_0086	acetone + PTA	0.075	48

The sample position resulted in an effective pixel size of 10.9 µm. The CT scan of the medaka stained with 0.33 % PTA ranges only over 299° as the x-ray tube broke down.

Results

Resulting from the histogram analysis (table 4.7), all medaka were completely stained. The medaka stained with 0.075 % PTA were the only ones to have a small, unstained fraction of voxels. In the medaka stained for 24 h, 0.3 % of the tail muscle remained unstained. In the medaka stained for 48 h, 0.09 % of the brain remained unstained.

Table 4.7.: Staining quality of brain (B), liver (L) and tail muscle (TM) based on the histogram analysis of 13 weeks old medaka. The medaka were stained with 0.075 % PTA, 0.15 %, or 0.33 % PTA for either 24 h or 48 h. All samples were completely stained. The percentages indicate the proportion of voxels with a grey value below twice the mean background for the analysed region. It lowers with increasing staining time or higher PTA concentration.

		Staining duration					
		24 h			48 h		
PTA concentration	0.075 %	B ✓ 0.00 %	L ✓ 0.00 %	TM ✓ 0.30 %	B ✓ 0.09 %	L ✓ 0.00 %	TM ✓ 0.00 %
	0.15 %	B ✓ 0.00 %	L ✓ 0.00 %	TM ✓ 0.00 %	B ✓ 0.00 %	L ✓ 0.00 %	TM ✓ 0.00 %
	0.33 %	B ✓ 0.00 %	L ✓ 0.00 %	TM ✓ 0.00 %	B ✓ 0.00 %	L ✓ 0.00 %	TM ✓ 0.00 %

The visual impression of the tomograms confirmed the results of the histogram analysis. Sagittal slices (figure 4.4) of the tomograms show that the contrast increased with staining duration and PTA concentration. The medaka stained with 0.33 % PTA for 48 h is blurred due to an under-sampled CT scan (see section 2.5.3). Staining for 24 h with 0.33 % resulted in a bright contrast in some organs and the upper back muscle in comparison the rest of the medaka. None of the medaka showed shrinkage.

Conclusion

The experimental series showed an improved staining with higher PTA concentrations as well as longer staining durations. A staining with 0.15 % PTA for 24 h was sufficient for a complete full body staining of a 13 weeks old medaka. The partially strong staining with 0.33 % PTA for 24 h might lead to beam hardening artefacts at the beam line. No shrinkage was detected.

4.1.6. Revised staining protocol

The variations on the staining protocol showed that the replacement of ethanol by acetone has the largest effect on the staining efficiency. This single change allowed a satisfying full body staining of 13 weeks and 17 months old medaka of different inbred lines. However, the 17 months old medaka dehydrated at 37 °C medaka showed shrinkage, which is a known issue in staining of biological samples. An adaption of the dehydration series or a lower temperature might overcome this issue. In general, acetone-based staining reduces the risk of shrinkage due to a shorter staining duration. Options as using water-solved PTA or sample rehydration to avoid shrinkage were not considered. Both affect sample storage, which is important to prepare medaka in advance. The 13 weeks old medaka required a lower PTA concentration and a shorter staining duration for optimum staining in comparison to the larger, 17 months old medaka.

Table 4.8 presents the revised staining protocol for 10 weeks old medaka.

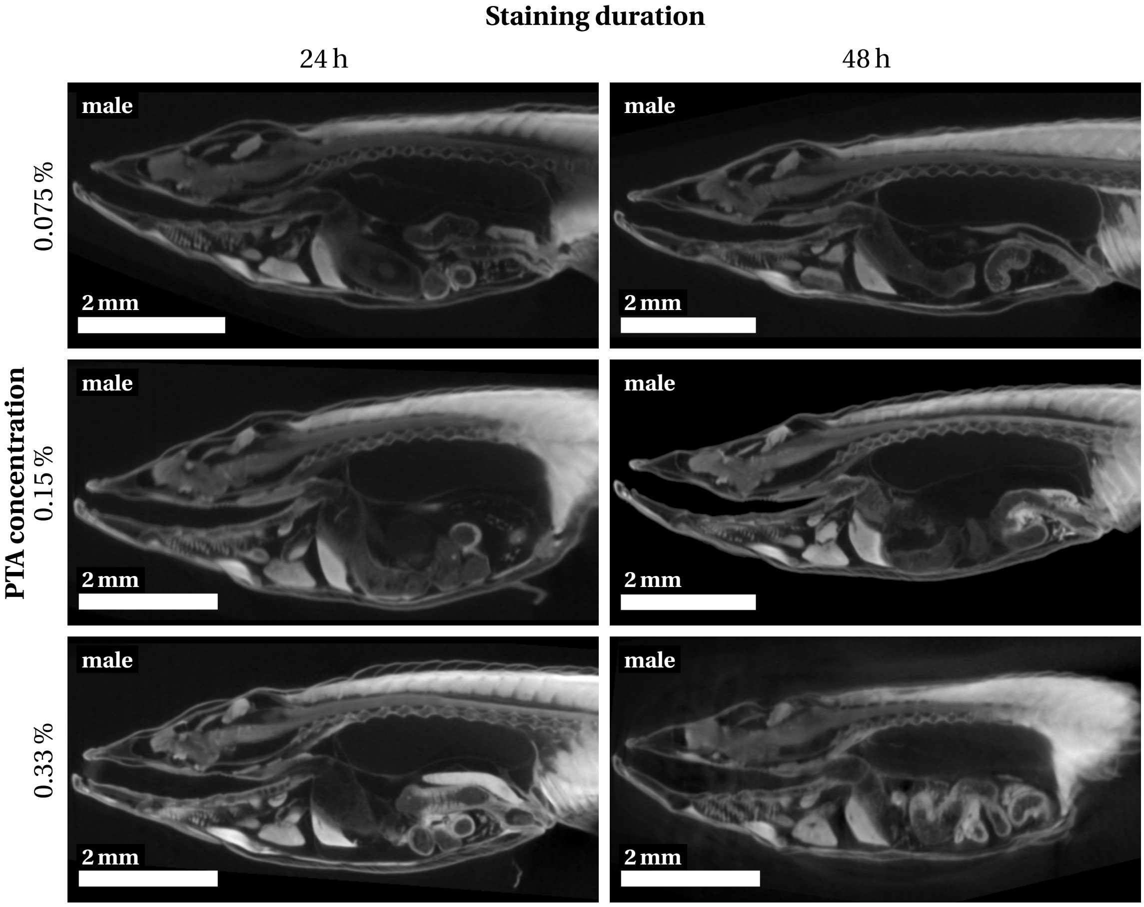

Figure 4.4.: Sagittal slices through the tomograms of 13 weeks old medaka. The medaka were stained with 0.075 % PTA, 0.15 %, or 0.33 % PTA for either 24 h or 48 h. All medaka were completely stained. The contrast increased with a longer staining duration as well as with a higher PTA concentration. The grey values display the reconstructed linear attenuation coefficient from 0 cm^{-1} to 0.81 cm^{-1} (black to white).

Table 4.8.: Revised staining protocol for a full-body staining of 10 weeks old medaka at 37 °C. Chemicals are exchanged every 48 h. The abbreviations are listed in table A.1.

Step	Agent	Duration
Fixation	4 % PFA/ 1 % GA	3 days
Washing	PBS	3×10 min
Dehydration	10 %, 25 %, 50 %, and 70 % acetone + 0.15 % PTA	45 min each step
Staining	0.15 % PTA in 70 % acetone	48 h
Washing	acetone	2×30 min

4.2. Optimization of embedding

In the previous μCT measurements at the synchrotron, bubbles formed in the embedding material agarose during the scanning (see section 3.1.2). The bubble formation caused motion artefacts in the reconstructed data and locally reduced the resolution. Resulting data sets will not be usable for further analysis. The aim of this section is to find an embedding material that is stable under x-ray exposure and prevents sample movement during the CT scan. Therefore, any liquid embedding material is not suitable as medaka float. The following four common embedding materials were selected for further testing, as they were stable during 1 min x-ray exposure in filtered white beam:

- gelatine,
- low melting agarose (LMA),
- paraffin,
- polyacrylamide.

4.2.1. Samples

Four medaka older than one year were stained according to the revised staining protocol (table 4.8). Each medaka was embedded in a 2 ml Eppendorf tube using one of the following embedding materials: gelatine, LMA, paraffin, and polyacrylamide. The sample preparation was performed at the IBCS by Narendar Aadepu.

4.2.2. Imaging setup

The medaka were scanned at the UFO station at KIT synchrotron (section 2.6.1). The x-ray beam was filtered with 0.2 mm aluminium. The Optique Peter macroscope was mounted with 2x magnification and coupled with the PCO.dimax. The resulting effective pixel size is 6.2 μm. One tomographic scan consisted of 3000 equiangular projections over a 180° rotation. The exposure time was 14 ms. This resulted in 2.5 min image acquisition per tomographic scan. Five to six tomograms covered the entire length of a medaka.

4.2.3. Results

The visual analysis shows large quality differences of the tomographic volumes resulting from the embedding with different embedding materials (figure 4.5).

The medaka embedded in gelatine was deformed (figure 4.5a) and the complete body collapsed (A3, blue arrows). From the eye, only the lenses remained intact. Compared to the other tomographic volumes of medaka, the oral cavity was closed (blue arrow, A1). The outer part of the medaka is blurred.

The medaka embedded in LMA shows neither deformations nor motion artefacts. All organs were clearly visible (figure 4.5b). In the sagittal slice, low contrast beam hardening artefacts appeared as “shadow medaka” (B1).

The medaka embedded in paraffin shows neither deformations nor motion artefacts (figure 4.5c). All organs were clearly visible. However, the paraffin did not enclose the medaka completely. It did not penetrate the mouth (C1) and detached from the skin.

The medaka embedded in polyacrylamide shows no deformations or movement artefacts (figure 4.5d). All organs were clearly visible, but high absorbing spots were visible (D1).

(a) Gelatine.

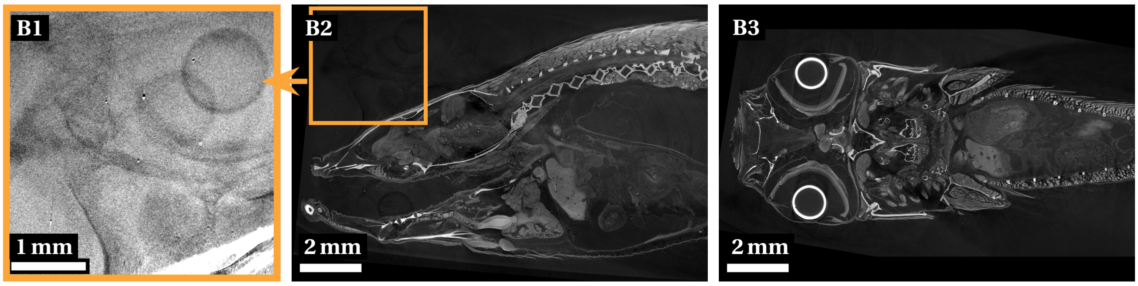

(b) Low melting agarose.

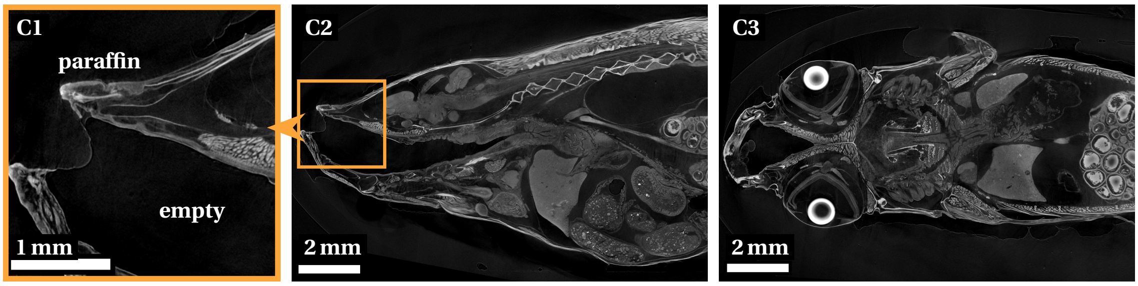

(c) Paraffin.

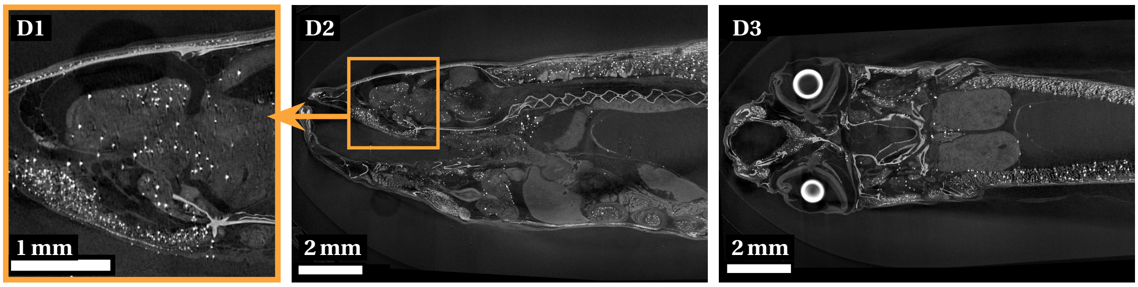

(d) Polyacrylamide.

Figure 4.5.: (Columns 1 and 2) Sagittal and (column 3) coronal slices of medaka embedded in (a) gelatine, (b) low melting agarose, (c) paraffin, and (d) polyacrylamide. All medaka are stained with the protocol developed in the previous section. (B1 to B3) Low melting agarose (LMA) performed best. It did not alter the sample, completely enclosed it, and (B1) beam hardening artefacts indicate a low absorption in LMA. The slices display the reconstructed linear attenuation coefficients from 0 cm^{-1} to 7.23 cm^{-1} (black to white). The detailed views (A1, C1, D1) display them from 0 cm^{-1} to 4.27 cm^{-1} and the detailed view (B1) displays them from 0 cm^{-1} to 1.14 cm^{-1}.

4.2.4. Conclusion

From all embedding materials tested, low melting agarose (LMA) and paraffin were the only ones to not alter the sample. Gelatine dehydrated the sample leading to shrinkage and motion blur during the scan. Polyacrylamide led to high-absorbing precipitates, probably caused by a reaction of polyacrylamide with PTA. Paraffin did not enclose the sample completely. It did not penetrate the open mouth and detached from the skin. Therefore, LMA is the embedding material of choice although the tomographic reconstruction led to beam hardening artefacts at high absorbing structures as lenses and skin. Additional filters for the low energy x-ray regime will reduce the beam-hardening artefacts.

4.3. Optimization of image quality and reduction of post-processing time

Step CT configuration is commonly used in tomographic scans of samples larger than the available field of view. The resulting tomographic volumes are afterwards stitched together to receive a full body volume. Another configuration is helical CT (section 2.5), which is especially suited for the measurement of long, extended objects as medaka. The result of the reconstruction is one tomographic volume without the need for further processing. Additionally, helical CT reduces ring artefacts [47].

In this section, step and helical CT are compared regarding acquisition and post-processing time as well as image quality and resolution.

4.3.1. Sample preparation

Five four weeks old medaka (samples M1 to M5) from the inbred line Ho5 were sacrificed and stained according to the revised protocol (see table 4.8). All samples were embedded in Eppendorf tubes using LMA. The samples were prepared at the IBCS by Narendar Aadepu.

4.3.2. Imaging setup

The tomographic scans were carried out at the UFO station of KIT Light Source (see section 2.6.1). The x-ray beam was filtered using 1 mm aluminium. The Optique Peter twin mic was used with 5x magnification. The effective pixel size is 2.44 µm and the square field of view has a width of 4.92 mm. The exposure time per projection was 8 ms with a frame rate of 70 fps to not overflow the internal camera memory during a helical CT scan.

Step and helical CT consisted of 1500 projections per 180° rotation. Four CT scans covered the 15 mm long samples in step CT configuration. The vertical shift between the tomograms was 3.5 mm. In helical CT, a 180° turn covered about 3 mm sample length. Scanning the whole sample equalled to six step CT tomograms. The vertical travel speed was adapted to the frame rate. Each sample was scanned in step and helical configuration. The samples were exchanged manually.

After reconstruction and stitching of the spiral CT scans (see section 2.6.3), the step CT and helical CT tomograms were automatically aligned using Amira 2019.2.

4.3.3. Results

The comparison of helical and step CT is divided into two main aspects: the time needed per sample for scanning and post-processing and the analysis of the respective tomograms regarding image quality and resolution.

In step CT, the total time for the CT scan and tomographic reconstruction was about 71 min (table 4.9). Helical CT configuration was faster. In total, it only needed 51 min. The main time reduction in helical CT was the avoidance of stitching, which is needed in step CT scan to obtain a single tomogram of the complete medaka. However, a helical CT scan was roughly 4 min longer than the complete step CT scan, as the camera read-out was significantly longer. The read-out lasted an additional 389.19 s in helical and 65.52 s in step CT configuration after the image acquisition finished. The reconstruction of the tomograms took about 41 min for helical CT and around 35 min for four step CT volumes. Some reconstructions in step CT required manual assistance to find the position of the axis of rotation resulting in a longer time needed.

Table 4.9.: Mean scanning and post-processing times for step and helical CT scans resulting from the measurements of five 15 mm long medaka at the UFO station.

	Time helical CT /s	Time step CT /s
Total CT scan	568.17±10.92	323.56±19.35
- acquisition	181.49±5.35	258.26±18.01
- read-out	389.19±4.90	65.52±2.36
Reconstruction	2483.56±283.56	2061.40±301.55
Stitching	–	1883.03±94.24
Total	3054.24±292.07	4268.21±697.35

A detailed look into the gills (figure 4.6) shows, that the resulting resolution was similar in the tomograms acquired using helical CT or step CT. The contrast was higher in the helical CT tomogram, but the display of the medaka was slightly blurred. At the gills, the background noise was increased in helical CT in comparison to step CT.

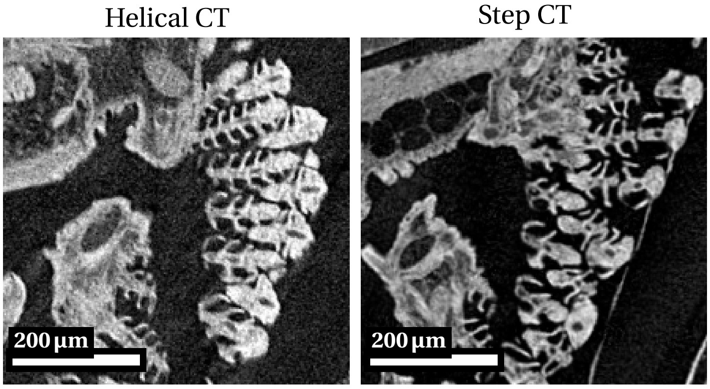

Figure 4.6.: Axial slice displaying the gills of a four weeks old medaka (sample M3). The tomograms resulted from (left) helical and (right) step CT configuration. The resolution is similar. The grey values range from 0 cm^{-1} to 5.68 cm^{-1} (black to white).

In general, the reconstructed contrast was higher in the helical CT tomograms throughout the complete medaka (figure 4.7). The display of the air bladder was less noisy in helical CT. All relevant organs and tissues, including different brain regions and retinal layers, were distinguishable and could be segmented in both configurations. The collapsed left eyeball (figure 4.7, orange arrows) resulted from the sample preparation.

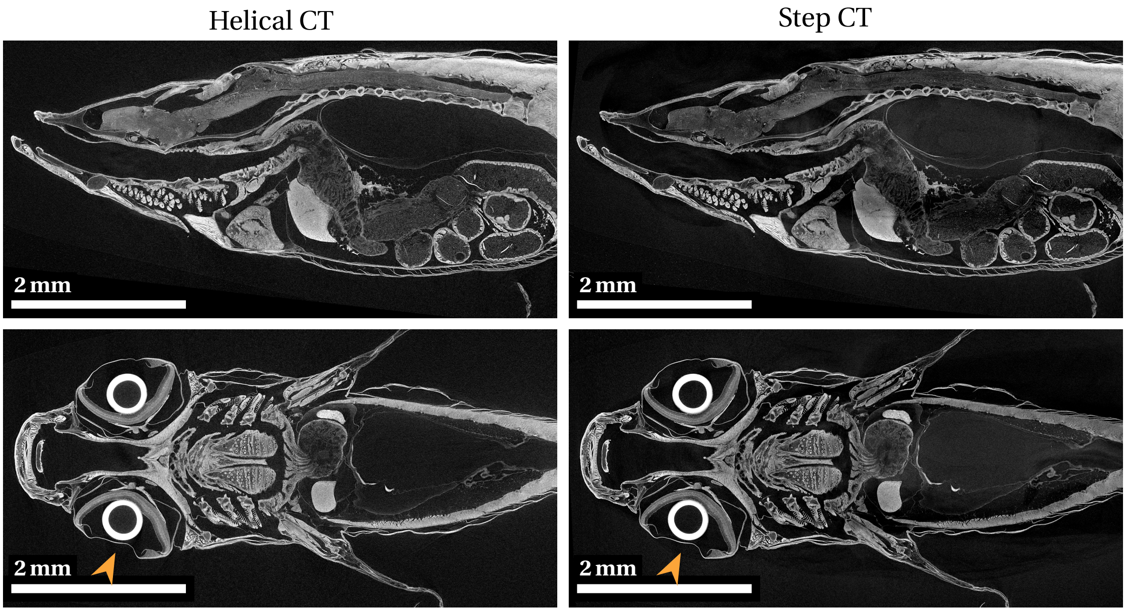

Figure 4.7.: (top) Sagittal and (bottom) coronal slices of the tomograms of a four weeks old medaka (sample M3) scanned and reconstructed using (left) helical and (right) step CT configuration. The contrast, especially in the intestine, is higher in the helical CT configuration. The left eyeball collapsed (orange arrow). The grey values range from 0 cm^{-1} to 5.68 cm^{-1} (black to white).

Despite a ring filter, ring artefacts remained prominent in step CT data for example in the liver (figure 4.8). The ring filter reduced the ring artefacts, but unwanted contrast differences remained. It also blurred the ring artefacts leading to a blur in underlying image information. Therefore, the level of detail available is higher in helical CT in affected regions as the intestine.

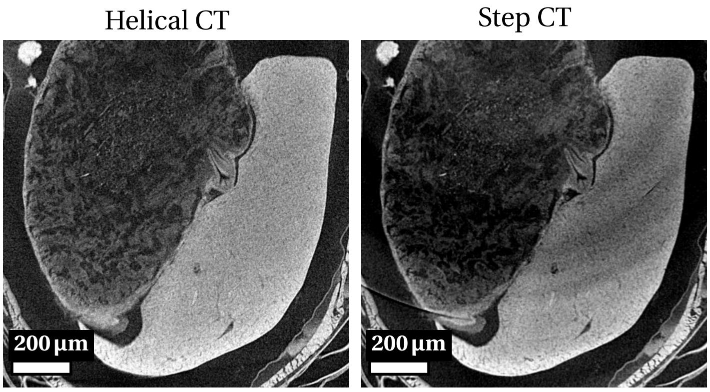

Figure 4.8.: Axial slice displaying liver and intestine of a four weeks old medaka (sample M3). The tomograms resulted from (left) helical and (right) step CT configuration. Helical CT suppresses ring artefacts. The grey values range from 0 cm^{-1} to 5.68 cm^{-1} (black to white).

The calculated CNRs (figure 4.9, left) confirmed a higher image quality of the helical CT tomograms. Only the liver of sample M4 and the tail muscle of sample M2 had a similar CNR in helical and step CT data. The smaller CNR of the step CT data resulted from a trend towards lower contrast in the examined regions as indicated by the distributions of linear attenuation coefficients in the examined regions (figure 4.9, right). The distributions of the linear attenuation coefficients in the background were similar for helical and step CT data. Further analysis showed that the background noise in step CT depended on the position of the examined region on the detector. The noise was higher, if the organ's position was at the top or the bottom of the detector.

4.3.4. Conclusion

The most important aspects for fast full-body CT imaging of medaka are the time needed of CT scan and post-processing as well as the image quality.

Step CT was about 4 min faster than a helical CT scan. However, helical CT was 20 min faster in post-processing as the reconstruction directly returns the complete tomographic volume. The stitching needed in step CT added about 30 min to achieve a complete tomogram of a medaka. In total, helical CT was faster with the bottleneck being the up-to-date camera read-out.

Helical CT resulted in a higher CNR and generally in a tendency towards higher contrast in the examined organs. As stated by Pelt et al. [47], the use of helical CT eliminates ring artefacts. In general, the image quality was higher in helical CT. In step CT, the noise was highest at the top and bottom of the detector, as here the photon count is lower. A smaller vertical step between the CT scans would decrease the noise at the cost of a longer acquisition and post-processing time due to the additional CT scans needed to cover the entire sample.

The displayed structures are slightly blurred in helical CT data in comparison to step CT. Still, the resolution is high enough to display the fine structures of the gills in both configurations.

To conclude, helical CT is favourable for high-throughput imaging with this imaging setup. The total processing time per medaka is shorter and the resulting image quality was higher.

4.4. Conclusion

In this chapter, different optimizations of the staining, the embedding, and the imaging setup for high-throughput full-body 3D imaging of medaka were tested.

The phosphotungstic acid (PTA) staining was optimized by replacing ethanol with acetone as dehydration agent and PTA solvent. This measure results in a high staining efficiency regarding reliability and homogeneity. The adapted protocol was successfully tested on 5 weeks, 13 weeks, and 17 months old medaka of different sizes and inbred lines. Thus, the acetone-based staining overcomes previously reported size limitations for ethanol-based PTA staining [67–70]. Distinction and segmentation of all relevant inner organs was possible. The low resolution of the laboratory setup limited the distinction of small structures.

Low melting agarose (LMA) resulted as the best choice of the tested embedding materials for measurements using a synchrotron pink beam. It formed no bubbles neither during 1 min exposure nor during a complete CT scan of a medaka. In addition, it completely enclosed the medaka without any alteration regarding shape or contrast.

The aim for the imaging pipeline is an imaging setup that provides a high image quality in combination with a low time effort. A comparison demonstrated that helical CT is advantageous

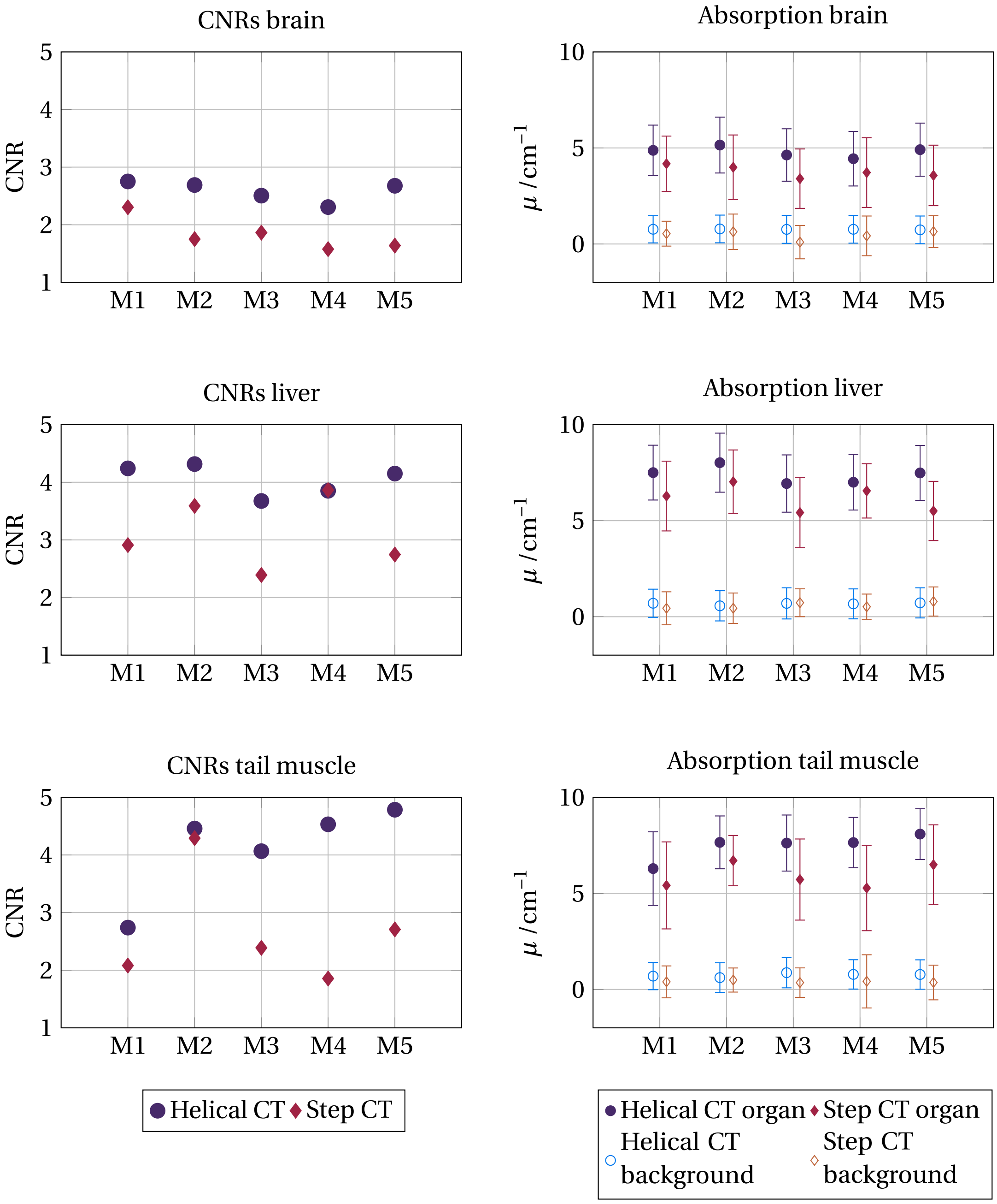

Figure 4.9.: (left) Comparison of the CNRs of the segmented brains, livers, and parts of the tail muscle of five four weeks old medaka (samples M1 to M5) scanned and reconstructed using helical CT or step CT configuration. (right) Boxplots of the linear attenuation coefficients of the voxels inside the segmented regions as well as of the background for all five medaka and the two CT configurations. The CNRs resulting from the helical CT scans were higher than that obtained by the step CT scan. The reconstructed linear attenuation coefficients in the segmented regions tend to be higher for helical CT configuration. The linear attenuation coefficients in the backgrounds were similar in both configurations.

to step CT in both aspects. The image quality was higher due to suppressed ring artefacts at the cost of a 4 min longer acquisition time for the CT scan. Further reduction of the acquisition time in helical CT scan is presently limited by the up-to-date camera read-out. Future improvements in camera technology and data transfer might speed up the camera read-out and thus the helical CT scan. The post-processing was significantly faster in helical CT compared to step CT.

To conclude, the sample preparation and imaging setup for absorption imaging were successfully optimized. The optimized workflow can be implemented in the pipeline of high-throughput full-body imaging of medaka.

Chapter 5

High-throughput imaging pipeline for full-body imaging of medaka

This chapter presents the imaging pipeline from sample preparation and high-throughput measurements to tomographic reconstruction for 10 weeks old medaka as derived in the previous chapters. It evaluates the throughput as well as the image quality and resolution of resulting tomograms. A manual segmentation shows the level of detail available for morphometric analysis.

5.1. Established imaging pipeline

The aim of this thesis is the development of an imaging pipeline. In the previous chapters, different tasks of the workflow were optimized regarding sample throughput, image quality, resolution, and time effort for the imaging of adult medaka. In addition to the presented results, smart parallelization of axis movement and data-read-out reduced the time span between two consecutive helical CT scans. The following sections present the optimized steps of the final imaging pipeline (figure 5.1) in detail. Highlighted are the tasks that were adapted in this thesis to optimize the performance of the imaging pipeline.

5.1.1. Sample preparation

The sample preparation ensures the comparability of the samples, sufficient contrast of all inner organs and tissues, and a standardized sample form for high-throughput measurements.

The medaka are raised under controlled conditions such as a fixed day/ night cycle and constant water temperature to ensure similar growth (see appendix A.1). They are sacrificed about 10 weeks post hatching after reaching adulthood. Table 5.1 presents the preparation of the medaka for absorption µCT . The medaka are stained in batches of five per flask to reduce the effort, while providing sufficient chemicals to each medaka for fixation and staining. To stain larger, older medaka, a higher PTA concentration and longer fixation and staining times are required to ensure sufficient contrast (see section 4.1).

After the staining, each medaka is embedded into 0.5 ml Eppendorf tubes using low melting agarose. Stained and embedded samples could be stored at 4 °C for at least half a year without degeneration.

5.1.2. Data acquisition

The imaging setup for data acquisition is located at the UFO station of KIT Light Source for which systematic access is granted. The beamline parameters are listed in section 2.6.1. The x-ray beam is filtered with aluminium to reduce the heat load on the sample and to avoid beam hardening.

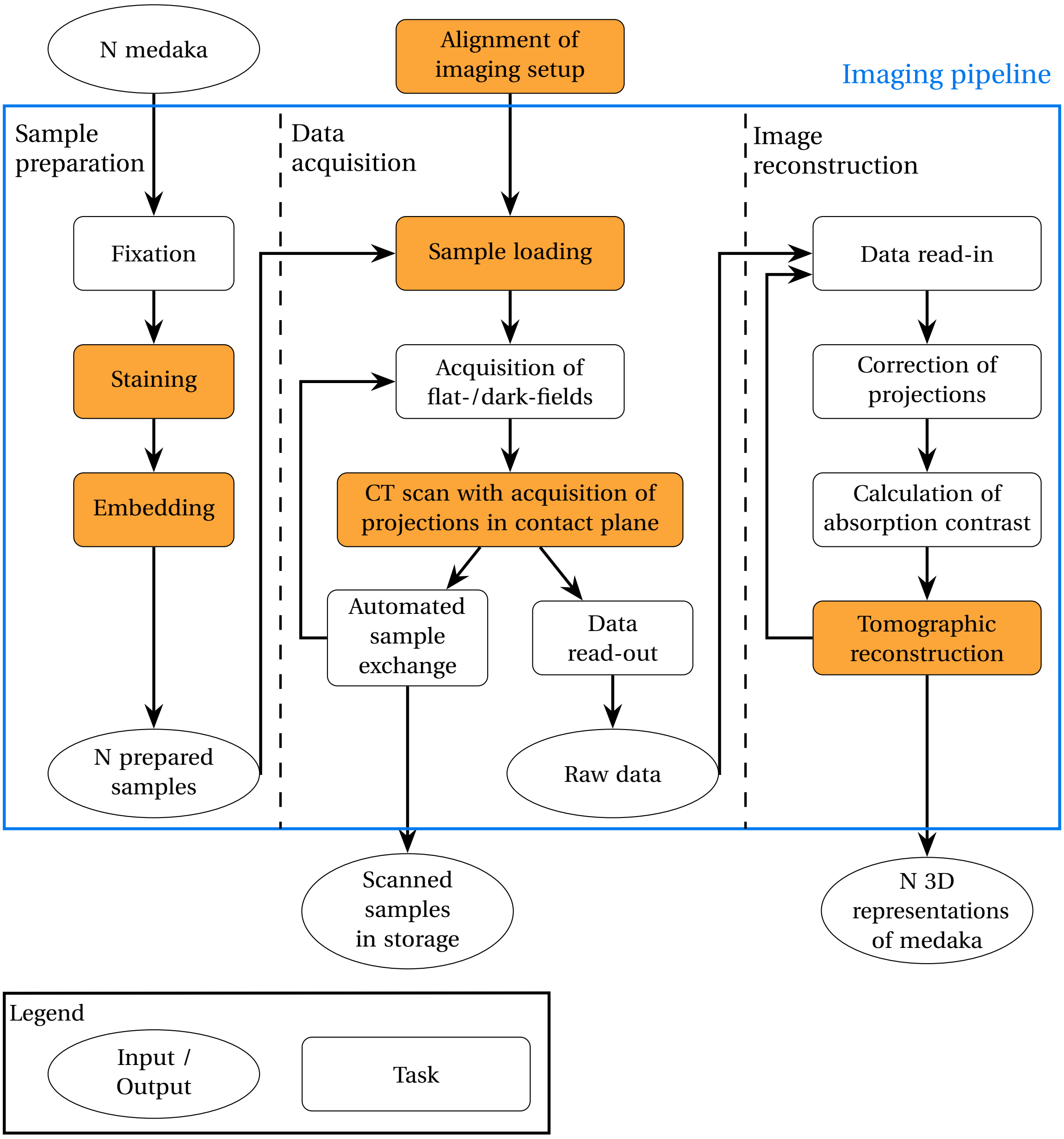

Figure 5.1.: Workflow of the resulting imaging pipeline for high-throughput imaging of adult medaka. The automated segmentation handles up to 40 samples without human intervention. Highlighted are the tasks that were adapted and optimized in the framework of this thesis.

The thickness of the filters is adapted to the flux density, which depends on the ring current. The filter thickness is 1 mm for a ring current above 120 mA and 0.7 mm below 120 mA.

Figure 5.2a shows the final tomographic station. The camera is the Elya macroscope with 2.5× magnification (section 2.6.1). The horizontal field of view (FOV) of 8.87 mm matches the inner diameter of 8.8 mm of the standardized polypropylene containers [62]. The vertical FOV is cropped to 1536 pixel to avoid the low intensity regions at top and bottom of the FOV. In addition, it reduces data size. The effective pixel size is 4.4 µm. The exposure time per projection is 40 ms

Table 5.1.: Staining protocol for a full-body staining of 10 weeks old medaka. The temperature during the staining is 37 °C. The abbreviations are listed in table A.1.

Step	Agent	Duration
Fixation	4 % PFA/ 1 % GA	3 days
Washing	PBS	3×10 min
Dehydration	10 %, 25 %, 50 %, and 70 % acetone + 0.15 % PTA	45 min each step
Staining	0.15 % PTA in 70 % acetone	48 h
Washing	PBS	2×30 min

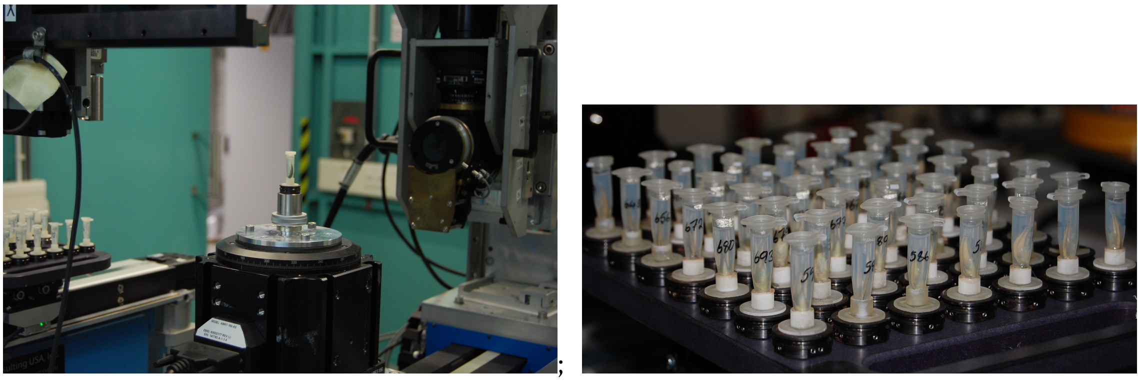

(a) Tomographic station.

(b) Prepared sample tray.

Figure 5.2.: (a) Tomographic station used in the imaging pipeline with sample changer robot (left), rotary stage (mid), and Elya detector system (right). (b) Prepared sample tray with 49 medaka.

with the according frame rate of 25 fps. This corresponds to the upper limit for the frame rate to avoid overflow of the camera memory.

The tomographic volumes are acquired in helical CT configuration. The scan takes 2000 projections per 180 °C and covers a vertical travel of 1336 pixels (≈ 5.88 mm) during that rotation. The total vertical travel is 28 mm per medaka, which roughly corresponds to five 180°-CT scans. Data acquisition without online-reconstruction, sample exchange, and camera read-out accumulate to a processing time of 11 min per sample. A single helical CT scan of a 10 weeks old medaka produces 67.8 GB of data.

The use of the sample changer robot allows to scan a sample tray containing up to 49 samples (figure 5.2b) without human intervention. The sample trays are exchanged manually. A single alignment procedure at the beginning of each beam time and the standardized sample size ensure that each sample is inside the FOV.

5.1.3. Image reconstruction

The automated helical CT reconstruction runs within the UFO framework [55]. It bases on filtered backprojection which allows online reconstruction during image acquisition adding 3 min to the duration of the helical CT scan. A tomogram has 94.6 GB data size, so the scanning of a 10 weeks old medaka results in 162.4 GB of data.

5.2. Evaluation of the imaging pipeline

This section presents the evaluation of the sample throughput and addresses the question of consistent imaging quality of the tomograms. Additionally, the semi-automated segmentation of a medaka shows which organs and tissues can be segmented for later analysis.

5.2.1. Sample throughput

The time efforts for sample preparation, image acquisition, and reconstruction have been minimized as much as possible while providing sufficient image quality in the tomograms.

The sample preparation takes about 6 days. This time is needed to ensure sufficient fixation and staining for 10 weeks old medaka. Storage of prepared medaka is possible at least for half a year without detectable degeneration. Therefore, the relatively long sample preparation is no limitation for large-scale measurements of medaka.

A short duration of the helical CT scan is of great relevance as the available beam time at a synchrotron is limited. For 10 weeks old medaka, the duration was reduced to 11 min. The limitation is the speed of the up-to-date camera read-out. The sample changer robot reduces manual work and allows to scan up to 49 samples without human intervention. The scanning of a full sample tray with 49 samples takes roughly 9 h. Then the sample tray is manually exchanged, and the automated CT scans restarted. The high-throughput helical CT allows to scan up to 110 medaka per day corresponding to 22 h of available x-ray beam.

The automated tomographic reconstruction takes about 30 min per medaka on two RTX 8000 graphic cards (NVIDIA). Thus, the reconstruction of 110 medaka measured in a day takes about 55 h. The total amount of measured and reconstructed data for 110 medaka accumulates to 17.5 TB.

To conclude, the imaging pipeline is suited for large-scale studies. Up to 500 tomographic volumes of 10 weeks old medaka can be acquired within a week of beam time corresponding to 100 h of available x-ray beam.

5.2.2. Comparability of tomograms

Similar and reproducible image quality and resolution between different scans allow for comparative studies and ease automated segmentation of the tomograms. Thereby, image quality comprises contrast and noise.

Image quality

The resulting contrast of the different tissues depends mostly on the staining. The staining protocol is identical for all samples. Visual evaluation shows sufficient staining of relevant organs and tissues in all 884 medaka scanned up to now. No shrinkage was detected. The noise and contrast in tomograms depend on the signal-to-noise ratio (SNR) of the acquired projections. A high SNR is desirable, which corresponds to a high signal and thus a high current at the synchrotron.

The contrast-to-noise-ratio (CNR) is a measure for the image quality regarding contrast and noise. Therefore, the CNRs of eye lenses, retinae and liver were calculated from 161 tomograms for further analysis. The tomograms were acquired using the developed image pipeline. The medaka are from 29 different inbred lines with a varying number of individuals per inbred line. Prior to the segmentation, the tomograms were binned by a factor of two and individually transformed to 8-bit data to reduce data size. This affects the values of contrast and noise, but the CNR remains unchanged in a reasonable transformation range from 32-bit to 8-bit image data. The data was provided by Yaroslav Zahrov (IPS, KIT), who develops neural networks for automated segmentation of medaka. As each medaka has two eyes, the number of data points is doubled for eye lenses and retinae.

The CNRs of eye lenses, retinae, and livers are independent of the ring current measured at the start of the helical CT scans (figure 5.3). This indicates a similar image quality for all resulting tomograms.

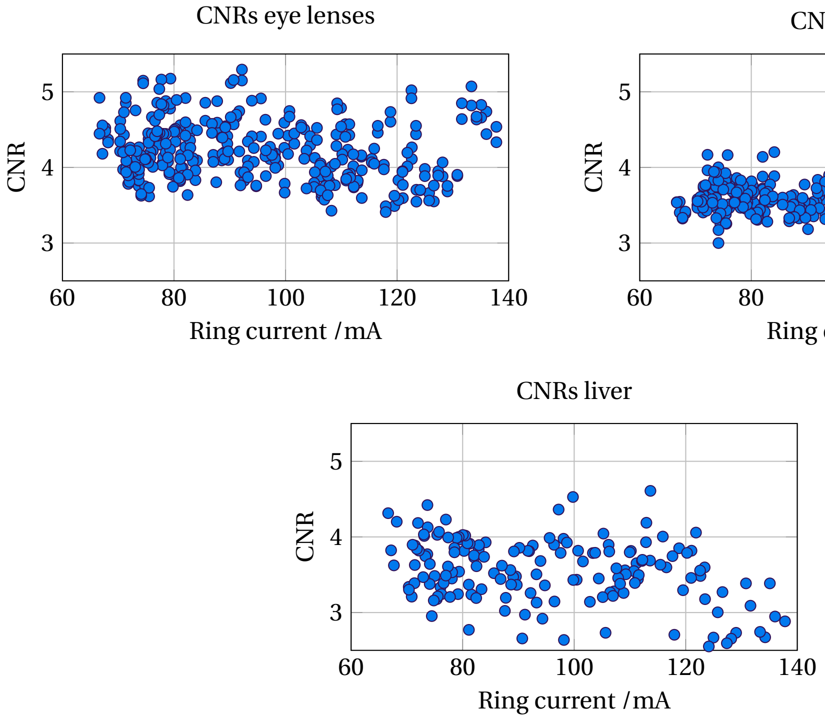

Figure 5.3.: CNRs of eye lenses, retinae, and livers plotted over ring current measured at the start of the corresponding helical CT scan. There was no discernible relationship between CNRs and ring current.

The CNRs plotted against the inbred lines (figure 5.4) indicated sufficient contrast, and thus staining, of the examined regions for all inbred lines. The CNRs of the eye lenses clearly differed between some of the inbred line for example 75-1 and 80-1. The CNRs of retinae and livers showed no significant difference.

Resolution

The aim of the imaging setup is to resolve all relevant structures in 10 weeks old medaka. The smallest structure of interest are the gill filaments with 10 µm [8]. The theoretical resolution of the imaging setup is 8.8 µm and identical for each measurement. Changes in resolution might occur due to a higher noise of the projections which correlates with the intensity of the x-ray beam and thus with the ring current. As electrons are injected but once in the morning at KIT Light Source, the ring current decreases during the day. Therefore, the SNR is lower for measurements late in the night and the higher noise might lower the resolution in the tomogram.

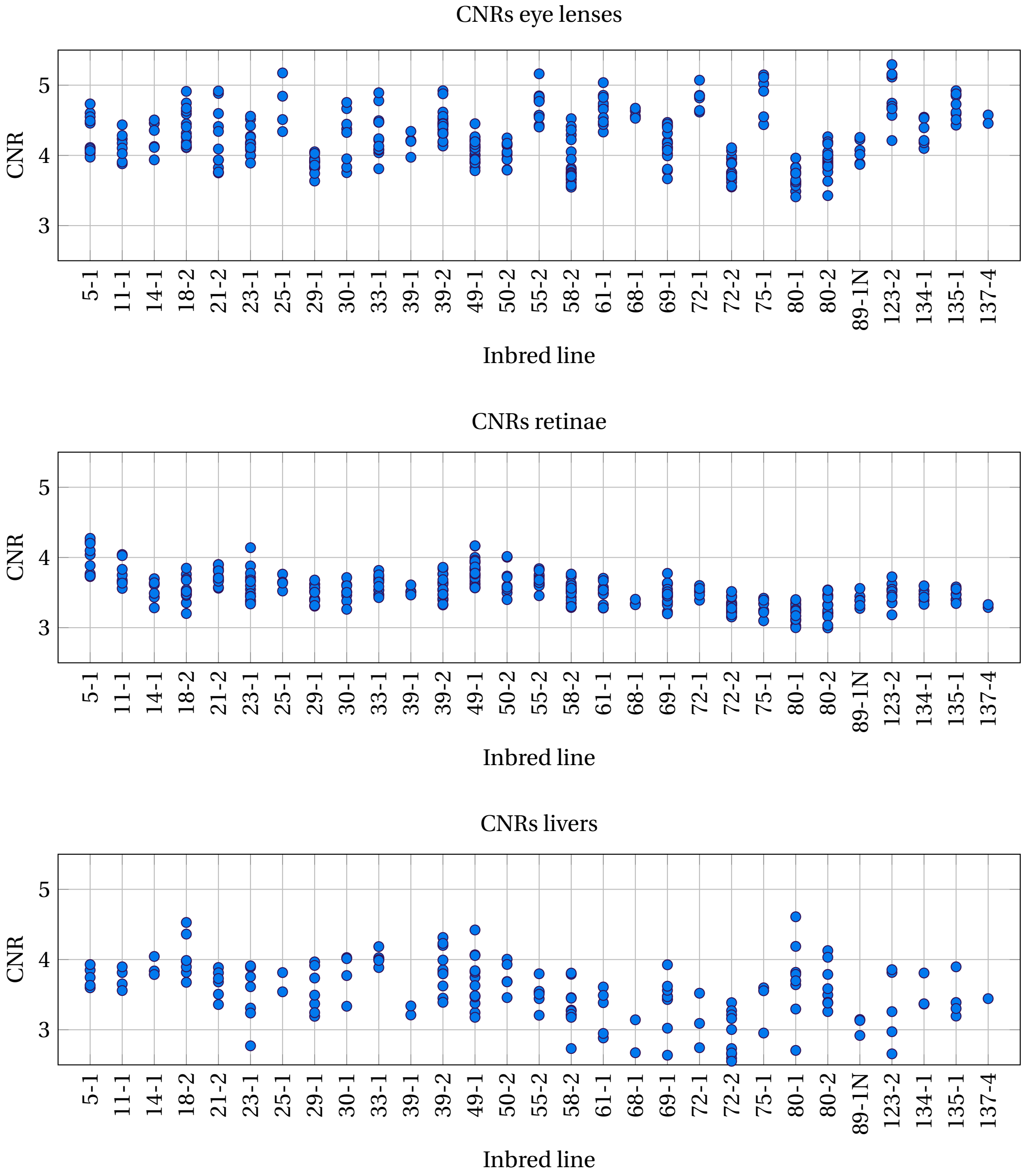

Figure 5.4.: Boxplots of the CNRs calculated for eye lenses, retinae, and livers plotted for the measured medaka inbred lines. The number of individuals scanned for each inbred line differs. In addition, the underlying values are twice for eye lenses and retinae, as each medaka has two eyes. The CNRs seemed to differ between the inbred lines.

A 3D spot check of 30 unaligned tomograms measured with different ring currents revealed that the gills were resolved in each medaka. The shape of the gills, as well as the shape and size of the head, differs between inbred lines (figure 5.5, A1 and B1).

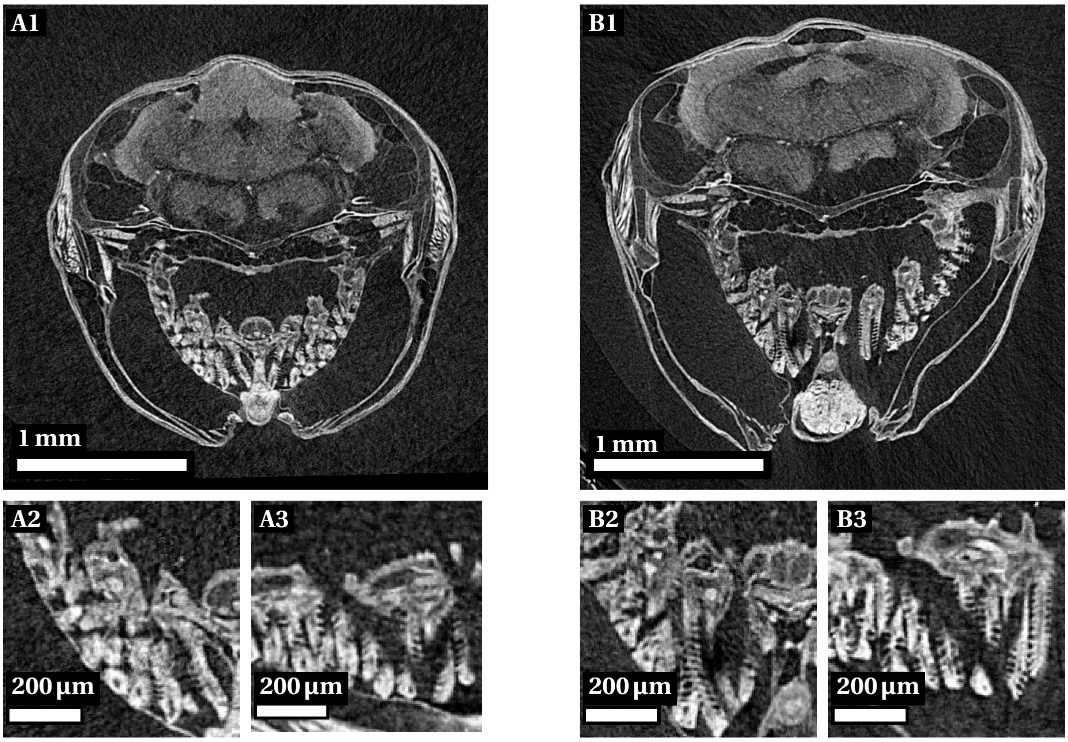

Figure 5.5.: Axial slices of (1) the head and (2) detailed axial and (3) sagittal views of the gills of two medaka from the inbred lines (A) 29-1 and (B) 33-1. The gills were resolved. Their shape, as well as head shape and size, differs between the inbred lines. The grey values display the absorption coefficients from 0 cm^{-1} to 6.82 cm^{-1} (black to white).

Conclusion

The analysis of CNRs in 161 medaka yielded consistent image quality independently of the imaging setup and the differing ring current. As the CNRs are independent of the physical measurement setup (figure 5.3), the tendency about differing CNRs between different inbred lines (figure 5.4) results from variances of the inbred lines, for example in size. Visual analysis of 30 medaka demonstrated sufficient resolution to resolve the gill structures. Thus, the tomograms resulting from the imaging pipeline are suited for comparative studies on morphometry. A final evaluation of the contrast and the achieved resolution of all 884 medaka measured up to now is planned as soon as automated segmentation and analysis of relevant structures is possible to minimize the time effort needed.

5.2.3. Segmentation of medaka

For biological studies on phenotypes, segmentation and further morphometric analysis of the tomograms are key. This section shows the available level of detail in a semi-automated segmentation (section 2.6.3) of an 11 weeks old medaka of the inbred line 94-1. To reduce data size and workload, the data set was binned by a factor of two prior to segmentation. The time effort to complete the manual labelling and the interpolation was about 150 h. Histological slices of adult medaka [60] were used to identify the organs and structures.

Segmentation of all inner organs and of parts of the skeleton, the muscles, the nervous system, and the circulatory system was possible. The simultaneous accessibility of axial, sagittal, and coronal slices of the virtual 3D volume allowed precise label assignment. Table 5.2 gives an overview of all labelled organs and tissues. Some structures could be labelled, but the interpolation by biomedisa failed. This was the case for thin structures with a width of just a few pixels or small structures with contrast differences. Such contrast differences occur for example in blood vessels, as the blood is not evenly distributed. Segmentation and interpolation of the skull and the rips was difficult due to enclosing muscles with similar contrast. In addition, the differentiation between smooth muscle tissue, blood vessels, and nerves proved difficult without deep anatomical knowledge.

Table 5.2.: List of organs and tissues of an 11 weeks old medaka manually labelled and interpolated using biomedisa [58]. The semi-automated segmentation failed at thin structures, at which the interpolation failed.

	segmented	labelled, interpolation failed
Skeleton	vertebral column	skull, rips, fin rays
Muscle	tongue, back muscle, tail muscle, fin muscles	
Nervous system	optic nerves, brain including substructures, spinal cord	olfactory nerves
Sensory system	eyes including substructures, inner ears	
Circulatory system	heart, bulbus arteriosus with aorta and pulmonary branches	
Digestive tract	liver, gallbladder, spleen, pancreas, intestine	
Respiratory system	gills	
Urinary system	head kidneys, urinary bladder, ureter	
Others	air bladder, testis	peritoneum

The volume render (figure 5.6a) gives a 3D impression of selected organs. The coronal slices (figure 5.6b) give an overview of segmented regions from top to bottom of the medaka. In almost all organs, smaller structures, such as different brain regions, atrium and ventricle in the heart, and retinal layers, were distinguishable. The brain regions (figure 5.7) were defined in as much detail as possible for a non-expert. It includes the segmentation of the optic nerves. The border between brain and spinal cord is artificial and adapted from a medaka brain atlas [76].

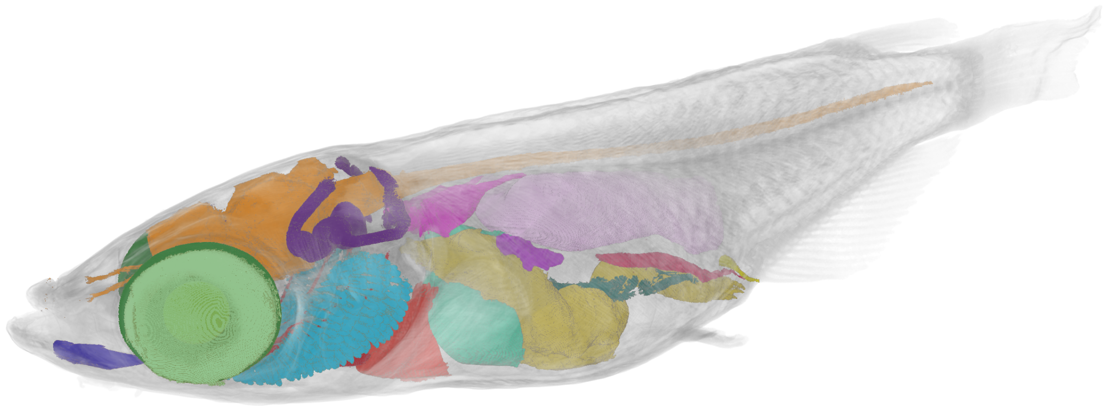

(a) Volume render.

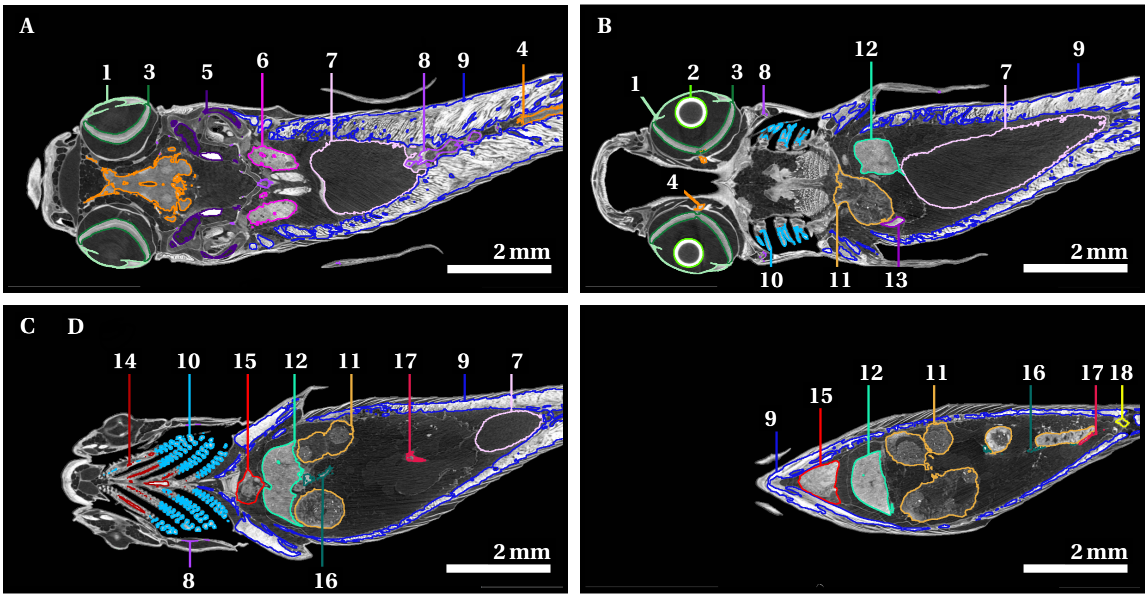

1. Cornea and iris
2. Lens
3. Retina
4. Nervous system
5. Inner ear
6. Head kidneys
7. Air bladder
8. Vertebral column
9. Muscle
10. Gills
11. Intestine
12. Liver
13. Spleen
14. Pulmonary branch
15. Heart
16. Pancreas
17. Testis
18. Urinary tract

(b) Coronal slices with labels.

Figure 5.6.: Results of a semi-automated segmentation of an 11 weeks old medaka of the inbred line 94-1. (a) The volume render displays the 3D shape and distribution of the segmented organs and tissues. (b) The coronal slices display the labels resulting from the semi-automated segmentation from dorsal to ventral (A to D).

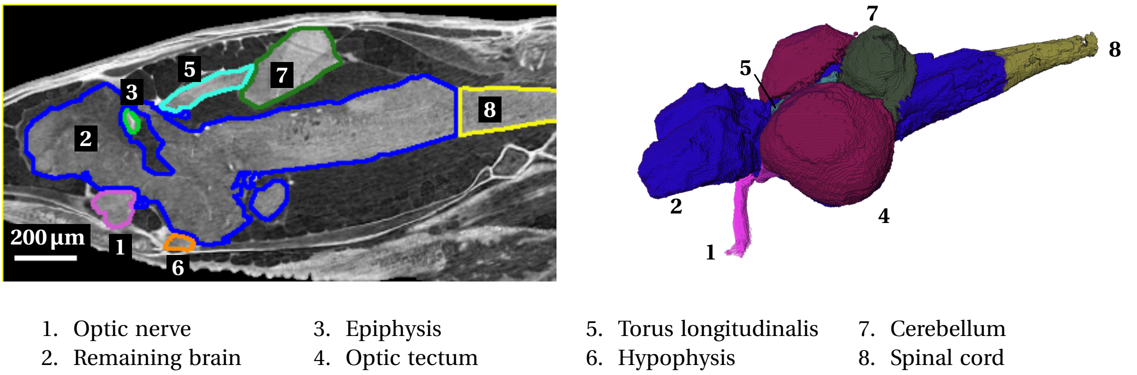

Figure 5.7.: Detailed semi-automated segmentation of the brain of an 11 months old medaka of the inbred line 94-1. (left) Sagittal mid-brain slice with the marked labels. (right) Volume render of the segmented brain regions and the optic nerves. The border between brain and spinal cord is artificial.

To conclude, the segmentation of all relevant organs was possible. As semi-automated segmentation takes a long time, automated segmentation of the medaka is desirable. Another advantage of automated segmentation is that a neural network might not only train for contrast but also for structure or shape. This would facilitate for example the differentiation between the structured muscles and the smooth bone in medaka head. Working on the original sized data would allow for the segmentation of thin structures at which interpolation failed.

5.3. Conclusion

The optimized sample preparation and data acquisition ensure a consistent image quality and resolution. Therefore, the developed imaging pipeline is well suited for large-scale, comparative studies on 10 weeks old, adult medaka. Semi-automated segmentation of a medaka demonstrated that all relevant organs and structures can be segmented. As semi-automated segmentation is time-consuming, the training of neural networks for automated segmentation has started. Currently, the eye lenses, the retinae, and the liver can be automatically segmented. A remaining challenge is the large data size not only for long-term data storage but also for the segmentation.

Chapter 6

Summary and conclusion

This thesis established a high-throughput pipeline for morphological 3D imaging of small vertebrate model organisms. 3D representations of vertebrate model organisms enable researchers to study development and disease etiology based on morphometric data [1–5]. High-throughput imaging will allow the measurement of sufficient sample numbers for statistical analysis in a reasonable amount of time, thus overcoming a major limitation of current experimental series. The morphological imaging pipeline comprises the three main parts: sample preparation, data acquisition, and image reconstruction. Due to dependencies between the three parts, they must be mutually optimized. The sample preparation influences the preservation of the sample anatomy as well as the image contrast. The choice of the physically measured image contrast puts demands on sample preparation as well as the algorithms used for 2D and 3D image reconstruction. The specific configurations of the imaging setup used for data acquisition as well as the image reconstruction algorithms define the final imaging contrast and the achievable resolution. Various external constraints as sample size or computational power limit the detailed implementation. Requirements on the performance of the pipeline as well as the resulting 3D representation also have to be considered. The following requirements were identified as particularly important for a high-throughput imaging pipeline with focus on 3D representations for morphometric analysis of small vertebrate model organisms:

- availability of the imaging setup for measurement campaigns with large sample series,
- a sample preparation preserving the sample in a state as close to living as possible,
- a minimum time effort, especially regarding data acquisition,
- preservation of the sample anatomy also during storage,
- provision of the 3D representation of the full-body of the organism in sufficient resolution,
- the depiction of all relevant organs and tissues with sufficient contrast for segmentation,
- reproducible image quality of the 3D representations for comparative studies.

The development of an imaging pipeline thus requires to carefully weigh external constraints and requirements against each other. This thesis demonstrates this procedure on the example of the model organism medaka (*Oryzias latipes*), also known as Japanese rice fish.

As one aim is the 3D representation of the full medaka body on the scale of single organs down to tissues at a resolution of 10 µm, x-ray computed tomography was chosen as imaging technique. It provides a 3D representation in sufficient resolution and in a reasonable amount of time. A challenge in x-ray imaging of biological samples is the low natural absorption of biological soft tissue and thus low absorption contrast. X-ray phase contrast is well suited for imaging of low absorbing materials but cannot be directly measured. To find the best suited physical contrast for medaka, also under consideration of the requirements defined above, absorption imaging, inline phase-contrast imaging, and grating interferometry (GI) were further analysed regarding contrast generation, resolution, and acquisition time.

Absorption imaging bases on direct intensity attenuation of x-rays passing through a sample. Therefore, an x-ray detector is sufficient to directly measure the resulting absorption image. Complete non-specific staining of the whole adult medaka body was a particular challenge to sufficiently increase the low natural absorption of biological soft tissue. In this thesis, absorption imaging with phosphotungstic acid (PTA) staining was demonstrated at a synchrotron and a laboratory source. Experiments with a previously developed staining protocol yielded an insufficient staining of most medaka. Detailed studies on PTA staining led to a reliable full-body staining of adult medaka of different sizes. The staining allows tissue differentiation and segmentation down to the level of different brain regions. The developed PTA staining protocol thereby overcomes previously reported limitations on sample size. The acquisition time for two months old medaka at the synchrotron was reduced by a factor of 10 in comparison to a previous high-resolution setup. The achieved resolution of the synchrotron setup was sufficient even to resolve the gills. An issue in pink beam imaging at the synchrotron was bubble formation in the embedding material which could be solved by a suitable replacement. The resolution of the CT scans carried out at the laboratory was not sufficient to resolve the gills. A higher resolution would be possible at the cost of an acquisition time more than 10 times of that achieved at the synchrotron.

Phase contrast imaging is well suited for low absorbing materials as the phase changes induced by the sample are large enough for sufficient contrast. As no staining is required, the risk for sample alteration is lower and even application to living specimens is possible [10, 11]. However, the phase and thus phase changes cannot be directly measured. As a requirement for high-throughput imaging is a short acquisition time, single distance phase imaging with Paganin phase retrieval was tested on medaka. This method retrieves the phase from the Fresnel diffraction pattern in the propagated x-ray wave field behind the sample. Due to the needed propagation, this phase imaging method is limited to sources offering a sufficiently coherent x-ray beam. The contrast of soft tissues in unstained medaka was significantly increased in comparison to the absorption image. Tissue differentiation was difficult, as all tissues yielded a similar contrast.

GI provides absorption, differential phase, and visibility contrast of a sample in a single experiment. Visibility contrast thereby comprises scattering and unresolved differential phase contrast. GI bases on the self-imaging effect, also known as the Talbot effect, of periodic structures. The self-image of a grating is projected onto a second grating, called analyser grating. Therefore, sufficient coherence of the x-ray beam is required. Measurements at x-ray sources providing a low coherent x-ray beam are possible with the introduction of a third grating, called source grating, near the source. The three contrasts are retrieved from several radiograms measured in a phase stepping scan, in which the phase or the analyser grating is shifted relative to the other grating(s). With an available grating interferometer, two months old, dried medaka were measured. Absorption, differential phase, and visibility contrast were retrieved using a different number of radiograms. An acceptable image quality was achieved with five radiograms. Each retrieved contrast provided different information on the sample. This advantage comes at the cost of an acquisition time at least 5 times longer in comparison to conventional absorption imaging. In addition, the available grating interferometer does not match the resolution requirements for the measurement of medaka.

Finally, absorption imaging based on the developed staining protocol was chosen for the *high-throughput* 3D imaging pipeline due to both, the excellent tissue differentiation in sufficient resolution and its relatively short acquisition time. Additionally, absorption imaging could be further improved regarding image quality and time effort with the use of helical CT. Helical CT reduces ring artefacts due to a movement along the axis of rotation during image data acquisition. This movement allows to measure the complete length of a medaka in a single acquisition. In addition, the post-processing time is significantly reduced in comparison to the prior used step CT configuration with several acquired tomograms per medaka.

With the improvements on sample preparation and data acquisition achieved in this thesis, the absorption imaging setup with synchrotron pink beam matches the requirements for a high-throughput imaging setup. The final pipeline was optimized for *adult* (10 weeks old) medaka regarding sample preparation and scanning field of view of the imaging setup.

The pipeline starts with the sample preparation. The medaka are fixed and stained according to the optimized sample preparation protocol to preserve the sample and to ensure sufficient absorption contrast. Samples can be stored for at least half a year without degeneration, which allows to prepare a large number of samples in advance. The medaka are embedded into Eppendorf tubes to standardize the sample size and enable the use of a sample changer robot.

The imaging setup used is located at the UFO station of KIT Light Source to which systematic access is granted for large-scale comparative morphological studies. With the high-throughput imaging setup, more than 100 medaka can be measured within a single day. The current limitation for further reduction of the acquisition time is the state-of-the-art camera data read-out. The automatized sample robot available at the UFO station allows a batch process. Human interaction is only required every 9 h to provide a new sample tray with 49 samples. Thus, it is possible to run large sample series in a reasonable amount of time with low human resources.

In post-processing, the tomographic reconstruction of helical CT data is automated using a new development of the UFO platform [55] based on concert [48]. A remaining challenge is the storage of the acquired data which results in more than 16 TB per day of measurement.

The capability of the developed pipeline to run large sample series has been demonstrated by performing measurement campaigns resulting in morphometric 3D representations of more than 800 medaka. The analysis of the tomograms demonstrated reliable and repeatable resolution as well as image quality, for example regarding contrast and noise. Semi-automated segmentation of all relevant organs of a medaka was possible including the segmentation of different brain regions. Initial results of automated segmentation showed the potential for time-efficient segmentation of large sample numbers.

6.1. Future perspectives

The high-throughput 3D imaging pipeline developed in this thesis was specifically optimized for imaging of 10 weeks old, adult medaka (length about 20 mm). It can be further optimized regarding acquisition time by mapping the vertical travel of the helical CT scan to the actual sample size and not to the length of the container. The challenge is the automated detection of the medaka tail fin due to its low contrast. Additionally, its position inside the container varies for each medaka making it hard to detect. Image recognition by a neural network might solve this issue.

The established pipeline itself can be readily applied to larger, older medaka with an adaption of the staining protocol according to the results of the staining optimization and an increase of the scanning field of view. With an adaption of the vertical travel, the established helical CT setup is usable up to sample sizes that fit into 2 mm Eppendorf tubes. In general, the established high-throughput imaging pipeline is directly applicable to vertebrate of similar size as medaka. The experience in creating, implementing, and optimization of the complete workflow for large scale comparative studies can be used to establish pipelines for any small organism.

As absorption imaging is also applicable at laboratory sources, it allows to run large scale studies even on samples that do not fit into the synchrotron field of view. The key to handling large sample numbers is to run the data acquisition at several laboratories in parallel. Comparative results must be ensured by detailed measurement protocols. Further tests must show the limitation on sample size of the staining procedure developed in the framework of this thesis. Up to now, it has been successfully applied to various vertebrate up to the size of an adult western clawed frog (*Xenopus tropicalis*) with a body length of about 50 mm.

Automated segmentation of the acquired data will be a useful extension of the imaging pipeline. It greatly reduces the time effort per sample regarding segmentation. In addition, with automated morphometric analysis, automated segmentation is key for the analysis of large-scale studies in a reasonable amount of time. Up to now, eye lenses, retinae, liver, and the outer shape of medaka can be automatically segmented and analysed. Systematically training data will be created for all relevant organs and tissues of medaka to allow the extensions of the neural networks developed by Yaroslav Zharov (Institute for Photon Science and Synchrotron Radiation, Karlsruhe Institute of Technology). The acquired data of medaka is used for the correlation of morphometric data to the genome of medaka inbred lines in cooperation with the Centre for Organismal Studies Heidelberg (University Heidelberg) and the European Bioinformatics Institute (European Molecular Biology Laboratory). The results will allow future studies on phenotype-genotype correlation.

Bibliography

[1] P. M. Larson, 'Chondrocranial development in larval Rana sylvatica (Anura: Ranidae): morphometric analysis of cranial allometry and ontogenetic shape change', Journal of morphology **252**, 131–144 (2002).

[2] C. Parng, N. M. Roy, C. Ton, Y. Lin and P. McGrath, 'Neurotoxicity assessment using zebrafish', Journal of pharmacological and toxicological methods **55**, 103–112 (2007).

[3] J.-H. He, S.-Y. Guo, F. Zhu, J.-J. Zhu, Y.-X. Chen, C.-J. Huang, J.-M. Gao, Q.-X. Dong, Y.-X. Xuan and C.-Q. Li, 'A zebrafish phenotypic assay for assessing drug-induced hepatotoxicity', Journal of pharmacological and toxicological methods **67**, 25–32 (2013).

[4] J. F. Charles, M. Sury, K. Tsang, K. Urso, K. Henke, Y. Huang, R. Russell, J. Duryea and M. P. Harris, 'Utility of quantitative micro-computed tomographic analysis in zebrafish to define gene function during skeletogenesis', Bone **101**, 162–171 (2017).

[5] S. Jarque, M. Rubio-Brotons, J. Ibarra, V. Ordoñez, S. Dyballa, R. Miñana and J. Terriente, 'Morphometric analysis of developing zebrafish embryos allows predicting teratogenicity modes of action in higher vertebrates', Reproductive toxicology (Elmsford, N.Y.) **96**, 337–348 (2020).

[6] L. Quintana and J. Sharpe, 'Optical Projection Tomography of Vertebrate Embryo Development', in *Imaging in developmental biology*, edited by J. Sharpe, R. O. Wong and R. Yuste, Imaging series (CSH Laboratory Press, Cold Spring Harbor, NY, 2011), pp. 739–752.

[7] S. Kirchmaier, K. Naruse, J. Wittbrodt and F. Loosli, 'The genomic and genetic toolbox of the teleost medaka (Oryzias latipes)', Genetics **199**, 905–918 (2015).

[8] I. Leguen, 'Gills of the medaka (Oryzias latipes): A scanning electron microscopy study', Journal of morphology **279**, 97–108 (2018).

[9] B. D. Metscher, 'MicroCT for comparative morphology: simple staining methods allow high-contrast 3D imaging of diverse non-mineralized animal tissues', BMC physiology **9**, 11 (2009).

[10] J. Moosmann, A. Ershov, V. Altapova, T. Baumbach, M. S. Prasad, C. LaBonne, X. Xiao, J. Kashef and R. Hofmann, 'X-ray phase-contrast in vivo microtomography probes new aspects of Xenopus gastrulation', Nature **497**, 374–377 (2013).

[11] J. Moosmann, A. Ershov, V. Weinhardt, T. Baumbach, M. S. Prasad, C. LaBonne, X. Xiao, J. Kashef and R. Hofmann, 'Time-lapse X-ray phase-contrast microtomography for in vivo imaging and analysis of morphogenesis', Nature protocols **9**, 294–304 (2014).

[12] T. Koenig, M. Zuber, B. Trimborn, T. Farago, P. Meyer, D. Kunka, F. Albrecht, S. Kreuer, T. Volk, M. Fiederle and T. Baumbach, 'On the origin and nature of the grating interferometric dark-field contrast obtained with low-brilliance x-ray sources', Physics in medicine and biology **61**, 3427–3442 (2016).

[13] F. Pfeiffer, T. Weitkamp, O. Bunk and C. David, 'Phase retrieval and differential phase-contrast imaging with low-brilliance X-ray sources', Nature physics **2**, 258 (2006).

[14] F. Pfeiffer, M. Bech, O. Bunk, P. Kraft, E. F. Eikenberry, C. Brönnimann, C. Grünzweig and C. David, ‘Hard-X-ray dark-field imaging using a grating interferometer’, Nature materials **7**, 134 (2008).

[15] R. Gradl, K. S. Morgan, M. Dierolf, C. Jud, L. Hehn, B. Gunther, W. Moller, D. Kutschke, L. Yang, T. Stoeger, D. Pfeiffer, B. Gleich, K. Achterhold, O. Schmid and F. Pfeiffer, ‘Dynamic In Vivo Chest X-ray Dark-Field Imaging in Mice’, IEEE transactions on medical imaging **38**, 649–656 (2019).

[16] K. Takashima, M. Hoshino, K. Uesugi, N. Yagi, S. Matsuda, A. Nakahira, N. Osumi, M. Kohzuki and H. Onodera, ‘X-ray phase-contrast computed tomography visualizes the microstructure and degradation profile of implanted biodegradable scaffolds after spinal cord injury’, Journal of synchrotron radiation **22**, 136–142 (2015).

[17] M. Willner, J. Herzen, S. Grandl, S. Auweter, D. Mayr, A. Hipp, M. Chabior, A. Sarapata, K. Achterhold, I. Zanette, T. Weitkamp, A. Sztrókay, K. Hellerhoff, M. Reiser and F. Pfeiffer, ‘Quantitative breast tissue characterization using grating-based x-ray phase-contrast imaging’, Physics in medicine and biology **59**, 1557–1571 (2014).

[18] D. M. Paganin, *Coherent X-ray optics*, Vol. 6, Oxford series on synchrotron radiation (Oxford University Press, Oxford, 2006).

[19] J. Als-Nielsen and Des McMorrow, *Elements of modern X-ray physics*, Second edition (Wiley, Chichester, 2011).

[20] *XCOM-Photon Cross Sections Database, NIST Standard Reference Database 8*, https://physics.nist.gov/PhysRefData/Xcom/html/xcom1.html.

[21] W. Demtröder, *Experimentalphysik 4* (Springer Berlin Heidelberg, Berlin, Heidelberg, 2017).

[22] *Index of Refraction*, https://henke.lbl.gov/optical_constants/getdb2.html.

[23] D. Paganin, S. C. Mayo, T. E. Gureyev, P. R. Miller and S. W. Wilkins, ‘Simultaneous phase and amplitude extraction from a single defocused image of a homogeneous object’, Journal of microscopy **206**, 33–40 (2002).

[24] R. Lohr, C. C. Scott, A. Pil-Ali and K. S. Karim, ‘A comparison of phase retrieval methods for propagation-based phase contrast X-ray imaging with polychromatic sources’, in Medical Imaging 2020: Physics of Medical Imaging, edited by G.-H. Chen and H. Bosmans, Progress in biomedical optics and imaging (2020), p. 182.

[25] T. Faragó, P. Mikulík, A. Ershov, M. Vogelgesang, D. Hänschke and T. Baumbach, ‘syris: a flexible and efficient framework for X-ray imaging experiments simulation’, Journal of synchrotron radiation **24**, 1283–1295 (2017).

[26] M. R. Teague, ‘Deterministic phase retrieval: a Green’s function solution’, Journal of the Optical Society of America **73**, 1434 (1983).

[27] T. Weitkamp, D. Haas, D. Wegrzynek and A. Rack, ‘ANKAphase: software for single-distance phase retrieval from inline X-ray phase-contrast radiographs’, Journal of synchrotron radiation **18**, 617–629 (2011).

[28] Y. I. Nesterets, S. W. Wilkins, T. E. Gureyev, A. Pogany and A. W. Stevenson, ‘On the optimization of experimental parameters for x-ray in-line phase-contrast imaging’, The Review of scientific instruments **76**, 093706 (2005).

[29] H. F. Talbot, 'LXXVI. Facts relating to optical science. No. IV', The London, Edinburgh, and Dublin Philosophical Magazine and Journal of Science **9**, 401–407 (1836).

[30] Gerhard Merziger, Günter Mühlbach, Detlef Wille and Thomas Wirth, *Formeln und Hilfen zur höheren Mathematik*, 4th ed. (Binomi, Springer, 2001).

[31] T. J. Suleski, 'Generation of Lohmann images from binary-phase Talbot array illuminators', Applied optics **36**, 4686–4691 (1997).

[32] A. W. Lohmann, H. Knuppertz and J. Jahns, 'Fractional Montgomery effect: a self-imaging phenomenon', Journal of the Optical Society of America. A, Optics, image science, and vision **22**, 1500–1508 (2005).

[33] M. Bech, O. Bunk, T. Donath, R. Feidenhans, C. David and F. Pfeiffer, 'Quantitative x-ray dark-field computed tomography', Physics in Medicine & Biology **55**, 5529 (2010).

[34] P. Zhu, K. Zhang, Z. Wang, Y. Liu, X. Liu, Z. Wu, S. A. McDonald, F. Marone and M. Stampanoni, 'Low-dose, simple, and fast grating-based X-ray phase-contrast imaging', Proceedings of the National Academy of Sciences of the United States of America **107**, 13576–13581 (2010).

[35] P. C. Diemoz, P. Coan, I. Zanette, A. Bravin, S. Lang, C. Glaser and T. Weitkamp, 'A simplified approach for computed tomography with an X-ray grating interferometer', Optics express **19**, 1691–1698 (2011).

[36] A. Momose, W. Yashiro, H. Maikusa and Y. Takeda, 'High-speed X-ray phase imaging and X-ray phase tomography with Talbot interferometer and white synchrotron radiation', Optics express **17**, 12540–12545 (2009).

[37] Y. Ge, K. Li, J. Garrett and G.-H. Chen, 'Grating based x-ray differential phase contrast imaging without mechanical phase stepping', Optics express **22**, 14246–14252 (2014).

[38] H. Xie, W. Cai, L. Yang, H. Mao and X. Tang, 'Reducing radiation dose in grating based x-ray phase contrast CT with twin-peaks in its phase stepping curves', Medical physics **43**, 5942 (2016).

[39] Y. Yang, H. Xie, W. Cai, H. Mao and X. Tang, 'Grating-based x-ray differential phase contrast imaging with twin peaks in phase-stepping curves-phase retrieval and dewrapping', Medical physics **43**, 2855–2869 (2016).

[40] W. Haas, M. Bech, P. Bartl, F. Bayer, A. Ritter, T. Weber, G. Pelzer, M. Willner, K. Achterhold, J. Durst, T. Michel, M. Prümmer, F. Pfeiffer, G. Anton and J. Hornegger, 'Phase-unwrapping of differential phase-contrast data using attenuation information', in Medical Imaging 2011: Image Processing, edited by B. M. Dawant and D. R. Haynor, SPIE Proceedings (2011), 79624R.

[41] G. Rodgers, G. Schulz, H. Deyhle, S. Marathe, C. Bikis, T. Weitkamp and B. Müller, 'A quantitative correction for phase wrapping artifacts in hard X-ray grating interferometry', Applied Physics Letters **113**, 093702 (2018).

[42] F. M. Epple, G. Potdevin, P. Thibault, S. Ehn, J. Herzen, A. Hipp, F. Beckmann and F. Pfeiffer, 'Unwrapping differential x-ray phase-contrast images through phase estimation from multiple energy data', Optics express **21**, 29101–29108 (2013).

[43] J. Besag, 'On the Statistical Analysis of Dirty Pictures', Journal of the Royal Statistical Society: Series B (Methodological) **48**, 259–279 (1986).

[44] T. Weitkamp, A. Diaz, C. David, F. Pfeiffer, M. Stampanoni, P. Cloetens and E. Ziegler, ‘X-ray phase imaging with a grating interferometer’, Optics express **13**, 6296–6304 (2005).

[45] K. Creath and J. C. Wyant, ‘Moiré and fringe projection techniques’, in *Optical shop testing*, edited by D. Malacara, Wiley series in pure and applied optics (Wiley, New York, 1992), pp. 653–685.

[46] M. Engelhardt, C. Kottler, O. Bunk, C. David, C. Schroer, J. Baumann, M. Schuster and F. Pfeiffer, ‘The fractional Talbot effect in differential x-ray phase-contrast imaging for extended and polychromatic x-ray sources’, Journal of microscopy **232**, 145–157 (2008).

[47] D. M. Pelt and D. Y. Parkinson, ‘Ring artifact reduction in synchrotron x-ray tomography through helical acquisition’, Measurement Science and Technology **29**, 034002 (2018).

[48] M. Vogelgesang, T. Farago, T. F. Morgeneyer, L. Helfen, T. Dos Santos Rolo, A. Myagotin and T. Baumbach, ‘Real-time image-content-based beamline control for smart 4D X-ray imaging’, Journal of synchrotron radiation **23**, 1254–1263 (2016).

[49] L. A. Feldkamp, L. C. Davis and J. W. Kress, ‘Practical cone-beam algorithm’, Journal of the Optical Society of America. A, Optics, image science, and vision **1**, 612 (1984).

[50] M. Kachelriess, M. Knaup and W. A. Kalender, ‘Extended parallel backprojection for standard three-dimensional and phase-correlated four-dimensional axial and spiral cone-beam CT with arbitrary pitch, arbitrary cone-angle, and 100% dose usage’, Medical physics **31**, 1623–1641 (2004).

[51] X. Tang, J. Hsieh, A. Hagiwara, R. A. Nilsen, J.-B. Thibault and E. Drapkin, ‘A three-dimensional weighted cone beam filtered backprojection (CB-FBP) algorithm for image reconstruction in volumetric CT under a circular source trajectory’, Physics in Medicine & Biology **50**, 3889–3905 (2005).

[52] P. S. Tofts and J. C. Gore, ‘Some sources of artefact in computed tomography’, Physics in Medicine & Biology **25**, 117–127 (1980).

[53] R. Schulze, U. Heil, D. Gross, D. D. Bruellmann, E. Dranischnikow, U. Schwanecke and E. Schoemer, ‘Artefacts in CBCT: a review’, Dento maxillo facial radiology **40**, 265–273 (2011).

[54] R. A. Brooks and G. Di Chiro, ‘Beam hardening in x-ray reconstructive tomography’, Physics in Medicine & Biology **21**, 390–398 (1976).

[55] M. Vogelgesang, S. Chilingaryan, T. d. Rolo and A. Kopmann, ‘UFO: A Scalable GPU-based Image Processing Framework for On-line Monitoring’, in IEEE 14th International Conference on High Performance Computing and Communications & 2012 IEEE 9th International Conference on Embedded Software and Systems (HPCC-ICESS), 2012, edited by G. Min (2012), pp. 824–829.

[56] J. Schindelin, I. Arganda-Carreras, E. Frise, V. Kaynig, M. Longair, T. Pietzsch, S. Preibisch, C. Rueden, S. Saalfeld, B. Schmid, J.-Y. Tinevez, D. J. White, V. Hartenstein, K. Eliceiri, P. Tomancak and A. Cardona, ‘Fiji: an open-source platform for biological-image analysis’, Nature methods **9**, 676–682 (2012).

[57] I. Wolf, M. Vetter, I. Wegner, T. Böttger, M. Nolden, M. Schöbinger, M. Hastenteufel, T. Kunert and H.-P. Meinzer, ‘The medical imaging interaction toolkit’, Medical image analysis **9**, 594–604 (2005).

[58] P. D. Lösel, T. van de Kamp, A. Jayme, A. Ershov, T. Faragó, O. Pichler, N. Tan Jerome, N. Aadepu, S. Bremer, S. A. Chilingaryan, M. Heethoff, A. Kopmann, J. Odar, S. Schmelzle, M. Zuber, J. Wittbrodt, T. Baumbach and V. Heuveline, 'Introducing Biomedisa as an open-source online platform for biomedical image segmentation', Nature Communications **11**, 1–14 (2020).

[59] A. Limaye, 'Drishti: a volume exploration and presentation tool', in Developments in X-Ray Tomography VIII, edited by S. R. Stock, SPIE Proceedings (2012), p. 85060X.

[60] medaka, *Medaka Book DVD*, https://medaka-book.org.

[61] V. Weinhardt, R. Shkarin, T. Wernet, J. Wittbrodt, T. Baumbach and F. Loosli, 'Quantitative morphometric analysis of adult teleost fish by X-ray computed tomography', Scientific reports **8**, 16531 (2018).

[62] Eppendorf, *Technical drawing Eppendorf Safe-Lock Tube 2.0ml*, https://www.eppendorf.com/product-media/doc/en/140034_Technical-Data/Eppendorf_Consumables_Technical-data_Safe-Lock-Tube-20-mL_Safe-Lock-20-mL-technical-drawing.pdf, 2021.

[63] T. J. Schröter, F. Koch, P. Meyer, M. Baumann, D. Münch, D. Kunka, S. Engelhardt, M. Zuber, T. Baumbach and J. Mohr, 'Large area gratings by x-ray LIGA dynamic exposure for x-ray phase-contrast imaging', Journal of Micro/Nanolithography, MEMS, and MOEMS **16**, 013501 (2017).

[64] T. J. Schröter, F. J. Koch, D. Kunka, P. Meyer, S. Tietze, S. Engelhardt, M. Zuber, T. Baumbach, K. Willer, L. Birnbacher, F. Prade, F. Pfeiffer, K.-M. Reichert, A. Hofmann and J. Mohr, 'Large-area full field x-ray differential phase-contrast imaging using 2D tiled gratings', Journal of Physics D: Applied Physics **50**, 225401 (2017).

[65] S. A. McDonald, F. Marone, C. Hintermüller, G. Mikuljan, C. David, F. Pfeiffer and M. Stampanoni, 'Advanced phase-contrast imaging using a grating interferometer', Journal of synchrotron radiation **16**, 562–572 (2009).

[66] M. A. Beltran, D. M. Paganin, K. Uesugi and M. J. Kitchen, '2D and 3D X-ray phase retrieval of multi-material objects using a single defocus distance', Optics express **18**, 6423–6436 (2010).

[67] E. Pauwels, D. van Loo, P. Cornillie, L. Brabant and L. van Hoorebeke, 'An exploratory study of contrast agents for soft tissue visualization by means of high resolution X-ray computed tomography imaging', Journal of microscopy **250**, 21–31 (2013).

[68] C. Dullin, R. Ufartes, E. Larsson, S. Martin, M. Lazzarini, G. Tromba, J. Missbach-Guentner, D. Pinkert-Leetsch, D. M. Katschinski and F. Alves, 'µCT of ex-vivo stained mouse hearts and embryos enables a precise match between 3D virtual histology, classical histology and immunochemistry', PloS one **12**, e0170597 (2017).

[69] K.-C. Chen, A. Arad, Z.-M. Song and D. Croaker, 'High-definition neural visualization of rodent brain using micro-CT scanning and non-local-means processing', BMC Medical Imaging **18**, 38 (2018).

[70] M. Kaucka, J. Petersen, M. Tesarova, B. Szarowska, M. E. Kastriti, M. Xie, A. Kicheva, K. Annusver, M. Kasper, O. Symmons, L. Pan, F. Spitz, J. Kaiser, M. Hovorakova, T. Zikmund, K. Sunadome, M. P. Matise, H. Wang, U. Marklund, H. Abdo, P. Ernfors, P. Maire, M. Wurmser, A. S. Chagin, K. Fried and I. Adameyko, 'Signals from the brain and olfactory epithelium control shaping of the mammalian nasal capsule cartilage', eLife **7**, 10.7554/eLife.34465 (2018).

[71] G. Quintarelli, R. Zito and J. A. Cifonelli, ‘On phosphotungstic acid staining. I’, The journal of histochemistry and cytochemistry: official journal of the Histochemistry Society **19**, 641–647 (1971).

[72] Y. Ding, D. J. Vanselow, M. A. Yakovlev, S. R. Katz, A. Y. Lin, D. P. Clark, P. Vargas, X. Xin, J. E. Copper, V. A. Canfield, K. C. Ang, Y. Wang, X. Xiao, F. de Carlo, D. B. van Rossum, P. La Riviere and K. C. Cheng, ‘Computational 3D histological phenotyping of whole zebrafish by X-ray histotomography’, eLife **8**, {10.7554/eLife.44898} (2019).

[73] M. Patzelt, J. Mrzilkova, J. Dudak, F. Krejci, J. Zemlicka, J. Karch, V. Musil, J. Rosina, V. Sykora, B. Horehledova and P. Zach, ‘Ethanol fixation method for heart and lung imaging in micro-CT’, Japanese journal of radiology **37**, 500–510 (2019).

[74] Z. Zhu, R. Tain and C. Rhodes, ‘A study of the decomposition behaviour of 12-tungstophosphate heteropolyacid in solution’, Canadian Journal of Chemistry **81**, 1044–1050 (2003).

[75] R. Balint, T. Lowe and T. Shearer, ‘Optimal Contrast Agent Staining of Ligaments and Tendons for X-Ray Computed Tomography’, PloS one **11**, e0153552 (2016).

[76] R. Anken and F. Bourrat, *Brain atlas of the Medakafish: Oryzias latipes* (Inst. National de la Recherche Agronomique, Paris, 1998).

Appendix A

Supplements

A.1. Medaka stock and husbandry

Medaka are raised and maintained by the Loosli group at the Institute of Biological and Chemical Systems (IBCS) at the Karlsruhe Institute of Technology (KIT). They are kept in a tank system with recirculating water at 26 °C. The day/ night cycle is 14 h light and 10 h dark. Keeping the fish at a low density (1 fish per litre) avoids stress related variations during their development.

Animal husbandry and experimental procedures were performed in accordance with EU directive 2010/63/EU guidelines as well as with German animal protection regulations (Tierschutzgesetz §11, Abs. 1, no. 1; Regierungspräsidium Karlsruhe, Germany; husbandry permits AZ35-9185.64/BH KIT). The facility is under the supervision of the Regierungspräsidium Karlsruhe, who approved the experimental procedures.

A.2. Abbreviations

Table A.1.: List of abbreviations.

Chemicals		
	GA	glutaraldehyde
	LMA	low melting agarose
	PBS	phosphate buffered saline
	PFA	paraformaldehyde
	PMMA	polymethylmethacrylate $(C_5O_2H_8)_n$
	PTA	phosphotungstic acid
Imaging and analysis		
	CNR	contrast-to-noise ratio
	CT	computed tomography
	FFT	Fast Fourier Transform
	FST	Fourier slice theorem
	FOV	detector field of view
	GI	grating interferometry
	MRM	magnetic resonance microscopy
	µCT	micro computed tomography
	MUI	microscopic ultrasound imaging
	MRF	Markov-Random-Field
Institutes and setups		
	CL-Lab	Computed laminography laboratory
	IBCS	Institute of Biological and Chemical Systems
	IPS	Institute for Photon Science and Synchrotron Radiation
	KIT	Karlsruhe Institute of Technology

A.3. Symbols

Table A.2.: List of symbols.

α	angular deviation
β	imaginary part of the refractive index n
δ	refractive index decrement, real part of the refractive index n
λ	wavelength
ε_ω	electrical permittivity
$\mu = 2k\beta$	linear attenuation coefficient
μ_0	magnetic permeability
$\bar{\mu}$	mean value
Φ	phase shift
ϕ	phase
ψ_ω	function of a monochromatic plane wave
ρ	electron density
σ	standard deviation
a	Fourier coefficients
D	sample thickness
I	intensity
k	wave number
$\mathbf{k}$	wave vector
L	coherence length
M	magnification
n	refractive index
p	grating period
P	propagated wave field
ps	pixel size
r_0	Thomson scattering length
T	transmission function
T_μ	transmission of a sample
V	visibility
z	propagation distance
z_T	Talbot distance
$\mathscr{F}$	Fourier transformation